EVALUATION OF SIMULATED TROPICAL CONVECTIVE UPDRAFT HYDROMETEOR PROPERTIES USING AIRCRAFT OBSERVATIONS

by

McKenna W. Stanford

A thesis submitted to the faculty of
The University of Utah
in partial fulfillment of the requirements for the degree of

Master of Science

Department of Atmospheric Sciences

The University of Utah

December 2016

The University of Utah Graduate School

STATEMENT OF THESIS APPROVAL

The thesis of **McKenna W. Stanford**

has been approved by the following supervisory committee members:

Adam Varble	, Chair	**09/21/2016** Date Approved
Edward Zipser	, Member	**09/21/2016** Date Approved
Steven Krueger	, Member	**09/21/2016** Date Approved

and by **Kevin D. Perry** , Chair/Dean of

the Department/College/School of **Atmospheric Sciences**

and by David B. Kieda, Dean of The Graduate School.

ABSTRACT

The High Altitude Ice Crystals - High Ice Water Content (HAIC-HIWC) field campaign produced aircraft retrievals of total condensed water content (TWC), hydrometeor particle size distributions, and vertical velocity (*w*) in high ice water content regions of tropical mesoscale convective systems (MCSs). These observations are used to evaluate deep convective updraft properties in high-resolution nested Weather Research and Forecasting (WRF) simulations of observed MCSs. Because simulated hydrometeor properties are highly sensitive to the parameterization of microphysics, three commonly used microphysical parameterizations are tested, including two bulk schemes (Thompson and Morrison) and one bin scheme (Fast Spectral Bin Microphysics).

A commonly documented bias in cloud-resolving simulations is the exaggeration of simulated radar reflectivities aloft in tropical MCSs. This may result from overly strong convective updrafts that loft excessive condensate mass and from simplified approximations of hydrometeor size distributions, properties, species separation, and microphysical processes. The degree to which the reflectivity bias is a separate function of convective dynamics, condensate mass, and hydrometeor size has yet to be addressed. This research untangles these components by comparing simulated and observed relationships between *w*, TWC, and hydrometer size as a function of temperature.

All microphysics schemes produce median mass diameters that are generally

larger than observed for temperatures between -10 °C and -40 °C and TWC > 1 g m^{-3}. Observations produce a prominent mode in the composite mass size distribution around 300 μm, but under most conditions, all schemes shift the distribution mode to larger sizes. Despite a much greater number of samples, all simulations fail to reproduce observed high TWC or high *w* conditions between -20 °C and -40 °C in which only a small fraction of condensate mass is found in relatively large particle sizes. Increasing model resolution and employing explicit cloud droplet nucleation decrease the size bias, but not nearly enough to reproduce observations. Because simulated particle sizes are too large across all schemes when controlling for temperature, *w*, and TWC, this bias is hypothesized to partly result from errors in parameterized microphysical processes in addition to overly simplified hydrometeor properties such as mass-size relationships and particle size distribution parameters.

In dedication to Norma A. Stevens for always encouraging me to look at the sky.

TABLE OF CONTENTS

ACKNOWLEDGEMENTS

I would like to thank my advisor, Adam Varble, for his guidance over the last two years. Your sense of intuition and passion for the science are inspiring. You have taught me how to relate subtle details to the big picture, a lesson I find positively ambiguous in its application to my career and life. I am thankful to my committee members, Ed Zipser and Steve Krueger, for providing valuable insight to the science and for helping me realize the importance of asking questions. I greatly appreciate funding from the National Science Foundation to perform this research, and thank the HAIC-HIWC scientists responsible for processing the multitude of data I used. I would also like to acknowledge the Center for High Performance Computing for providing the resources necessary to complete this work. I am especially grateful for the many friends who selflessly helped me adjust to a new city and life, and to my Zipser group colleagues for your insight through the research process. To my family, I am thankful for your unwavering love and support, and for remaining positive when I found it difficult to do so.

CHAPTER 1

INTRODUCTION

The utility of cloud resolving models (CRMs) is tied to their ability to adequately resolve cloud systems and associated latent heating budgets that are partially controlled by microphysical processes (Tao and Moncrieff, 2009). Indeed, the representation of clouds in models across a range of spatio-temporal scales impacts shortwave/longwave radiation budgets (Ramanthan et al., 1989; Hartmann et al., 2001) and the global hydrological cycle (Tiedtke, 1993). CRMs have considerably improved over the past few decades as computing power has increased and physics parameterizations have been refined using observations (e.g., Stoelinga et al., 2003). Very fine resolution ($\Delta x \sim 10^2$ m) is required to properly resolve mixing processes that impact convective dynamics and microphysics (Bryan et al., 2003); however, these large-eddy simulations (LES) are typically not feasible for most mesoscale modeling applications because of computing time and disk storage limitations. Therefore, CRMs and nested limited area models (LAMs) remain the workhorses of mesoscale meteorological research and forecasting. Climate research and forecasting requires even greater computing power, and thus, general circulation models (GCMs) have much coarser resolution ($\Delta x \sim 10^4 - 10^5$ m) that fails to resolve convective cloud processes. However, insertion of coarse resolution CRMs into GCM grid boxes through superparameterization is now commonplace

(Grabowski and Smolarkiewicz, 1999; Grabowski, 2001; Khairoutdinov and Randall, 2001; Randall et al., 2003). As computing power continues to increase and GCMs increase in resolution, they too will eventually reach cloud-resolving scales. Therefore, evaluating and improving CRMs and LAMs is of vital importance to improving weather and climate forecasting.

Many processes in CRMs operate on scales smaller than the model grid spacing, so-called sub-grid scale processes, that must be parameterized. Sub-grid scale parameterizations vary in sophistication and execution. High-order turbulence closures in a cumulus ensemble model (e.g., Krueger, 1988) may be used to parameterize turbulent processes in convective clouds, which in turn can be coupled with microphysical parameterizations through the implementation of a turbulent collision kernel in the stochastic collection equation (e.g., Benmoshe et al., 2012; Benmoshe and Khain, 2014). Parameterized microphysical processes impact energy budgets through latent heating and cooling, impacting large-scale circulations and distributions of heat, moisture, and aerosols in the troposphere (Schumacher et al., 2004). Unfortunately, assumptions and simplifications must be made in microphysical parameterizations, which use equations that are subject to many uncertainties and only empirically constrained by limited observations that fail to cover the large range of atmospheric conditions and cloud responses possible (Khain et al., 2015).

Improvement of numerical weather models and parameterizations has motivated many field experiments, with particular focus in the tropics because of its large contribution to global annual rainfall (Nesbitt et al., 2006). The Tropical Rainfall Measuring Mission (TRMM) Large-Scale Biosphere-Atmosphere (LBA) Experiment and

Kwajalein Experiment (KWAJEX) in 1999 used airborne instruments to measure microphysical characteristics in tropical convection (Stith et al., 2002, 2004) with remote sensing observational context. Rigorous validation of CRMs and LAMs using high-quality observations followed these and many other experiments, from which generalized model biases have emerged (Blossey et al., 2007; Lang et al., 2007; Li et al., 2008; Matsui et al., 2009; Varble et al., 2011, 2014a-b; and many others). Varble et al. (2011, 2014a-b) performed an intercomparison of CRM and LAM output with data from a scanning polarimetric C-band radar, vertical wind profilers, and surface disdrometers that were deployed during the Tropical Warm Pool-International Cloud Experiment (TWP-ICE) in Darwin, Australia in 2006 (May et al., 2008). These studies revealed high biases in convective reflectivity, vertical velocity, and area with low biases in stratiform rainfall across a suite of microphysics schemes for an active monsoon mesoscale convective system (MCS). They concluded that such biases are a result of many different complexly interacting components that include, but are likely not limited to, simple assumptions of hydrometeor properties, overly strong convective updrafts, and errors in environmental representation. Identifying the specific sources of convective biases requires in situ data that did not exist in TWP-ICE.

The High Altitude Ice Crystals - High Ice Water Content (HAIC-HIWC) (Dezitter et al., 2013; Strapp et al., 2015) joint field campaign was conducted with objectives ranging from identifying meteorological processes responsible for commercial aircraft engine malfunction (Lawson et al., 1998) to improving model microphysics parameterizations. The available dataset from the Darwin, Australia, phase is well-suited for the investigation of biases in simulated tropical convection, particularly because the

campaign targeted regions in and around convective updrafts with high ice water contents (> 2 g m^{-3}) and relatively low radar reflectivities (Leroy et al., 2016, hereafter L16). In particular, this dataset is ideal for investigating the overestimation of radar reflectivity aloft in simulated tropical oceanic convection that has been attributed to the lofting of large hydrometeors such as graupel (Blossey et al., 2007; Lang et al., 2007; Li et al., 2008; Matsui et al., 2009; Varble et al., 2011; Caine et al., 2013). Varble et al. (2014a) explored the possible contribution of vertical velocity to this bias, and concluded that overly strong convective updrafts in simulations were partially responsible for the reflectivity bias. However, they also found that the magnitude of this bias depends on the parameterization of microphysics and interaction of the parameterized microphysics with the biased convective dynamics. Microphysical parameterizations and convective dynamics are clearly linked to the reflectivity bias; however, these components have yet to be untangled. Furthermore, the individual contributions of hydrometeor type, size, and bulk mass to the reflectivity high bias have yet to be separated.

Ackerman et al. (2015) compared observations collected during several Airbus test flights during 2010-2012 in Cayenne, French Guiana, Darwin, Australia, and Santiago, Chile, (Grandin et al., 2014) with results from an idealized parcel model. However, this study was limited by the reliability of instrumentation (Fridlind et al., 2015) and focused exclusively on flight data around -40 °C. Lang et al. (2011) compared an improved version of the Goddard three-class ice (cloud ice, snow, and graupel) bulk microphysics scheme with observations taken during KWAJEX and TRMM-LBA. However, their study was limited to using remote-sensing data and focused on improving a single bulk microphysics scheme for the purpose of reproducing observed radar

reflectivity. The extent to which this bias is present in bin microphysics schemes has not been widely addressed, but Ackerman et al. (2015) show that a simulation using bin microphysics in the Distributed Hydrodynamic Aerosol and Radiative Modeling for Atmospheres (DHARMA) model failed to reproduce observed low reflectivity values in high ice water content regions, suggesting that this bias may exist in bin schemes as well.

The focus of this study is to compare hydrometeor sizes for given bulk mass and vertical velocity conditions so that the role of microphysical processes and assumed particle properties in producing model convective precipitation biases can be isolated from the roles of total condensate and vertical velocity biases. Mass size distributions (MSDs), which describe how total mass is distributed by particle size, are calculated in the schemes employed in this study so that comparisons are possible with observed MSDs. Analyzing both bulk and bin microphysics schemes provides insight into how biases differ between two fundamentally different approaches in microphysics parameterization. The effects of model horizontal resolution, explicit prediction of cloud droplet nucleation, and event considered for comparison with observations are also explored. Observations are described in Chapter 2, model setup in Chapter 3, intercomparison methodology in Chapter 4, results in Chapter 5, and conclusions in Chapter 6.

CHAPTER 2

HAIC-HIWC OBSERVATIONS

The High Altitude Ice Crystals - High Ice Water Content (HAIC-HIWC) field experiment was a result of objectives set by the Engine Harmonization Working Group (EHWG) to address aircraft engine rollback events in tropical deep convective environments. Lawson et al. (1998) hypothesized that a possible cause for these engine malfunctions is the ingestion of high mass concentrations of small ice crystals in glaciated clouds. These high ice water content (IWC) regions are likely produced and detrained from deep convective updrafts, and large regions of moderate-high IWC conditions are therefore possible in mesoscale convective systems (MCSs). The presence of these regions has been documented in co-location with areas of low radar reflectivity (Mason et al., 2006; Grzych and Mason, 2010; Mason and Grzych, 2011) that make them difficult to detect from conventional pilot's radar displays. In an effort to investigate the industrial and scientific aspects of these high IWC – low reflectivity regions, the HAIC-HIWC field campaign targeted cold cloud top regions of MCSs often associated with deep convective updraft cores for observation. The campaign consisted of two phases with the first in Darwin, Australia, from January to March of 2014 and the second in Cayenne, French Guiana, in May of 2015. This study primarily utilizes data from the Darwin campaign phase, which provides an ideal environment to investigate regions of

high IWC because of the tropical maritime conditions common during the active period of the monsoon season (Cifelli and Rutledge, 1998; May and Ballinger, 2007). HAIC-HIWC is one of many experiments exploring tropical phenomena in Darwin, including, but not limited to, TWP-ICE, the Darwin Area Wave Experiment (DAWEX) (Hamilton et al., 2004), the Island Thunderstorm Experiment (ITEX) (Keenan et al., 1989), the Down Under Doppler and Electricity Experiment (DUNDEE) (Rutledge et al., 1992), the Equatorial Mesoscale Experiment (EMEX) (Webster et al., 1991), the Stratosphere-Troposphere Exchange Project (STEP) (Russell et al., 1993), and the Maritime Continent Thunderstorm Experiment (MCTEX) (Keenan et al., 2000). Limited data from the Cayenne phase are briefly shown to fortify results from Darwin, but more detailed comparison of the Darwin and Cayenne datasets is left for future studies.

The SAFIRE[1] Falcon 20 research aircraft managed 23 flights through tropical MCS events during the Darwin campaign and was equipped with a variety of instrumentation used to collect in situ and W-band radar data. However, only the instrumentation used for the current study are described here. Particle images used for derivations of particle size distributions (PSDs) were obtained by two optical array probes (OAPs), including the 2D-Stereo probe (2D-S, Lawson et al., 2006) from SPEC Inc. and the Precipitation Imaging Probe (PIP, Baumgardner et al., 2011) from Droplet Measurement Technologies. The 2D-S was primarily used for the measurement of particles with diameters less than 1280 μm with a resolution of 10 μm, while the PIP measured particles up to 6400 μm, but at a coarser resolution of 100 μm. A linearly weighted composite size distribution using area-equivalent diameters described in L16 is

1 Service des Avions Francais Instrumentes pour la Recherche en Environnement

used for the current dataset. The OAPs were equipped with antishattering tips to avoid ice fragmentation and an interarrival time algorithm was used to remove potentially shattered particles (Field et al., 2003; Korolev and Isaac, 2005; Heymsfield, 2007).

Bulk TWC measurements were made with an isokinetic evaporator probe (IKP2) from Science Engineering Associates (SEA) Inc. (Strapp et al., 2016) engineered for high IWC conditions, which provides more reliable retrievals than other datasets that use mass-size power law assumptions. The IKP2 uses a differential hygrometry method in calculating TWC that accounts for background water vapor. Further detail of microphysical instrumentation aboard the Falcon 20 may be found in L16.

Vertical velocities (w) were calculated by SAFIRE using a method similar to that of Jorgensen and LeMone (1989), in which vertical velocity is defined as the difference between the vertical motion of the aircraft relative to the ground and relative to the air. The vertical motion with respect to air is calculated using the aircraft's true air speed along with attack, side-slip, pitch, and roll angles, the former two of which are measured using differential pressure measurements and the latter two using inertial navigation measurements. Errors in w calculations are restricted to ~ 1 m s^{-1}.

L16 use retrieved TWC with retrieved PSDs to constrain mass-size relationships ($m = \alpha D^{\beta}$, in which D is particle diameter and $\alpha = \frac{\pi}{6}\rho_i$ where ρ_i is the bulk density of the i^{th} hydrometeor species) in calculating MSDs over 5-second sampling intervals. The particle diameter used in this study is the 2D area equivalent diameter (D_{eq}), defined as the diameter of a circle with the same area as particle images from the OAPs. L16 show that observed median mass diameters (MMDs, defined as the diameter at the median percentile of the MSD) can vary by more than 20% depending on how diameter is

defined (e.g., mean chord length, box length, maximum dimension, or area equivalent diameter). D_{eq} was chosen for this study because it is the most similar to diameter definitions within the microphysics schemes. The exponent β in the mass-size relationship is constrained by relating it to the exponents in area-size and perimeter-size relationships derived from OAP images, which allows it to vary as a function of time by accounting for changing crystal habits along flight trajectories. Moreover, α was constrained in the mass-size relationship by matching the integrated MSD to TWC measurements from the IKP2. The available PSD and MSD dataset described by L16 permits comparisons of simulated and observed hydrometeor properties in the context of TWC and *w* that are much more uncertain and less detailed in remote-sensing retrievals, which need to make numerous assumptions. However, because an objective of this study is to investigate well-known reflectivity biases, data from a C-band scanning dual-polarimetric radar (C-POL) (Keenan et al., 1998) located near Darwin are utilized for Flight 23 on 18 February 2014 in an MCS event, one of the only events that occurred within range of the radar (see Section 5.1 for more detail).

CHAPTER 3

MODEL

3.1 Model setup

The Advanced Research Weather Research and Forecasting (WRF-ARW) V3.6.1 model (Skamarock et al., 2008) is used to perform a suite of simulations with varying microphysics schemes and tropical MCS cases. The Bureau of Meteorology's (BOM) Australian Community Climate and Earth-System Simulator Regional model (ACCESS-R) analyses are used as large-scale forcing. These three-hourly analyses have ~12 km horizontal grid spacing. WRF-ARW's dynamical core uses an Eulerian solver for the fully compressible nonhydrostatic equations with a 3rd order Runge-Kutta time integration technique on a staggered Arakawa C-grid. Physics parameterizations common to all simulations performed include the Mellor-Yamada-Janjic (MYJ) planetary boundary layer (PBL) scheme (Janjic, 1994), the Rapid Radiation Transfer Model (RRTM) longwave radiation scheme (Mlawer et al., 1997), the Dudhia (1989) shortwave radiation scheme, the Kain-Fritsch cumulus scheme (Kain, 2004), and the Noah Land Surface Model (Chen and Dudhia, 2001). All of the simulated MCS events use 9:3:1-km two-way nesting with 92 vertical levels and the 1000-m grid spacing domain is used for most analyses. However, analysis of an additional embedded 333-m horizontal grid spacing domain with 182 vertical levels in the 18 February case is also performed. This

higher resolution domain uses 1.5-order turbulent kinetic energy turbulence closure, whereas the coarser domains use a 2-D Smagorinsky scheme for horizontal mixing and the PBL parameterization for vertical mixing.

3.2 Microphysics schemes

Three commonly used microphysics schemes are employed in this study, including the Thompson (Thompson et al., 2008) and Morrison (Morrison et al., 2009) bulk microphysics schemes and the Hebrew University Fast Spectral Bin Microphysics (FSBM) scheme (Lynn et al., 2005). Descriptions of the predicted hydrometeor species in each scheme are shown in Table 3.1. The bin microphysics scheme explicitly solves a set of microphysical equations for mass bins separately for aerosols, liquid, graupel/hail, and cloud ice/snow, and each mass bin has a corresponding particle diameter. It therefore makes no assumptions about the shape of PSDs and calculates process rates for each bin rather than entire PSDs. The primary weakness of bin schemes are their high computational costs relative to bulk schemes, which predict only integral moments of the PSDs. Single moment (1M) bulk schemes typically predict the mass mixing ratio (q) of a number of hydrometeor species and double moment (2M) schemes typically predict both q and number concentration (N). Although not included in this study, three-moment schemes usually predict Rayleigh reflectivity as a third moment of the PSD (e.g., Milbrandt and Yau, 2005, 2006). Bulk scheme PSDs are typically represented by a gamma function of the following form:

$$N(D) = N_0 D^{\mu} e^{-\lambda D} \tag{3.1}$$

where N_0 is the intercept parameter, D is the particle diameter, μ is the shape parameter,

and λ is the slope parameter (units of m^{-1}). μ is typically set to a constant, and if set to 0, then the PSD is exponential. λ depends on predicted bulk mass, and for 2M schemes, λ and N_0 depend on the number concentration. N_0 can be thought of as controlling the number of small particles for a given bulk mass, whereas μ controls the PSD dispersion and λ controls the PSD slope. The range of possible values for these parameters are typically based on fits to available observations (Pruppacher and Klett, 1997).

The Thompson and Morrison bulk schemes predict moments of the PSD for five hydrometeor species, including cloud ice, cloud water, rain, snow, and graupel. The Morrison scheme is primarily a 2M scheme, predicting N for graupel, rain, snow, and cloud ice, whereas the Thompson scheme only predicts N for cloud ice and rain. Field et al. (2005) describe the bimodal gamma snow size distribution that varies as a function of temperature that is utilized in the Thompson scheme. The Morrison scheme assumes spherical particles and assigns a bulk density for all ice species given by Reisner et al. (1998). While a bulk density is assumed for the hybrid graupel-hail species in the Thompson scheme, it uses a nonspherical mass-size power law relationship for snow, as presented in Cox (1988) that allows for the bulk density of snow to vary with particle size. Varble et al. (2014a) showed that this relationship (where $m \propto D^2$) reproduces observed reflectivity better than schemes assuming $m \propto D^3$ for snow and supports surface disdrometer (Mitchell et al., 1990) and aircraft (Westbrook et al., 2004) observations of snow particles. Although graupel/hail N is not predicted in the Thompson scheme, it uses a variable N_0 that varies inversely as a function of the predicted mass mixing ratio and shifts the fall-speed relationship from graupel toward hail as particle size increases. For the versions of the Morrison and Thompson schemes used in this study, $\mu = 0$ for rain,

graupel, and cloud ice, but is variable for cloud water. For snow, $\mu = 0$ for Morrison, but is nonzero in the Thompson scheme. Lastly, this study uses a constant cloud droplet number concentration of 100 cm^{-3} in both bulk schemes that is typical of the clean tropical maritime air masses commonly observed in Darwin. A summary of the bulk scheme MSD parameters may be found in Table 3.2 for Thompson and Table 3.3 for Morrison.

The FSBM scheme uses 33 mass-doubling bins to represent the mass (size) distributions, and process rates are computed separately for each bin. The fast SBM scheme differs from the full SBM scheme (Khain and Sednev, 1996; Khain et al., 2000) by decreasing the number of ice size distributions to be solved from 6 to 2. Both the full and fast versions of the scheme solve equations for size distributions representing cloud condensational nuclei (CCN) and liquid water (which includes both rain drops and cloud droplets). However, instead of solving equations separately for 3 types of ice crystals (including plates, columns, and dendrites, which vary as a function of temperature, Takahashi et al., 1991) and 3 large ice species (aggregates, hail, and graupel), the fast version combines dendrites with snow, columnar crystals with graupel, and platelike crystals with hail, increasing computational efficiency by simplifying ice crystal depositional growth representations (Lynn et al., 2005). It also explicitly represents cloud droplet nucleation and is able to maintain supersaturations over liquid should the environmental conditions demand it. The inclusion of aerosol activation by the FSBM scheme offers an advantage over the bulk schemes discussed above because of the effects that aerosol concentrations and activity can have on convective cloud systems (Kaufman and Nakajima, 1993; Khain et al., 1999; Harshvardhan et al., 2002). Initial CCN

concentrations in the FSBM scheme are set to resemble the maritime environment in Darwin during the active period of the monsoon season. CCN concentrations in the boundary layer are ~100 cm^{-3} and decrease exponentially with height to about 50 cm^{-3} at 4-km altitude and to less than 10 cm^{-3} at 9 km altitude. The influence of aerosols on clouds and precipitation was also considered in a new version of the Thompson scheme (Thompson and Eidhammer, 2014) by the prediction of available aerosols for cloud ice and droplet nucleation (i.e., making cloud water a double moment species). To test the impact of this change, a sensitivity test was performed using the Thompson "aerosol-aware" (AA) version, and is described in Section 5.4.3. In both the Thompson AA and FSBM schemes, CCN concentrations become quite variable as they are advected, consumed by hydrometeors, and reintroduced through evaporation.

3.3 Simulated events

Four events from the HAIC-HIWC campaign are simulated. The flight tracks of these events are shown in Figure 3.1 overlaid on infrared imagery from the Multifunctional Transport Satellites 1R (MTSAT-1R) satellite. Included are MCSs sampled during Flight 6 on 23 January 2014 (Figure 3.1a), Flights 12-13 from 2-3 February 2014 (Figure 3.1b), Flight 16 on 7 February 2014 (Figure 3.1c), and Flight 23 on 18 February 2014 (Figure 3.1d). Several attempts were also made to simulate the 29 January 2014 MCS (Flight 10), but a system similar to that observed could not be simulated. Each of these events were sampled at varying temperature levels from -10 °C to -50 °C through updraft cores and high TWC regions exceeding 2 g m^{-3} on 10-km scales and 3.5 g m^{-3} on 1-km scales.

All four events were simulated with both Morrison and Thompson microphysics schemes. However, as presented in Section 5.4.1, simulated hydrometeor properties vary little between events when controlling for *w* and TWC. Therefore, the primary case analyzed is the 18 February MCS (Flight 23), which contains the most flight observations near -10°C and flight legs within range of C-POL. The 450-km by 540-km inner domain (1000-m grid spacing) for this case is shown in Figure 3.2, and was run from 00Z on the 18th to 06Z on the 19th. Additionally, a 240-km by 200-km domain with 333-m grid spacing (see Figure 3.2) is run to test resolution sensitivity. The 333-m grid spacing simulation is not run as an original nested domain, but rather as a single domain forced by output from the 1000-m simulation and run from 12Z on the 18th to 00Z on the 19th. The sensitivity run using the Thompson AA scheme is also only run for the 18 February case, and because of the high computational cost of running FSBM for a mesoscale domain, this is the only case simulated using FSBM.

Table 3.1. Description of each scheme's representation of explicit aerosol activation, dense rimed ice species, vapor-grown ice species, and liquid water species. For bulk schemes (Thompson, Morrison, and Thompson AA), the number of PSD moments predicted for that species is shown in parentheses. Note that the bulk schemes require separation of liquid water species (cloud water and rain) and vapor-grown ice species (cloud ice and snow), whereas FSBM is not subject this distinction. For FSBM and Morrison, graupel or hail may be chosen. This study uses the graupel option for both schemes.

Microphysics Scheme Descriptions				
Scheme	Explicit Aerosol Activation	Dense Rimed Ice Species	Vapor-grown Ice Species	Liquid Water Species
Thompson	No	graupel-hail hybrid (1M)	snow (1M) and cloud ice (2M)	rain (2M) and cloud water (1M)
Morrison	No	graupel (2M)	snow (2M) and cloud ice (2M)	rain (2M) and cloud water (1M)
FSBM	Yes	graupel	snow-cloud ice hybrid	rain-cloud water hybrid
Thompson AA	Yes	graupel-hail hybrid (1M)	Snow (1M) and cloud ice (2M)	rain (2M) and cloud water (2M)

Table 3.2. Parameters in the Thompson mass-size relationships ($m = \alpha D^{\beta}$) and gamma PSD parameters for each species. N_c used for cloud water μ and N_0 calculations is set to a constant 100 cm^{-3}. N_0 equations for 2M species are determined by prognostic N and q. The bimodal gamma distribution used for the Thompson snow PSD may be found in Thompson et al. (2008), Equation 1.

Thompson MSD parameters						
Species	Prognostic Variables	ρ [kg m^{-3}]	α	β	N_0 [m^{-4}]	μ
Snow	q_s	$\frac{6\alpha_s}{\pi} D^{\beta_s-3}$	0.069	2	-	0.6357
Graupel	q_g	500	$\frac{\pi\rho_g}{6}$	3	$max\left[10^4, \min\left(\frac{200}{q_g}, 3 \times 10^6\right)\right]$	0
Cloud Ice	q_i, N_i	890	$\frac{\pi\rho_i}{6}$	3	$\frac{N\lambda^{\mu+1}}{\Gamma(\mu+1)}$	0
Rain	q_r, N_r	1000	$\frac{\pi\rho_w}{6}$	3	$\frac{N\lambda^{\mu+1}}{\Gamma(\mu+1)}$	0
Cloud Water	q_c	1000	$\frac{\pi\rho_w}{6}$	3	$\frac{N_c\lambda^{\mu+1}}{\Gamma(\mu+1)}$	$\min(15, \frac{10^9}{N_c} + 2)$

Table 3.3. Parameters in the Morrison mass-size relationships ($m = \alpha D^{\beta}$) and gamma PSD parameters for each species. N_c used for cloud water μ and N_0 calculations is set to a constant 100 cm^{-3}. Cloud water μ is calculated as a function of N_c using an empirical relationship described in Martin et al. (1994).

Morrison MSD parameters						
Species	Prognostic Variables	ρ [kg m^{-3}]	α	β	N_0 [m^{-4}]	μ
Snow	q_s, N_s	100	$\frac{\pi\rho_s}{6}$	3	$\frac{N\lambda^{\mu+1}}{\Gamma(\mu+1)}$	0
Graupel	q_g, N_g	400	$\frac{\pi\rho_g}{6}$	3	$\frac{N\lambda^{\mu+1}}{\Gamma(\mu+1)}$	0
Cloud Ice	q_i, N_i	500	$\frac{\pi\rho_i}{6}$	3	$\frac{N\lambda^{\mu+1}}{\Gamma(\mu+1)}$	0
Rain	q_r, N_r	997	$\frac{\pi\rho_w}{6}$	3	$\frac{N\lambda^{\mu+1}}{\Gamma(\mu+1)}$	0
Cloud Water	q_c	997	$\frac{\pi\rho_w}{6}$	3	$\frac{N_c\lambda^{\mu+1}}{\Gamma(\mu+1)}$	-

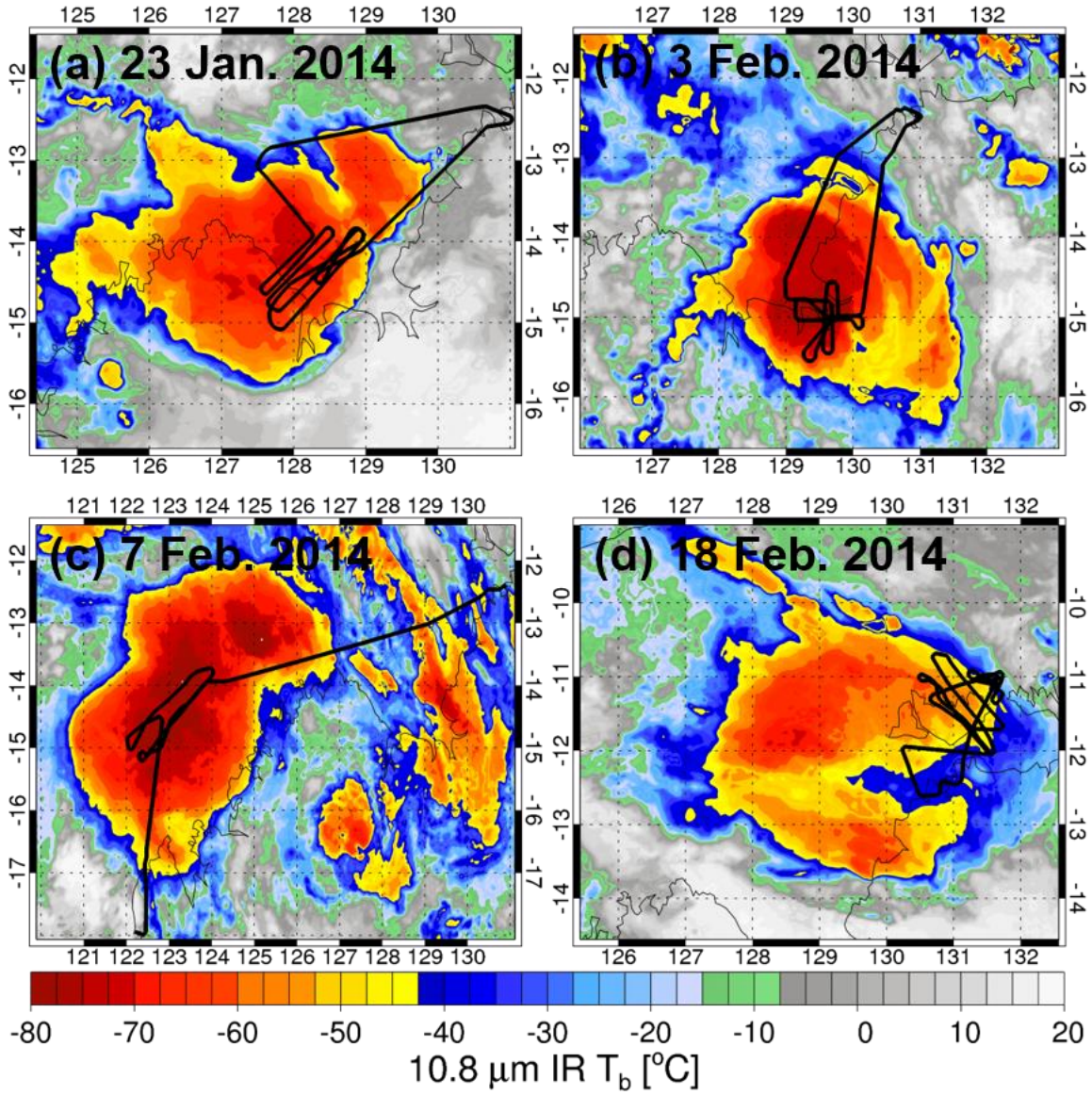

Figure 3.1. Flight tracks (black lines) for (a) Flight 6 on 23 January 2014, (b) Flight 13 on 3 February 2014, (c) Flight 16 on 7 February 2014, and (d) Flight 23 on 18 February 2014 overlaid on IR imagery from MTSAT-1R representative of the MCS lifecycle stage when it was sampled. Note that both Flights 12 and 13 flew through the same system (2-3 February), but only Flight 13 is shown.

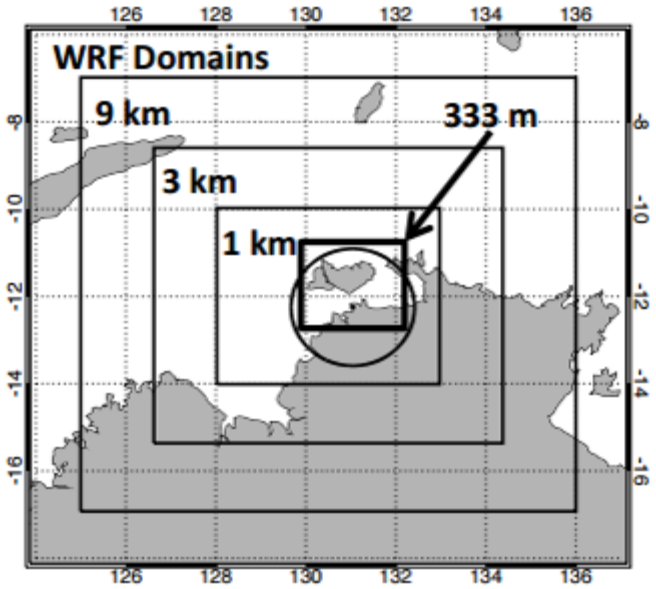

Figure 3.2. The WRF domains used for the 18 February 2014 simulation. The circle indicates the 150-km range ring of the C-POL radar.

CHAPTER 4

METHODOLOGY AND LIMITATIONS

4.1 Methodology

Each simulated event is sampled in a six-hour time period covering the flight leg times during the mature and/or decaying stages of the MCS within the 1000-m domain. For the 18 February event, the time period chosen is 18Z on the 18th to 00Z on the 19th. Four primary variables are analyzed: temperature (T), TWC, *w*, and percentiles of the mass size distribution (i.e., 10% mass diameter, MMD, and 90% mass diameter). For the simulations, TWC and mass diameters are calculated for individual and combined species, whereas species are not separated in the observations. However, L16 state that only trace amounts of liquid water content (LWC) were detected for a few flights at relatively warmer temperatures (T > -20 °C), and thus, TWC is a proxy for IWC in the vast majority of observed situations.

Comparison of simulation output and measurements are confined to grid points representative of convective updrafts, defined where (1) $w \geq 1$ m s^{-1} and (2) condensate mass mixing ratio > 10^{-12} kg kg^{-1}. Because this study focuses on biases primarily associated with ice microphysics and observations are limited to sub-freezing temperatures, only grid points where -60 °C ≤ T ≤ 0°C are analyzed. With these

constraints, grid point sample sizes for individual simulated events are greater than 10^6. Evaluating convective updraft properties using grid points rather than average and maximum values of "cores" defined as contiguous points where $w \geq 1$ m s^{-1} diverges from a number of previous studies (Zipser and LeMone, 1980; Lucas et al., 1994; Varble et al., 2011, 2014a, b). However, T, *w*, and TWC relationships for cores have very similar results to those for individual grid points using the above metrics (not shown). Grid points also have the advantage of matching kinematic and microphysical properties in space at the highest resolution possible. While simulated events are analyzed for a domain with 1000-m horizontal grid spacing, PSDs are retrieved using 5-second sampling windows, which corresponds to a grid spacing of ~750 m assuming a typical aircraft speed of 150 m s^{-1}. This could contribute to differences between observations and simulations, though results from reduced horizontal grid spacing of 333-m suggest that differences would not significantly contribute to the overall differences between simulations and observations.

Strapp et al. (2015) describe the sampling strategy of the Falcon 20 aircraft during the HAIC-HIWC campaign, which consisted of targeting regions of tropical MCSs with cold infrared brightness temperatures observed by satellite. Many legs penetrated convective updraft cores or regions downstream of updraft cores around -40 °C and -30 °C temperature levels, with fewer flight legs performed around -50 °C and -10 °C levels. The Cayenne dataset increases sample sizes at all levels with data from both the Falcon 20 and the Environment Canada Convair aircraft, particularly around -10 °C, but is only used in this study to provide context to conclusions drawn from the Darwin dataset because of its only recent release.

4.2 Calculation of variables from model output

Several variables are computed from model output for comparison with observations. The PSD (units of m^{-4}) is computed using Equation 3.1 for bulk schemes and is outputted directly by the bin scheme. The mass-size distribution parameters for bulk schemes (i.e., αD^{β} and gamma PSD parameters) are detailed in Tables 3.2 and 3.3 for the Thompson and Morrison schemes, respectively. For the FSBM scheme, all particles are spherical, graupel has a bulk density of 400 kg m^{-3}, and liquid has a bulk density of 1000 kg m^{-3}. The density of vapor-grown ice in FSBM varies from 900 kg m^{-3} to 35 kg m^{-3} for increasing particle size.

In Equation 3.1, N_0, the size intercept for 2M bulk species represented by a gamma PSD, is calculated using Equation 4.1:

$$N_0 = \frac{N\lambda^{\mu+1}}{\Gamma(\mu+1)} \tag{4.1}$$

where Γ is the Euler gamma function, N is the particle number concentration, μ is the shape parameter of the gamma PSD, and λ is the slope of the gamma PSD. For 1M species in bulk schemes, N_0 is diagnostic, but may vary as a function of prognostic variables such as temperature (e.g., Thompson scheme snow) or mass mixing ratio (e.g., Thompson scheme graupel). For 2M species, λ is calculated using Equation 4.2:

$$\lambda = \left[\frac{\alpha N\Gamma(\mu+\beta+1)}{\mathrm{q}\Gamma(\mu+1)}\right]^{\frac{1}{\beta}} \tag{4.2}$$

where q is the mass mixing ratio and α and β are the mass-size relationship parameters in the mass-size power law relationship $m = \alpha D^{\beta}$. λ for 1M species may also be calculated using Equation 4.2 for diagnostic N based on N_0 in Equation 4.1 and prognostic q.

Mass-size distributions (units of kg m^{-4}) are calculated by multiplying a scheme's

PSD by its mass-size relationship, as shown in Equation 4.3:

$$M(D) = \alpha D^{\beta} N(D) \tag{4.3}$$

Because the observed MSD dataset is not separated by individual species, observations are compared with the combined MSD of all hydrometeors in the scheme. The combined MSD, $M(D)_{tot}$, is calculated using Equation 4.4:

$$M(D)_{tot} = \sum_{i=1}^{n} \alpha_i D^{\beta_i} N_i(D) \tag{4.4}$$

where *n* is the number of species in the microphysics scheme. For the evaluation of mass partitioning between species in bulk schemes (see Section 5.2.1), liquid MSDs are the combination of cloud water and rain MSDs and vapor-grown ice MSDs are the combination of cloud ice and snow MSDs. For FSBM, there is intrinsically no separation between cloud water and rain or between cloud ice and snow.

Percentile mass diameters of each hydrometeor species are calculated by numerically integrating the MSD from 0 to the mass diameter where the integrated mass equals the desired percentage of total mass. For example, the combined hydrometeor MMD is calculated using Equation 4.5:

$$\int_0^{MMD} \alpha D^{\beta} N(D) dD = \frac{1}{2}\left[\sum_{i=1}^{n} \int_0^{\infty} \alpha_i D^{\beta_i} N_i(D) dD\right] = \frac{1}{2} TWC \tag{4.5}$$

where *n* is the total number of species in a single scheme. Integration from 0 to 10% MD or 90% MD would then be equal to 0.1×TWC and 0.9×TWC, respectively.

Equivalent Rayleigh reflectivity factor (Z_e) size distributions (ZSDs) are calculated by multiplying the 6th power of the melted equivalent diameter (D_{eq}) by the PSD. The melted equivalent diameter is given by Equation 4.6:

$$D_{eq} = \left[\frac{6\alpha}{\pi\rho_w}\right]^{\frac{1}{3}} D^{\frac{\beta}{3}} \tag{4.6}$$

where ρ_w is the bulk density of water. $D = D_{eq}$ for liquid water particles, and for spherical ice particles with constant bulk density, D_{eq} reduces to Equation 4.7:

$$D_{eq} = \left[\frac{\rho_i}{\rho_w}\right]^{\frac{1}{3}} D \tag{4.7}$$

where ρ_i is the bulk density of the ith hydrometeor species. The ZSD can then be computed using Equation 4.8:

$$Z_e(D) = 0.224\times10^{18}\left[\frac{6\alpha}{\pi\rho_w}\right]^2 D^{2\beta}N(D) \tag{4.8}$$

where 10^{18} is a conversion factor from m^6 to mm^6 and 0.224 is a factor accounting for the different dielectric constants of ice and liquid, following Smith (1984). For the jth liquid water species, Equation 4.8 reduces to Equation 4.9:

$$Z_e(D)_j = 10^{18} D^6 N_j(D) \tag{4.9}$$

where the ZSD has units of mm^6 m^{-4}. The combined ZSD, $Z_e(D)_{tot}$, is then calculated using Equation 4.10:

$$Z_e(D)_{tot} = 10^{18}\left[0.224\sum_{i=1}^{n}\left(\frac{6\alpha_i}{\pi\rho_w}\right)^2 D^{2\beta_i}N_i(D) + \sum_{j=1}^{m} D^6 N_j(D)\right] \tag{4.10}$$

where *n* is the number of ice species and *m* is the number of liquid species. Rayleigh equivalent reflectivity factor for each scheme is calculated by summing the integrated ZSD of *n* ice species and *m* liquid water species, as shown in Equation 4.11:

$$Z_e = 10^{18}\left[0.224\sum_{i=1}^{n}\int_0^{\infty}\left(\frac{6\alpha_i}{\pi\rho_w}\right)^2 D^{2\beta_i}N_i(D)dD + \sum_{j=1}^{m}\int_0^{\infty} D^6 N_j(D)dD\right] \tag{4.11}.$$

4.3 Limitations and caveats

Despite relatively long flight transects through MCSs at varying altitudes, several limitations exist in the observational datasets. For example, many flights are in MCSs that are in decaying stages after sunrise. Flight 23 (Figure 3.1d) began sampling around 22Z, several hours after the most intense convective bursts around 17Z (not shown). Moreover, data were collected in MCSs that varied in thermodynamic and kinematic structure. For example, Flights 16 and 23 (Figures 3.1c and 3.1d, respectively) sampled MCSs with convectively intense squall lines, while Flights 12 and 13 (Figure 3.1b) sampled a long-lived tropical low with much weaker, but equally deep convection. Because of a lack of significant lightning and high reflectivity during Flights 12-13, the aircraft was able to sample the most intense convective regions, whereas Flight 16 avoided the most intense cells with high reflectivity and lightning, sampling portions of the squall line that were in decaying stages.

The comparison of a single simulated event with flight data from the entire Darwin campaign may present a bias in comparisons, but was done because of the small sample size in any single event flown. However, the comparison of different simulated events with each other presented in Section 5.4.1 suggests that this bias is likely small. A more significant source of biased comparisons is the subjective observational sampling. Regions with lightning or “red” on the pilot’s X-band radar display (reflectivity exceeding 40 dBZ) were avoided during flights, and these regions likely contain the most intense convective cells with the most graupel and liquid water (e.g., Zipser and Lutz, 1994). This sampling cannot be replicated in simulations because of the previously mentioned biases in simulated reflectivity and the lack of lightning in simulations.

Additionally, simulating every event observed with multiple model setups is not computationally feasible. The possible effects of this bias on interpretation of results are discussed further in subsequent sections.

CHAPTER 5

RESULTS

5.1 Radar reflectivity

Representative cross-sections of Rayleigh reflectivity at 18Z on 18 February 2014 are shown in Figures 5.1-5.3 for 2.5-, 7-, and 10.75-km altitudes, respectively. Observed C-POL reflectivity is shown in (a) and derived reflectivities in the Thompson, Morrison, and FSBM schemes are shown in (b-d), respectively. Clear differences exist in the vertical reflectivity structure of the simulated MCSs between different microphysics schemes. Observed reflectivities at 2.5-km altitude reach a maximum of ~ 45 dBZ in the most intense convective cores covering a small area, but reflectivity values ranging from 25-35 dBZ are much more common across the region. Both bulk schemes at this altitude produce much more widespread high reflectivities that exceed 50 dBZ, and the Morrison scheme produces some reflectivities in convective cores that exceed 55 dBZ. The FSBM scheme recreates the observed reflectivity at this altitude considerably well, though the MCS is somewhat less organized at this time compared to the observed event. At 7-km altitude (Figure 5.2) corresponding to ~ -10 °C, observed reflectivities remain below 20 dBZ across the majority of the domain, with the strongest cores approaching 35 dBZ. All simulations produce reflectivities exceeding 45 dBZ at 7-km altitude. While the Thompson scheme produces the highest reflectivity values at 7-km, the cores of high

reflectivity are much smaller than in the Morrison and FSBM schemes. The Morrison scheme has maximum reflectivities of less than 48 dBZ, while the FSBM scheme produces much more widespread regions of reflectivity exceeding 50 dBZ. Observed convective core reflectivities are significantly reduced at 10.75-km altitude (Figure 5.3a), whereas all simulations produce much higher reflectivities (Figures 5.3b-d). The Morrison scheme produces the largest spatial extent of reflectivity values exceeding 20 dBZ at this altitude, whereas the Thompson scheme reflectivities remain mostly below 15 dBZ away from the highest values that approach 35 dBZ in concentrated cores. The FSBM scheme produces much smaller areas of elevated reflectivity compared to the bulk schemes except for a few cores that exceed 40 dBZ. Clearly, every microphysics scheme struggles in capturing the observed vertical reflectivity profile, and every scheme differs significantly from the others.

Percentile profiles of radar reflectivity for the 18 February MCS are shown in Figure 5.4 to further examine the vertical profile of reflectivity and to establish that biases in radar reflectivity exist in the current study. The model data have been interpolated to constant altitudes where C-POL data are available and only data points where reflectivity > 5 dBZ are included. Figures 5.4a and 5.4c show the 90^{th} percentile of reflectivity, and Figures 5.4b and 5.4d show the 99^{th} percentile. Figures 5.4a-b show 15Z profiles when the MCS was growing and convection was most intense, while Figures 5.4c-d show 19Z profiles during the mature stage of the MCS.

Figure 5.4 indicates that the 90^{th} and 99^{th} percentiles of simulated radar reflectivity values exceed those of observations across much of the troposphere. This bias does not relax over the lifetime of the MCS, and is especially present above the melting

level, but still exists to varying degrees down to the surface. Both bulk schemes consistently exaggerate reflectivities below the melting level, while the FSBM scheme performs best in liquid regions. Figures 5.4b and 5.4d show that all schemes produce reflectivities at the 99th percentile that exceed observations by up to 15 dBZ or greater between 5 and 15 km.

Although reflectivity is overestimated in amplitude, the vertical structure of the reflectivity is reproduced to varying degrees of accuracy by the simulations. The Thompson scheme best reproduces the vertical structure, especially in replicating the negative slope of the profile between the melting level and the homogeneous freezing region. Thompson also performs much better in the latter stages of the MCS lifecycle in comparison to the other schemes for the 90th percentile. The Morrison scheme typically captures the vertical profile better than FSBM, and exhibits larger reflectivities than the Thompson scheme at the 90th percentile, but the lowest reflectivities below freezing at the 99th percentile.

5.2 Relationships between T, W, TWC, and MMD

The partitioning of bulk condensate mass between hydrometeor species provides guidance for which species contribute most to reflectivity biases. Varble et al. (2011) found that graupel water content (GWC) and snow water content (SWC) contributions to Rayleigh reflectivity biases were strongly modulated by assumed size distribution parameters (N_0, μ, and λ) and the number of PSD moments predicted in bulk schemes. For example, diagnostically varying N_0 in the assumed graupel PSD of a 1M scheme aided in reducing the graupel contribution to high reflectivity biases by allowing for

higher number concentrations of small graupel particles for a given GWC. Predicting *N* in addition to *q* in the Morrison microphysics scheme generally reduced the graupel contribution to the reflectivity high bias, but larger snow sizes resulting from prognostic *N* increased snow's contribution to the bias. Although fewer assumptions are made regarding PSDs in the FSBM scheme, separate hydrometeor species with parameterized particle properties and microphysical processes still contribute to potential model biases. High biased reflectivities also result from exaggerated simulated convective updraft vertical velocities, which loft excessive condensate mass with hydrometeor PSD assumptions modulating the bias (Varble et al., 2014a). Therefore, it is necessary to control for *w* and TWC to isolate the role of hydrometeor size in producing the reflectivity high bias. This is accomplished by analyzing a phase space consisting of TWC, *w*, temperature, and median mass diameter (MMD).

5.2.1 Simulated relationships and species partitioning

Figure 5.5 shows variable-filled joint histograms for the 18 February simulated MCS, where the abscissa is *w*, the ordinate is temperature (T) below freezing, and average bulk mass (g m^{-3}) for various species are color-filled in *w*-T bins. The Thompson scheme is shown in Figures 5.5a-d, the Morrison scheme in Figures 5.5e-h, and the FSBM scheme in Figures 5.5i-l. TWC (all hydrometeor species added together) is shown in Figures 5.5a, 5.5e, and 5.5i; SWC (including cloud ice) is shown in Figures 5.5b, 5.5f, and 5.5j; GWC is shown in Figures 5.5c, 5.5g, and 5.5k; and LWC is shown in Figures 5.5d, 5.5h, and 5.5l. Figure 5.5 can be thought of as showing a vertical profile of condensate and its partitioning among different hydrometeor species for a given *w*.

Both bulk schemes and the bin scheme produce TWCs that increase with increasing temperature and *w*. For most *w*-T bins, the Morrison scheme produces the largest mean TWCs, reaching 4 g m^{-3} or greater at *w* exceeding 15 m s^{-1} and temperatures between 0 °C and -30 °C. The largest species contribution to TWC in Morrison is from graupel, where mean GWC greater than 2.5 g m^{-3} occurs over a wide range of values in *w*-T space (Figure 5.5g). The Thompson and FSBM schemes have lesser graupel production (Figures 5.5c and 5.5k), only reaching mean GWCs of 2.5 g m^{-3} at temperatures warmer than -20 °C and *w* above 15 m s^{-1}. Thompson and FSBM produce the highest mean SWC of 1.5-2 g m^{-3} at temperatures below -20 °C (Figures 5.5b and 5.5j). However, note that the FSBM simulation yields higher SWC at higher *w* and temperatures warmer than -30 °C. The Morrison scheme produces mean SWCs below 1 g m^{-3} across the entire *w*-T space because of the dominance of graupel. The largest rain and cloud water contents are lofted into the mixed-phase region by the Thompson scheme (Figure 5.5d), while the FSBM scheme has lesser amounts of liquid water lofted above -8 °C (Figure 5.5l). The Morrison scheme lofts a smaller amount of rain water content (RWC) just above the melting level compared to Thompson, but both bulk schemes loft much more cloud water than the bin scheme, which may impact riming processes.

Investigating hydrometeor size in conjunction with mass content is more revealing. Figure 5.6 shows variable-filled joint histograms similar to Figure 5.5, but the color-fill is mean hydrometeor MMD. Several patterns emerge in comparison with Figure 5.5. The Thompson scheme's snow dependency on temperature is clearly visible in Figure 5.6b, where a low-level maximum in mean snow MMD of 1-3 mm occurs at temperatures warmer than -20 °C and *w* weaker than 10 m s^{-1}, and decreases to snow

particles smaller than 0.5 mm at most temperatures below -30 °C across all *w*. The FSBM scheme produces similar results to the Thompson scheme, where snow MMD increases with increasing temperature but decreasing *w*. However, the FSBM scheme does not diagnostically force snow particles to smaller sizes as temperature decreases as the Thompson scheme does, and snow MMDs exceed graupel MMDs at temperatures warmer than -20 °C and *w* less than 10 m s^{-1}. Morrison has larger snow MMDs than graupel MMDs, which is the reason that they contribute to reflectivity high biases in addition to graupel, consistent with findings in Varble et al. (2011).

The smallest mean graupel MMDs are produced in FSBM, which also produces the least GWC (cf. Figures 5.5k and 5.6k). This may be related to smaller raindrops at temperatures warmer than -4 °C and smaller cloud water bulk mass at temperatures below -8 °C, which reach sizes more representative of drizzle than suspended cloud droplets (Figure 5.6l). For decreasing temperatures in the FSBM scheme, lesser cloud water/drizzle contents can be expected to reduce riming and thus lead to lesser production of graupel. Moreover, the smaller raindrops lofted above the melting level that freeze will produce graupel particles that are smaller compared to the Morrison scheme, which lofts larger raindrops. The Thompson scheme does not conserve number concentration when raindrops freeze into graupel, but its exponential size distribution and inverse relationship between the size distribution intercept and GWC virtually assures large graupel diameters when GWC is significant.

The Thompson scheme produces the largest mean graupel MMDs, as shown in Figure 5.6c. At high *w* and warm temperatures, mean graupel MMDs commonly exceed 1 cm. These large graupel sizes are a result of the inverse relationship between graupel

mass and size, by which graupel N_0 is diagnostically decreased with an increase in graupel mass mixing ratio, forcing graupel to much larger sizes. The large amount of cloud water mass present at temperatures warmer than -30 °C (where a relatively small amount of SWC exists) is thus more easily converted to graupel mass, lowering N_0, and increasing mean graupel MMDs. However, recall that a small amount of GWC is present in Figure 5.5c. At larger sizes, the Thompson fall-speed relationship becomes hail-like, resulting in faster sedimentation and limited GWC at cold temperatures or low vertical velocities.

The Morrison scheme produces smaller mean graupel MMDs compared to Thompson, which suggests that prognostic N for graupel helps in reducing graupel's contribution to reflectivity biases. Smaller graupel sizes mean slower terminal fall speeds. The fall speed relationship with diameter used in the Morrison scheme, $v_f = 19.3D^{0.37}$, produces slower fall speeds than the Thompson relationship, $v_f = 442D^{0.89}$, for large graupel sizes. For a 4 mm diameter graupel particle in the Morrison scheme (roughly the largest mean graupel MMD in Figure 5.6g), the fall speed is ~ 2.5 m s^{-1}. However, a graupel particle of the same size in the Thompson scheme falls at 3.25 m s^{-1}, while a 1-cm diameter graupel particle in the Thompson scheme (at large w and warm T in Figure 5.6c) has a terminal fall speed of ~ 7.5 m s^{-1}. These differences result in more GWC being lofted to cold temperatures in the Morrison scheme, as shown in Figure 5.5g. Large GWC in the Morrison scheme therefore allow mean graupel MMDs to contribute most to the combined hydrometeor MMD in Figure 5.6e, despite snow being the largest precipitating ice species. The Thompson and FSBM combined hydrometeor MMD-TWC relationships are more evenly distributed between snow and graupel contributions

compared to Morrison, where snow governs at colder temperatures and weaker *w* and graupel governs at warmer temperatures and stronger *w*.

Relationships between TWC, T, and MMD are shown in Figure 5.7, which shows joint histograms of temperature and species bulk mass and color-filled with each species' mean MMD. Vertical velocities greater than or equal to 1 m s^{-1} remain as constraints for the grid points in MMD-T-TWC plots. Figures 5.7a, 5.7e, and 5.7i show that all schemes produce increasing MMDs with increasing temperature and TWC. This relationship also exists independently for graupel, snow, and liquid for every scheme. Bulk schemes loft supercooled cloud water droplets (MMD < 50 μm) to the homogeneous freezing level for TWCs ≤ 1 g m^{-3}, whereas the FSBM scheme only lofts LWCs up to 0.5 g m^{-3} to this region. For large LWCs, FSBM mean liquid MMDs are considerably smaller than the bulk schemes. This suggests that even for large LWCs, formation of smaller graupel sizes (from smaller raindrops) in FSBM occurs more readily compared to bulk schemes. However, mean snow MMDs reach values up to 1 cm at warm temperatures and SWC > 2.5 g m^{-3}.

The Thompson scheme produces graupel MMDs exceeding 0.5 cm for GWCs as low as 1 g m^{-3}, suggesting that only small amounts of GWC are needed to bias reflectivity high. Even for GWCs as low as 0.25 g m^{-3}, the Thompson scheme produces graupel MMDs of 2 mm at temperatures warmer than -12 °C. At TWCs > 2 g m^{-3} in the Morrison scheme, graupel largely controls the combined hydrometeor MMD, whereas snow contributes much more at TWC < 2 g m^{-3}.

Figures 5.5-5.7 show that the partitioning of hydrometeor bulk mass is different for each scheme and is a strong function of how parameterized fall speed relationships

sediment each hydrometeor species. The distribution of sizes for a given species bulk mass relies on the number of prognostic PSD moments, the mass-size relationship, and how gamma parameters are varied diagnostically. In the following section, we explore how combined hydrometeor MMDs and TWC compare to observations for a given *w* and temperature.

5.2.2 Differences between simulations and observations

Figure 5.8 shows observational joint histograms similar to the simulated ones in Figures 5.5-5.7. Figure 5.8a shows average TWC as a function of temperature and *w*, and average MMD as a function of *w*-T and TWC-T are shown in Figures 5.8b and 5.8c, respectively. Observed mean TWCs in Figure 5.8a range from 1 to 3 g m^{-3} and generally increase with increasing *w*. No clear TWC-*w* relationships are present as a function of temperature, though this may be related to observational sampling biases, particularly at warm temperatures. In Figure 5.8b, a temperature dependency arises for average MMD as function of *w*. Observed mean MMDs range from 200-300 μm at temperatures colder than -30°C to sizes approaching 1 mm at higher *w* and warmer temperatures. Larger mean MMDs at temperatures between -24 °C and -28 °C and between -32 °C and -36 °C for all *w* and TWC values in Figures 5.8b and 5.8c result from observations of a single long-lived tropical low sampled during 2 flights on 2-3 February. These larger MMDs may be associated with the sustained upward motion near the center of the system's cyclonic circulation, which may allow the ice particles to grow to larger sizes before sedimenting to lower levels. Most observed *w*-T bins at temperatures colder than -20 °C show decreasing mean MMD with increasing *w*. The FSBM scheme is the only scheme

that is able to reproduce this feature (Figure 5.6i), while both bulk schemes show increasing MMD with increasing *w* for a given temperature (Figures 5.6a and 5.6e). Figure 5.8c shows that observed mean MMDs are not highly correlated with TWC at warm temperatures, though this also could be associated with biased sampling. At colder temperatures, observed mean MMDs generally decrease with increasing TWC for a given temperature. The exception is the 2-3 February flights into a strongly cyclonic tropical low that exhibit increasing mean MMDs with increasing TWC. All simulated MMD-T-TWC relationships in Figures 5.7a, 5.7e, and 5.7i fail to exhibit this, instead exhibiting increasing MMDs with increasing TWC for a given temperature.

Figures 5.9a-c show absolute differences and Figures 5.9d-f shows percentage differences between simulated and observed mean TWC as a function of *w* and temperature. Average TWCs in *w*-T bins where observations are present are subtracted from average TWCs for Thompson (Figures 5.9a and 5.9d), Morrison (Figures 5.9b and 5.9e), and FSBM (Figures 5.9c and 5.9f). At temperatures colder than -30 °C and *w* below 8 m s^{-1}, all microphysics schemes produce lesser mean TWCs than observed, but at higher *w* values, simulations produce greater mean TWCs than observed. At temperatures warmer than -30 °C, all simulations generally produce greater TWCs than observed, which could partly be a result of observational sampling bias. The Thompson scheme reproduces the observed T-*w*-TWC relationship with the greatest accuracy, where most average TWC values are within 1 g m^{-3} of observations for a given *w* and T. The FSBM scheme shows slightly larger differences with observed mean TWCs, while the Morrison scheme shows the greatest differences with much larger TWCs than observed across a range of *w*-T bins. The greater Morrison TWCs are largely attributable to the excessive

GWCs shown in Figure 5.5g. The largest percentage differences occur at $w < 5$ m s^{-1}. For weak to moderate w values, all schemes produce greater TWCs by more than 50% at temperatures warmer than -20 °C and lesser relative TWC by up to 100% at temperatures between -30 °C and -50 °C. Since snow is the primary contributor to TWC at $w < 5$ m s^{-1} and temperatures between -30 °C and -50 °C for all schemes, Figure 5.9 suggests that simulations do not produce enough snow.

Absolute and relative differences between simulated and observed mean MMDs as a function of temperature and w are shown in Figure 5.10. Thompson mean MMDs at temperatures below -30 °C and $w < 10$ m s^{-1} are slightly smaller than observed, but generally lie within 0.5 mm of observed MMDs. These small MMDs are associated with the Thompson snow parameterization forcing snow particles to relatively small sizes at colder temperatures. The FSBM scheme produces larger than observed mean MMDs in this w-T region, and while generally remaining within 0.5 mm of observations, relative differences approaching 100% exist for several w-T bins. For temperatures warmer than -20 °C and $w > 10$ m s^{-1}, all schemes exhibit relative differences of up to 100% or greater. The Morrison mean MMDs are larger than observed across almost every w-T bin with relative differences commonly exceeding 100%.

Figure 5.11 is similar to Figure 5.10, but the abscissa is TWC rather than w. Similar trends exist in MMD-T-TWC space as in MMD-T-w space. The Thompson scheme has smaller than observed mean MMDs at temperatures colder than -30 °C and TWCs up to 3 g m^{-3}, with more pronounced relative differences for TWCs < 1 g m^{-3} and temperatures colder than -40 °C. However, at TWCs exceeding 3 g m^{-3} and temperatures from -24 °C to -36 °C, the Thompson scheme has larger than observed mean MMDs by

more than 2 mm. The FSBM scheme produced larger than observed mean MMDs for most TWC bins at temperatures colder than -10°C, and the Morrison scheme produces much larger mean MMDs than observed across the majority of TWC-T bins. Positive relative differences (mean simulated MMDs > mean observed MMDs) increase as temperature and TWC increases, commonly exceeding 100% for all schemes.

Figures 5.10-5.11 show that all simulations produce larger than observed mean MMDs across a wide range of temperatures, *w*, and TWC, while Figure 5.9 shows that these larger than observed MMDs are not entirely associated with larger than observed TWCs. Differences with observed mean MMDs are much more prevalent in the Morrison scheme than in the Thompson and FSBM schemes. All schemes produce the largest differences with observed mean MMD values at higher *w* and TWC, although observations of particle size may be biased low at higher *w* and TWC because of avoidance of the most intense convective cores that likely contain more graupel than the sampled cores. As shown in Section 5.2.1, different species for each scheme control the overall TWC and MMD values.

5.3 MMD-W-TWC relationships in specific temperature ranges

To further investigate differences between simulations and observations, relationships between TWC, *w*, and MMD are explored for limited temperature ranges, avoiding the need for averaging TWC and MMD in variable-filled joint histograms. Two regions are selected (-32 °C to -40 °C and -8 °C to -16 °C) because of the number of observations available in these two regimes, as shown by black contours in Figure 5.8.

5.3.1 -32 °C to -40 °C

Figures 5.12a-c show average TWC, SWC, and GWC as a function of *w*, respectively, for temperatures between -32 °C and -40 °C, and Figures 5.12d-f show average *w* as a function of TWC, SWC, and GWC, respectively, for the same temperature range. Note that the ordinate ranges vary for each species. LWC is excluded because of the small amount of LWC in this temperature range. The FSBM scheme contains a negligible amount of LWC, while Thompson has the largest liquid contribution to TWC, but it generally remains below 0.75 g m^{-3} (not shown). Figure 5.12a shows that the Thompson scheme reasonably captures the observed TWC-*w* relationship in this temperature range, where TWC increases with increasing *w* and asymptotes toward 2.5 g m^{-3} at high *w*. For *w* below 10 m s^{-1}, observed TWC values for a given *w* bin are typically around 0.25 g m^{-3} higher in observations compared to Thompson. The Morrison scheme fails to capture the observed TWC-*w* profile as adequately as the Thompson scheme, producing TWC up to 1.5 g m^{-3} greater than observations for *w* greater than 6 m s^{-1}. The FSBM scheme performs closer to Thompson, producing lower TWC than observed for a given *w* below 6 m s^{-1}, but diverges from observations more than Thompson at higher *w* where TWC values are higher than observed. For TWC less than 2 g m^{-3} where most observations are available, all schemes generally reproduce an observed increase in *w* as a function of TWC (Figure 5.12d). Although few observations are available for TWC exceeding 3 g m^{-3}, all simulations show that larger *w* values are correlated with larger TWC values, but that each scheme significantly diverges from one another.

Figure 5.12b shows that SWC generally increases with increasing *w* in the Thompson and FSBM schemes, while decreasing slightly as a function of *w* at values

greater than 10 m s^{-1}. The Morrison scheme produces decreasing SWC with increasing *w* for values greater than 5 m s^{-1}. Vertical velocity generally increases as SWC increases for all schemes (Figure 5.12e), although only a weak SWC-*w* relationship is present in all schemes, consistent with Figures 5.5b, 5.5f, and 5.5j. GWC increases with increasing *w* in all schemes (Figure 5.12c), but to varying degrees. Thompson and FSBM have the least GWC in this temperature range (see Figure 5.5), while Morrison has the most, and therefore, the GWC contribution controls the Morrison TWC-*w* relationship in Figure 5.12a. Conversely, SWC dominates the TWC-*w* relationships for the Thompson and FSBM schemes, especially for weaker *w*. Vertical velocity as a function of GWC (Figure 5.12f) shows that *w* increases with increasing GWC for all schemes, but significant variability exists between schemes.

Figure 5.13 shows percentile mass diameters (10% MD, MMD, and 90% MD) as a function of *w* (Figures 5.13a-c) and TWC (Figures 5.13d-f). The Morrison and FSBM schemes fail to reproduce observed percentile mass diameters across all ranges of *w* and TWC, with differences as large as 3 mm for 90% MDs. The Thompson scheme produces smaller than observed 10% MDs in this temperature range, which is largely due to the prominent small, dense particle mode of the parameterized snow size distribution. MMDs and 90% MDs produced by the Thompson scheme diverge from observations significantly at high *w* and TWC values, a result of very large graupel sizes despite limited GWC in this temperature range. Some of this difference may be a result of biased observational sampling, but likely not all of it because of the high biases in Thompson simulated reflectivity. At *w* below 10 m s^{-1} and TWC below 2.5 g m^{-3}, Thompson and observed MMD and 90% MD values agree remarkably well. The Morrison scheme

generally produces the largest 10% MDs and MMDs, while the 90% MDs in FSBM are larger than in the other schemes at $w < 10$ m s^{-1} and TWC < 2.5 g m^{-3}, much larger than observed.

Clearly, large differences between the schemes and observations exist in the contribution of various hydrometeor sizes to total condensate mass, and variability becomes more significant at higher *w* and TWC values. Figure 5.12a shows that the FSBM and Morrison schemes loft greater condensate mass compared to observations for $w > 10$ m s^{-1}, but contain too little at smaller *w* values. The Thompson scheme performs better at higher *w* values, perhaps because of faster graupel sedimentation in the Thompson scheme than Morrison and FSBM schemes, caused by its inverse diagnostic relationship between graupel size and predicted mass coupled with its large fall speeds for larger graupel sizes. However, Thompson still appears to produce too many large particles at higher *w* and TWC, while Morrison and FSBM schemes produce larger particles than observed for all *w* and TWC values. These results show that high biased reflectivities aloft in simulations are not only a result of convective updrafts that are too strong, but also that biases are strongly tied to particle sizes that are too large.

5.3.2 -8 °C to -16 °C

Figure 5.14 shows the same information as Figure 5.12, but for a temperature range between -8 °C and -16 °C with LWC contributions to TWC included. Observations in Figures 5.14a and 5.14e are plotted as individual data points because of few measurements in this temperature region during the Darwin campaign. All simulations and observations produce increasing TWC with increasing *w* relationships as was found

at colder temperatures. The Morrison scheme produces the highest TWC for a given *w*, while the FSBM scheme produces slightly smaller TWC, but more than Thompson. Limited observations in this temperature range prevent conclusions on which schemes produce TWC-*w* relationships closest to observed.

For the Thompson and Morrison schemes, SWC decreases for increasing *w* (Figure 5.14b). This is an important relationship, and suggests that moderate to strong updraft cores in the mixed-phase region of convective updrafts fail to produce significant SWCs, despite observations in cores with *w* values of 5-10 m s^{-1} in this temperature range exhibiting primarily vapor-grown ice (L16). For the FSBM scheme, SWC generally increases with increasing *w* for *w* below 12 m s^{-1}, but a decreasing SWC-*w* relationship for larger *w*. This is consistent with the largest amount of SWC production by FSBM at higher *w* shown in Figure 5.5j. All schemes also show that GWC increases with increasing *w* (Figure 5.14c), where Morrison produces the most GWC in this temperature range for a given *w*. Similarly to the colder temperature range, *w* as a function of SWC shows a very weak relationship (Figure 5.14f), whereas *w* as a function of GWC shows a stronger positive relationship (Figure 5.14g).

The Thompson and Morrison schemes produce increasing LWC with increasing *w* (Figure 5.14d). Similar LWC-*w* and GWC-*w* relationships suggest that LWC in the bulk schemes is connected to GWC through freezing and riming processes. The FSBM scheme has the smallest LWC across all *w* in this temperature range (see Figure 5.5), but much larger amounts of LWC (> 4 g m^{-3}) at temperatures between 0 °C and -4 °C compared to the bulk schemes. The large amount of LWC between 0 °C and -4 °C is primarily raindrops (Figure 5.6l) formed by collision-coalescence that is likely faster than

that in the bulk schemes because of aerosol consumption. These raindrops are smaller than in the bulk schemes, and freeze quickly upon encountering ice particles and form graupel. In addition, the FSBM scheme allows supersaturation over liquid to exist, which may be related to the very small amount of LWC in this temperature region. The ability of supersaturation over liquid to persist limits condensation in the FSBM scheme, which differs from saturation adjustment in bulk schemes that condense all supersaturation over liquid while applying a constant cloud droplet number concentration.

Figure 5.15 is the same as Figure 5.13, but for updrafts in the -8 °C to -16 °C temperature range and observations are plotted as individual black diamonds. Much larger hydrometeor sizes are present at these warm temperatures than at the colder temperatures, and thus the ordinate range in Figure 5.15 is larger than in Figure 5.13 for MMDs and 90% MDs. Across all percentile mass diameters as a function of *w* or TWC, all schemes generally produce larger hydrometeor sizes than observed. The Thompson scheme reproduces the 10% MD observational profile reasonably well at weak-moderate *w* and TWC < 2 g m^{-3}. The Morrison and FSBM schemes capture the decreasing 10% MD with increasing *w* relationship, but Morrison performs considerably better with increasing *w*. The small 10% MDs for *w* > 5 m s^{-1} in the bulk schemes are produced by cloud droplets. In comparison with observations, this suggests that too many cloud droplets are produced in updrafts with *w* between 5 and 10 m s^{-1}. However, larger than observed 10% MDs in the FSBM scheme for all *w* may result from insufficient numbers of cloud droplets, possibly related to errors in aerosol representation, transport, and/or consumption. All schemes produce larger than observed MMDs and 90% MDs for most *w* and TWC where observations are present. The bulk schemes perform similarly, but

Thompson appears better able to capture observed 10% MDs as a function of TWC. For TWC < 2.5 g m^{-3} and w < 10 m s^{-1} where observations are present for this temperature region, Thompson TWC at these weaker vertical velocities is largely controlled by snow (Figure 5.5b), and so the 10% MD is likely closest to observations because of the smaller vapor-grown ice particles that result from Thompson's unique snow parameterization. FSBM recreates the observed MMD-w profile best across a range of w, but produces larger than observed 10% MDs, MMDs, and 90% MDs for a given TWC. Observed 90% MDs generally increase with increasing w, which the Thompson scheme is able to capture. The FSBM scheme produces the wrong slope, decreasing 90% MDs with increasing w. Figures 5.5 and 5.14 show that GWC increases and SWC decreases with increasing w while Figure 5.6 shows that snow sizes are larger than graupel sizes in the FSBM scheme. As w increases and graupel mass increases, the combined hydrometeor 90% MD shifts from being controlled by snow to graupel, decreasing the 90% MD in the FSBM scheme. The Morrison scheme also produces larger snow than graupel particles, but since the TWC-w relationship is largely controlled by GWC for all w, the combined hydrometeor 90% MD is largely controlled by graupel rather than snow. This results in a slightly increasing 90% MD with w for Morrison, asymptoting to ~ 5 mm for w > 7 m s^{-1}.

5.4 Sensitivity simulations

5.4.1 MMD-T-W-TWC relationships for different MCS cases

Figures 5.16a-c show 2.5-km altitude radar reflectivity cross-sections for the 2-3 February, 7 February, and 23 January cases, respectively, from WRF simulations using the Thompson scheme at a time representative of when each system was sampled for

analysis. Figures 5.16d-f show TWC 7-km altitude cross sections for the same time and cases. Clear differences in precipitation structure exist between these events. The 2 February long-lived tropical low simulation shown in Figure 5.16a produced widespread, intense deep convection with large TWC (> 4 g m^{-3}) oriented along spiral bands associated with the cyclonic circulation, whereas satellite, long range radar, and lightning measurements (not shown) show that the observed case produced equally deep, but weaker convection primarily in the center of the circulation (see Figure 3.1). The 7 February and 23 January events in Figures 5.16b-c, respectively, both produced squall lines at some point during their life cycle like observed. The 7 February case produces stronger updraft cores capable of lofting a larger amount of TWC compared to the 23 January event, also like observed (see Figure 3.1).

Clearly, the depth of intense updraft cores and amount of lofted TWC are different for each simulation. Figure 5.17 compares these events in the MMD-T-*w*-TWC phase space considered for the 18 February case. Average TWC as function of *w* and T is shown in panels (a-c), average MMD as a function of *w* and T in panels (d-f), and average MMD as a function of TWC and T in panels (g-i). Compared to the 18 February case (Figures 5.5a), the 7 February and 2 February cases produce slightly higher TWC for a given *w*-T bin, while the 23 January event produces the lowest TWC. MMDs for a given *w*-T bin are very similar for 18 February, 2 February, and 7 February (see Figure 5.6a). The 23 January case shifts MMDs to smaller sizes for a given *w*-T bin, but Figure 5.17i shows that MMDs for 23 January as a function of TWC and T are very similar to the other cases. This suggests that even though the 23 January case produced weaker updraft velocities that decreased the amount of lofted condensate, hydrometeor size

distributions do not change significantly as a function of TWC for a given temperature.

Figure 5.18 shows the same fields as Figure 5.16, but for the Morrison scheme instead of the Thompson scheme. For all simulated events, the Morrison scheme produces noticeably larger regions of high reflectivity than the Thompson scheme. The 2.5-km altitude reflectivity cross-sections show that regions exceeding 40 dBZ are much more prevalent in the Morrison scheme. Figures 5.18d-f show that larger amounts of TWC (both in quantity and spatial extent) exist above the melting level compared to Thompson. Morrison MMD-T-*w*-TWC relationships are shown in Figure 5.19 for each simulated event. As for the Thompson scheme and for the 18 February Morrison simulation, all events show that MMD and TWC increase with increasing temperature and *w*, and that MMDs increase as a function of increasing TWC and temperature. For the 23 January Morrison simulation, MMDs change more as function of TWC and T than in the Thompson simulation, which is likely a result of snow and graupel's double moment parameterization in the Morrison scheme, allowing for more flexibility in the range of sizes produced by the scheme. Despite significant differences in mesoscale precipitation structure for the events, the similarities between each event in MMD-T-*w*-TWC phase space for two different microphysics schemes suggest that a single event such as 18 February is adequate for robustly examining differences between various microphysics schemes and observations. It is possible that a bin microphysics scheme would be more variable than the bulk schemes, but examination of bin scheme variability between different simulated events is left for future studies due to their high computation costs.

5.4.2 Sensitivity of MMD-T-W-TWC relationships to model resolution

Investigation of the dependency of MMD-T-*w*-TWC relationships on horizontal resolution was performed for the Thompson scheme with a nested 333-m horizontal grid spacing domain. A 150-km by 150-km area inside the 333-m domain was used to sample convective updraft properties to exclude data points affected by model spin-up along the southern and western boundaries of the domain. Only grid points from the 1000-m grid spacing simulation that lie inside this 150-km by 150-km area are used for comparison with the 333-m simulation. Vertical levels are doubled from 91 to 182 and the simulation is run from 12Z on 18 February to 00Z on 19 February using boundary forcing from the 1000-m domain.

Figure 5.20 shows 7-km altitude reflectivity cross-sections for the 333-m simulation (Figures 5.20a-c) and the 1000-m simulation limited to the 333-m domain (Figures 5.20d-f) for 18Z (a, d) and 21Z (b, e) on the 18th and 00Z (c, f) on the 19th. The 333-m domain precipitation evolution is different in comparison with the 1000-m simulation. At 18Z, both simulations show two convergence zones—one just to the north of the Australian mainland and the other over the Tiwi Islands to the north. Both simulations eventually merge the two lines of convection as the southern squall moves north, but convection along the northern line is more extensive in the 333-m simulation through this six-hour period compared to the 1000-m simulation. The 1000-m simulation also produces much more extensive regions of stratiform precipitation and high reflectivity convective cores. Moreover, it is apparent that the higher resolution simulation produces more cellular convection and smaller updraft cores, and is therefore

more capable of resolving updraft dynamics and mixing processes.

Figure 5.21 shows joint histograms filled with relative differences between 333-m and 1000-m average species bulk mass for *w*-T bins (Figures 5.21a-d), average species MMD for *w*-T bins, (Figures 5.21e-h), and average species MMD for species bulk mass and T bins (Figures 5.21i-l). The top row shows combined hydrometeors (TWC), the second row shows vapor-grown ice species (SWC), the third row shows graupel (GWC), and the bottom row shows liquid (LWC). Figure 5.21a shows that the higher resolution simulation generally produces less TWC for a given *w* value. Discrepancies are enhanced at temperatures colder than -30 °C and $w < 5$ m s^{-1}. Decreases in both GWC and SWC in this *w*-T range contribute to the decrease in TWC. Combined hydrometeor mean MMDs for a given *w*-T bin (Figure 5.21e) are up to 50% smaller at temperatures warmer than -20°C and $w > 15$ m s^{-1}. This decrease in mean MMDs is largely attributable to a slight decrease in graupel MMDs combined with a more significant decrease in GWC in these *w*-T bins (Figure 5.21c). Less GWC at these warmer temperatures is likely a result of more efficient sedimentation of larger ice particles out of smaller updraft cores (Figure 5.20), where updrafts more closely resemble shedding thermals rather than deep convective plumes (Varble et al., 2014a). Additionally, larger raindrops sediment more easily out of updraft cores before reaching 0°C, and the raindrops that survive to sub-freezing temperatures and freeze to form graupel are somewhat smaller in the 333-m domain than the 1000-m domain. Figure 5.21l shows that liquid MMDs decrease across most LWC-T bins. The bins where liquid MMDs increase are the result of larger cloud water droplets, while rain MMDs for a given RWC-T bin are smaller across almost every bin (not shown). Therefore, smaller raindrops lofted above the freezing level are

consistent with a slight decrease in graupel MMDs just above the freezing level for a given *w*-T bin (Figure 5.21f). Overall, higher horizontal resolution aids in decreasing the size difference in the Thompson scheme, particularly at warm temperatures where the bias is most prevalent (see Figure 5.10a), but finer resolution alone is not enough to shift hydrometeor sizes to anywhere near the observed sizes.

5.4.3 Sensitivity of MMD-T-W-TWC relationships to explicit cloud droplet nucleation

A sensitivity run was also performed using the Thompson "aerosol-aware" (AA) scheme (Thompson and Eidhammer, 2014) that employs explicit cloud droplet nucleation by CCN, making cloud water a double moment species in addition to cloud ice. Initial concentrations of CCN and ice nucleating particles (IN) at the surface are 100 cm^{-3} and 1.5 cm^{-3}, respectively, and decay exponentially to 50 cm^{-3} and 0.5 cm^{-3}, respectively, in the free troposphere. Figure 5.22 shows relative difference joint histograms between the AA scheme and the non-AA scheme across MMD-T-*w*-TWC phase space. The color-filled variable and axis values are the same as in Figure 5.21, but the relative difference color bar spans a larger range of -100% to 100%.

In comparison to the non-AA scheme, the AA scheme produces lesser SWC for most *w*-T bins, with greater SWC at temperatures warmer than -20°C and $w > 10$ m s^{-1}. GWC increases in the AA scheme for many *w*-T bins, but decreases at warmer temperatures and weaker *w*. Not surprisingly, the largest relative changes in bulk mass occur for LWC, which decreases by more than 100% for temperatures between -30 °C and -40 °C and to a lesser degree for warmer temperatures (Figure 5.22d). However,

LWC contributes little to TWC, and therefore, changes in TWC (Figure 5.22a) at sub-freezing temperatures are largely due to changes in SWC and GWC.

The largest relative differences in average MMD for a given *w*-T or TWC-T bin also occur for liquid. Relative decreases in liquid MMDs for LWC > 2 g m^{-3} (Figure 5.22l) are largely controlled by raindrops, while relative increases in liquid MMDs for LWC < 2 g m-3 are controlled by cloud droplets (not shown). For *w*-T bins (Figure 5.22h), relative increases in liquid MMDs are also due to larger cloud droplet MMDs (which become more representative of drizzle drops) while relative decreases result from smaller raindrop MMDs. Smaller raindrops produced in the AA scheme are more easily lofted to colder temperatures, allowing graupel mass to increase just above the melting level through the freezing of raindrops. Recall that smaller raindrops were also lofted above 0°C by the FSBM scheme, suggesting that explicitly representing CCN activation may be responsible for smaller raindrops and graupel particles at temperatures in the mixed-phase region. Despite a decrease in graupel MMDs for many *w*-T bins and most GWC-T bins, mean graupel MMDs increase at temperatures colder than -40°C for all *w*. This increase in graupel MMDs in conjunction with an increase in GWC at these colder temperatures (due to easier lofting of smaller graupel from below with slower terminal velocities; see Figure 5.22c) control the large relative differences in combined hydrometeor MMDs for higher *w* (Figure 5.22e) and higher TWC (Figure 5.22i). Therefore, although vapor-grown ice, graupel, and rain MMDs typically decrease for a given *w* or TWC at temperatures warmer than -40°C, combined MMDs increase by up to 100% at colder temperatures when employing explicit activation of CCN. Regardless, these changes are minor compared to the large differences between different schemes and

with observed particle sizes, which remain significantly smaller than those in the AA scheme for a given *w* or TWC.

5.5 Definitive hydrometeor size biases

Results from Section 5.3 (Figures 5.13 and 5.15) suggest that high biases in simulated radar reflectivity are connected to too much bulk mass in large particle sizes as opposed to simply exaggerated vertical velocities lofting too much mass condensate. However, proving that simulations have a hydrometeor size bias is difficult because of biased observational sampling that avoids the highest reflectivity convective cores. There is confidence that sampling of these cores would not bring observed and simulated mass size distributions together for a given *w* or TWC since observed maximum reflectivities aloft are significantly less than simulated, as shown in Figures 5.2-5.4. Additionally, there are properties that can be compared that are not impacted by observational sampling biases, including the minimum 90% MD as a function of *w* and TWC. Figures 5.23 and 5.24 show minimum 90% MD relative difference joint histograms for temperature versus TWC and *w*, respectively. These plots are created by computing the minimum observed and simulated 90% MDs for each TWC-T and *w*-T bin, and subtracting observations from each simulation, where simulations in (a-c) are Thompson, Morrison, and FSBM, respectively. It is important to note that simulations on average have a factor of 10^3 more samples than observations, and therefore, bins that have larger simulated minimum 90% MDs than observed can be confidently called a bias toward too much mass in large particles. Bins where simulated minimum 90% MDs are smaller than observed are inconclusive because of the difference in sample size. Figure 5.23 shows that for TWC >

1.5-2 g m^{-3} across temperatures colder than -25 °C, most simulated minimum 90% MD values are greater than observed values. This is particularly prevalent for the Morrison scheme, where the majority of simulated minimum 90% MDs for TWCs > 1 g m^{-3} at most temperatures are high biased. The Thompson scheme's high bias exists for TWC > 1.5 g m^{-3} and temperatures between -25 °C and -40 °C, where excessive graupel sizes prevent the smallest 90% MDs from reaching observed values. The FSBM scheme performs similarly to the Thompson scheme with high biased minimum 90% MDs at temperatures colder than -25 °C for TWCs greater than 0.5 g m^{-3}. Even between temperatures of -10°C and -20°C at significant TWCs, there are at least a few bins where all schemes exhibit high biases. At temperatures > -10 °C, observed samples are too small to make any conclusive statements.

Figure 5.24 shows that minimum 90% MD values for a given *w*-T bin are also biased high at w > 10 m s^{-1} and temperatures colder than -30 °C. The Thompson and FSBM schemes perform better than Morrison for most *w*-T bins, and notably, less bins exhibit high biases than TWC-T bins, which perhaps suggests that simulations struggle more to produce observed mass size distributions for a given significant TWC than a given significant upward vertical velocity.

Figures 5.23 and 5.24 show that despite simulated sample sizes being many orders of magnitude larger than observations for any TWC-T-*w* bin, every microphysics scheme fails to produce a single minimum 90% MD value as small as observed at TWCs greater than 1.5 g m^{-3} or w greater than 10 m s^{-1} and temperatures colder than -30 °C. Recall that Figures 5.10 and 5.11 show that average MMDs are typically larger than observed in these TWC-T-*w* bins as well. These size biases for given w and TWC values show that

parameterized hydrometeor properties and/or microphysical processes are key contributors to high biased hydrometeor sizes, which are not simply a result of exaggerated updraft vertical velocities and condensate mass. It appears that the Thompson scheme's temperature-dependent snow PSD and mass-diameter relationship based on Field et al. (2005) aids in reducing the hydrometeor size bias relative to the Morrison scheme, despite Morrison's ability to produce a larger range of sizes as a 2M scheme with prognostic graupel and snow number concentrations. However, even bin representation of the PSD by the FSBM scheme produces high biased hydrometeor sizes. This places credence in the likely role of parameterized microphysical process errors in producing hydrometeor size biases in addition to parameterized hydrometeor PSDs and mass-size relationships.

5.6 Connecting hydrometeor size biases to radar reflectivity biases

Evaluating biases in equivalent Rayleigh reflectivity factor size distributions (ZSDs) may be analyzed to explore how errors in PSDs and MSDs translate to reflectivity biases. One caveat to interpreting differences between simulated and observed MSDs and ZSDs is that the observed MSDs are characterized by a single retrieved mass-diameter relationship, which may not work well in all situations, for example when there are relatively high density small and large particles, but relatively low density medium-sized particles. However, retrieval errors are likely reduced by computing composite distributions and are not likely to account for an order of magnitude difference between observed and simulated masses or reflectivities at a given particle diameter, because it would require greater than a 300% particle density error for the ZSD and 1000% particle

density error for the MSD.

Figure 5.25 shows observed and simulated composite PSDs, MSDs, and ZSDs for temperatures between -12 °C and -20 °C (Figures 5.25a-c) and between -32 °C and -40 °C (Figures 5.26d-f). All observed and simulated data points where TWC is between 2 and 2.5 g m^{-3} are included so that each composite PSD, MSD, and ZSD has approximately the same bulk mass. No *w* constraint is used in an effort to increase the sample size of observed distributions. However, implementing $w > 1$ m s^{-1} or $w > 5$ m s^{-1} requirements generally increases the mass contained in larger particle sizes (not shown). Discrepancies exist in observed and simulated composite PSDs (Figures 5.25a, d), though all schemes better reproduce observed PSDs in the colder temperature range. At warmer temperatures, all schemes underestimate the number of particles at diameters between 0.1 and 0.7 mm by an order of magnitude or more, but overestimate the number of particles with diameters greater than 1.5 mm by about an order of magnitude. Each microphysics scheme also agrees better with one another than with observations in this temperature range. At colder temperatures, the Thompson scheme captures the PSD quite well, while the FSBM scheme has more particles than observed for diameters greater than 1 mm and less particles than observed for diameters less than 0.5 mm. The Morrison scheme fails to capture the slope of the observed PSD at cold temperatures, producing less particles than observed at diameters less than 1 mm and greater than 6 mm, but more particles than observed in between.

Figures 5.25b and 5.25e show composite MSDs, which are computed by multiplying the mass-diameter relationship by the PSD of each species and adding each species together for bulk schemes and by multiplying the mass of particles in each size

bin by the number in that bin for observations and the FSBM scheme. Symbols plotted on the MSDs represent the 10% MD (squares), MMD (asterisks), and 90% MD (triangles). Observations show a prominent MSD mode at around 300 μm at both temperature ranges. At warmer temperatures, all simulations fail to capture the amplitude and location of this mode. Both bulk schemes shift the MSD mode to around 1 mm, while the FSBM scheme is slightly smaller but still larger than observed. All schemes distribute more mass at particle sizes larger than 1 mm in comparison with observations. Simulated MMDs are similar to observed 90% MDs, whereas simulated 90% MDs are several millimeters or more larger than observed. Remarkably, 90% of the more than 2 g m^{-3} condensate mass observed is typically contained in particles with diameters smaller than 1.5 mm at temperatures between -12°C and -20°C. While simulated MSDs at warmer temperatures perform somewhat similarly to one another, the same is not true at colder temperatures, where simulated results vary much more. The Thompson scheme is able to reproduce the MSD mode at 300 μm fairly well and compares favorably with observations up to 1500 μm, but then contains significantly more mass than observed at larger diameters. The FSBM scheme reproduces the shape of the observed MSD, but also distributes too much mass at larger diameters and has the most mass at particle diameters of 500 μm rather than 300 μm. The Morrison scheme puts the most mass in particles between 1 and 2 mm in diameter and distributes significantly more mass to particles between 1.5 and 5 mm than other schemes, but much less mass at particles larger than 5 mm. Ninety percent of the more than 2 g m^{-3} condensate mass observed is typically contained in particles with diameters smaller than 1 mm at temperature between -32°C and -40°C, and no simulation produces a MSD that narrow.

Figures 5.25c and 5.25f show how equivalent Rayleigh radar reflectivity factor is distributed among particle size. Composite observed ZSDs show a primary mode around 1500 μm at warmer temperatures (Figure 5.25c) and around 500 μm at colder temperatures (Figure 5.25f). In both temperature ranges, observed ZSD values decrease to a local minimum around 3-4 mm, but a secondary mode exists at larger diameters. Both bulk schemes fail to capture the local minimum in ZSD around 3-4 mm and produce larger reflectivities than retrieved from observations. The FSBM scheme reasonably recreates the observed ZSD at warmer temperatures, but at colder temperatures produces too much reflectivity for diameters between 1 and 6 mm despite being the only scheme that captures the local ZSD minimum around 3-4 mm. Both bulk schemes produce reflectivities that are an order of magnitude greater than observed at colder temperatures for diameters between 2 and 5 mm. The Thompson scheme recreates the observed ZSD at cold temperatures up to 1500 μm similarly to the MSD at these temperatures, but produces much higher reflectivities at larger diameters despite only having 10% of condensate mass contained in these diameters, leveling off at 1 mm^6 m^{-3} μm^{-1} for diameters ranging from 4-10 mm.

Figure 5.26 is the same as Figure 5.25, but for lesser TWC values between 0.5 and 1 g m^{-3}. At warmer temperatures, all simulations tend to better reproduce observations for lower TWC than higher TWC (cf. Figures 5.25a and 5.26a). At colder temperatures, the FSBM scheme shifts closer to the observed distribution than for greater TWCs, although it underestimates the number of particles at smaller diameters. At cold temperatures, the Thompson scheme struggles in capturing the observed PSD for TWC < 1 g m^{-3} much more than it did for TWC > 2 g m^{-3}. However, the Thompson composite PSD and MSD

at warm temperatures generally resembles the observed distributions, despite the missing mass peak at 300 μm. The ZSDs at warm temperatures show that for TWC < 1 g m^{-3}, all simulations still produce high biased equivalent reflectivity factors by up to an order of magnitude at diameters greater than 4 mm such that all simulations generally exceed one standard deviation of observed values at a given diameter. At colder temperatures, similar trends to those seen at higher TWCs are shown, though the Thompson scheme performs better at smaller TWCs. Again, FSBM is the only scheme able to generally recreate the observed ZSD shape. These ZSDs show that even though the simulations distribute a small fraction of mass at larger diameters, that small fraction of mass can bias radar reflectivity if it is greater than observed at those diameters.

5.7 Context from Cayenne observations

Figure 5.27 shows MMD-T-*w*-TWC relationships similar to those in Figure 5.8, but for the Cayenne phase of the HAIC-HIWC campaign. In addition to the Falcon 20 aircraft, the Environment Canada Convair 580 aircraft was equipped with in situ optical array and TWC probes and flew through convective systems around the -10 °C level, providing many more samples than were collected during the Darwin campaign at warm temperatures. The Convair datasets are still being quality controlled, but the Falcon datasets have been made available for analysis. Convective updrafts in Cayenne were generally weaker compared to Darwin, with the majority of samples in Figures 5.27a-b below 10 m s^{-1}. This is consistent with lower reflectivities aloft and much less lightning in Cayenne systems than Darwin systems. The great advantage of this fact is that observational sampling is much less biased in Cayenne because fewer convective cores

needed to be avoided, especially in the case of larger systems over the ocean.

Cayenne observed mean TWC for a given *w*-T bin is generally higher than Darwin values, reaching average values greater than 3 g m^{-3} for several bins at temperatures warmer than -20 °C. Cayenne data supports the observed trend of increasing TWC with increasing temperature that was seen in the Darwin observations. Despite slightly larger TWC for a given *w*-T bin, MMDs are very similar between Cayenne and Darwin, where MMDs increase with increasing temperature, and temperatures colder than -30 °C generally exhibit MMDs ≤ 0.6 mm. At temperatures warmer than -30 °C, both campaigns show that average MMDs typically remain below 1 mm. Figure 5.27c shows clearly the larger sample size in the Cayenne observations at warmer temperatures, and that many more samples exist at higher TWC (e.g., > 3 g m^{-3}) for a wide range of temperatures. As for Darwin, MMDs in the Cayenne dataset are not highly correlated with TWC at warm temperatures. Recall that Darwin observations showed a slight trend of decreasing MMD with increasing TWC at colder temperatures. This is less obvious in Cayenne observations. In general, MMDs for a given *w*-T or TWC-T bin are not significantly different from Darwin observations. While this places confidence in the generality of Darwin observations and in the ability to combine the two datasets for more statistically robust sample sizes, incorporation of Convair datasets, more in depth comparison of Darwin and Cayenne datasets, and simulations of Cayenne events are needed to test and extend the results presented here.

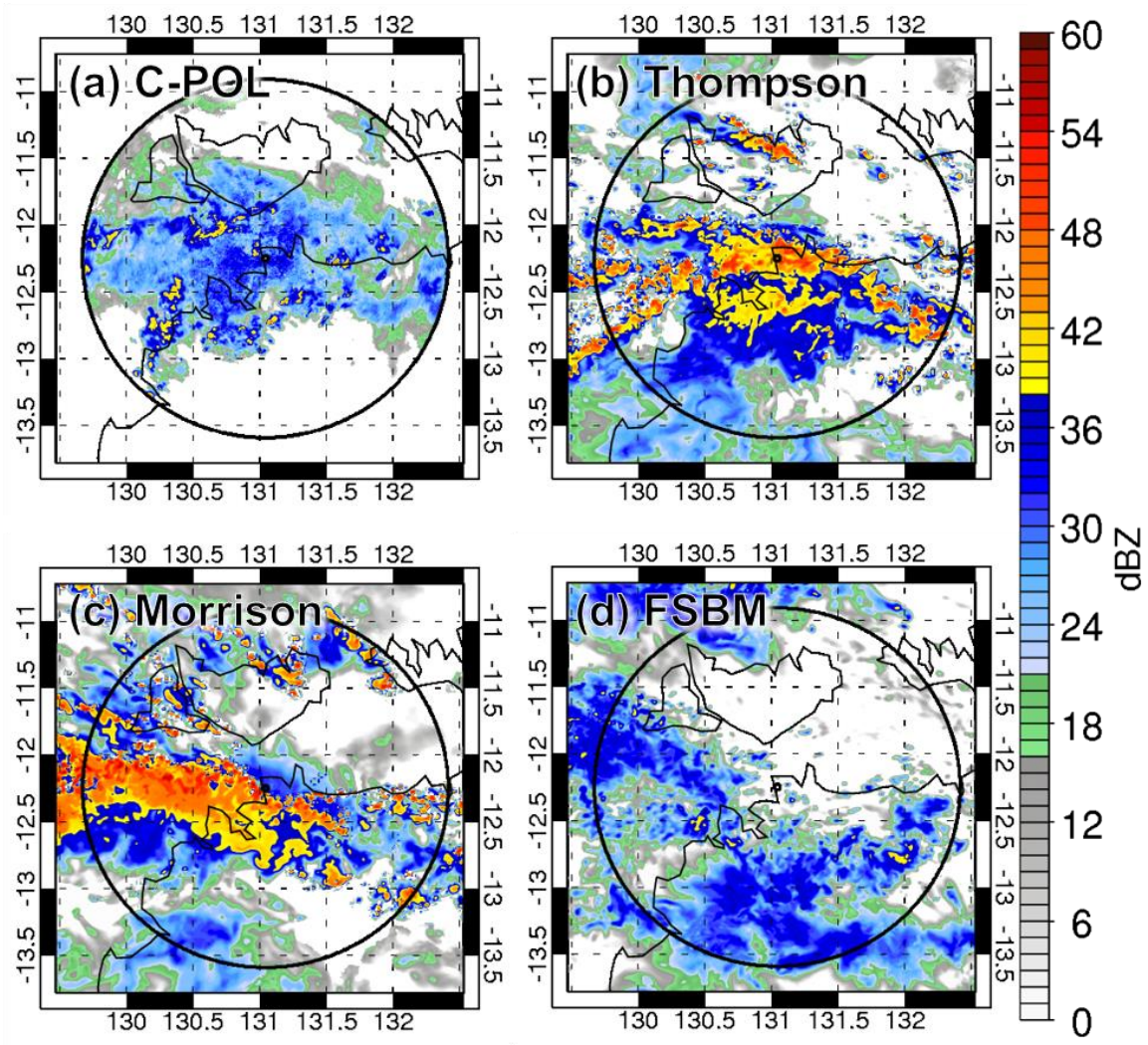

Figure 5.1. Representative 2.5-km horizontal radar reflectivity cross-sections on 18 February 2014 at 18Z for (a) observed C-POL, (b) Thompson, (c) Morrison, and (d) FSBM schemes. The circle indicates the 150-km range ring of the C-POL radar.

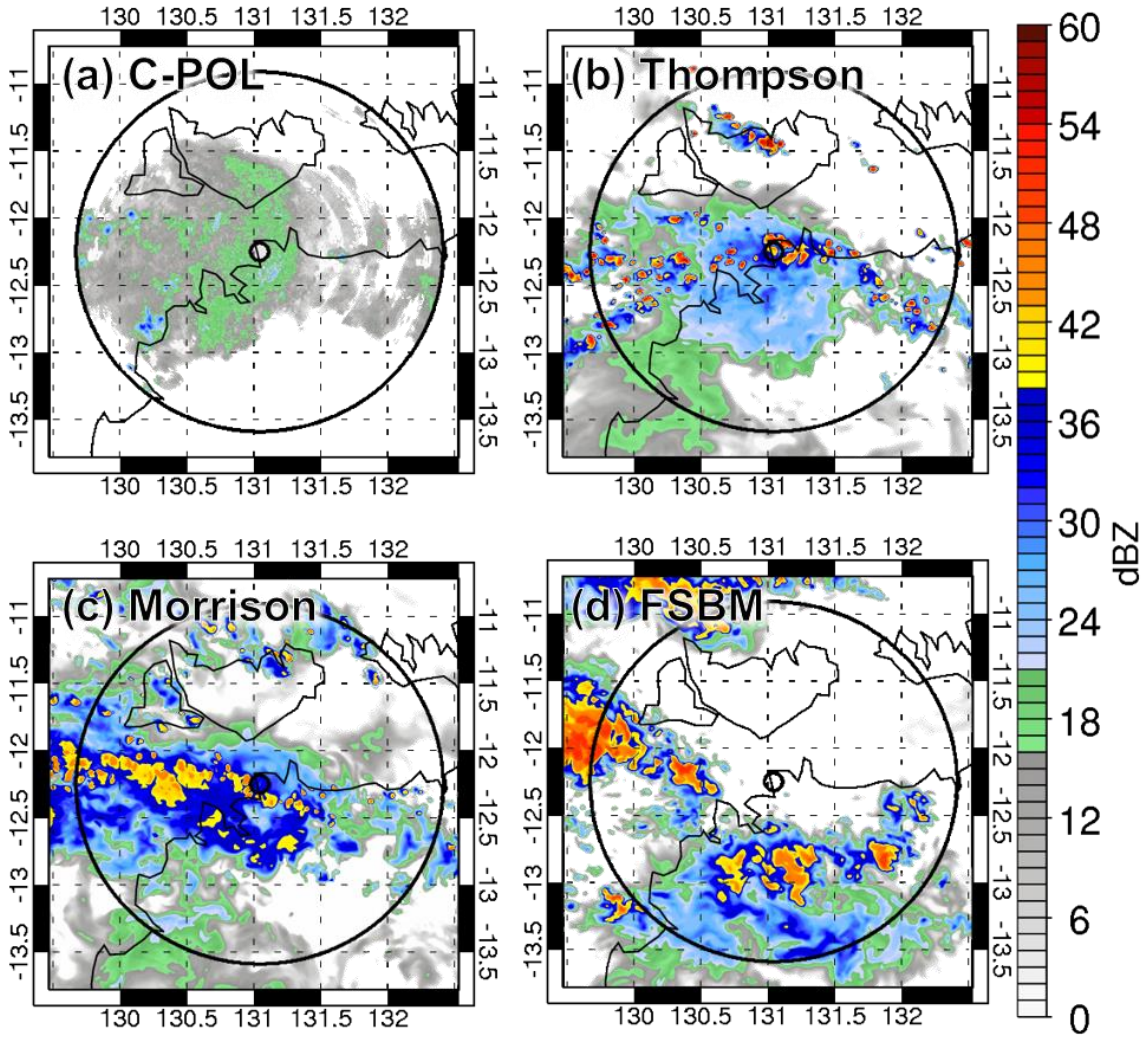

Figure 5.2. As in Figure 5.1 for 7-km altitude.

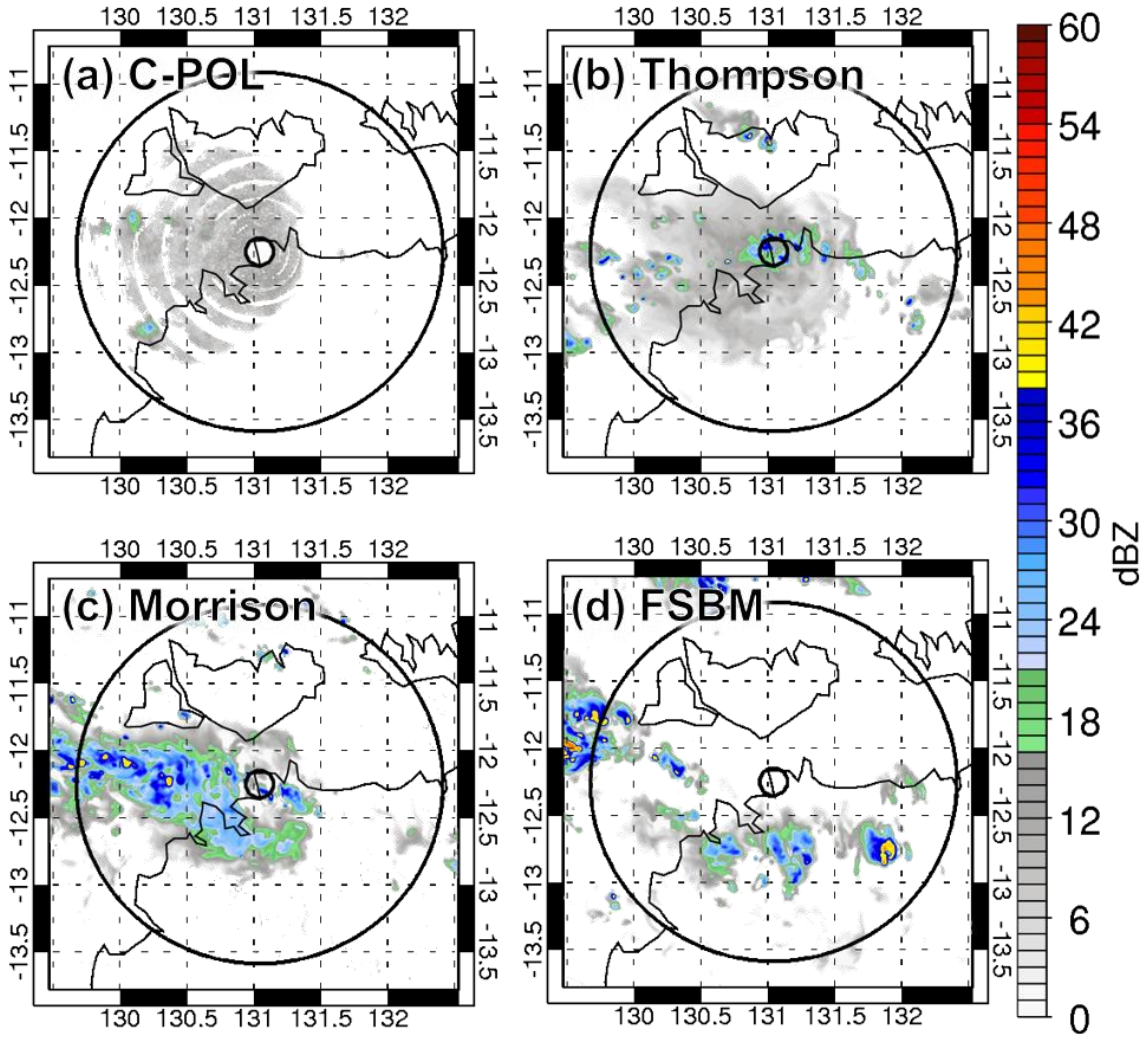

Figure 5.3. As in Figure 5.1 for 10.75-km altitude.

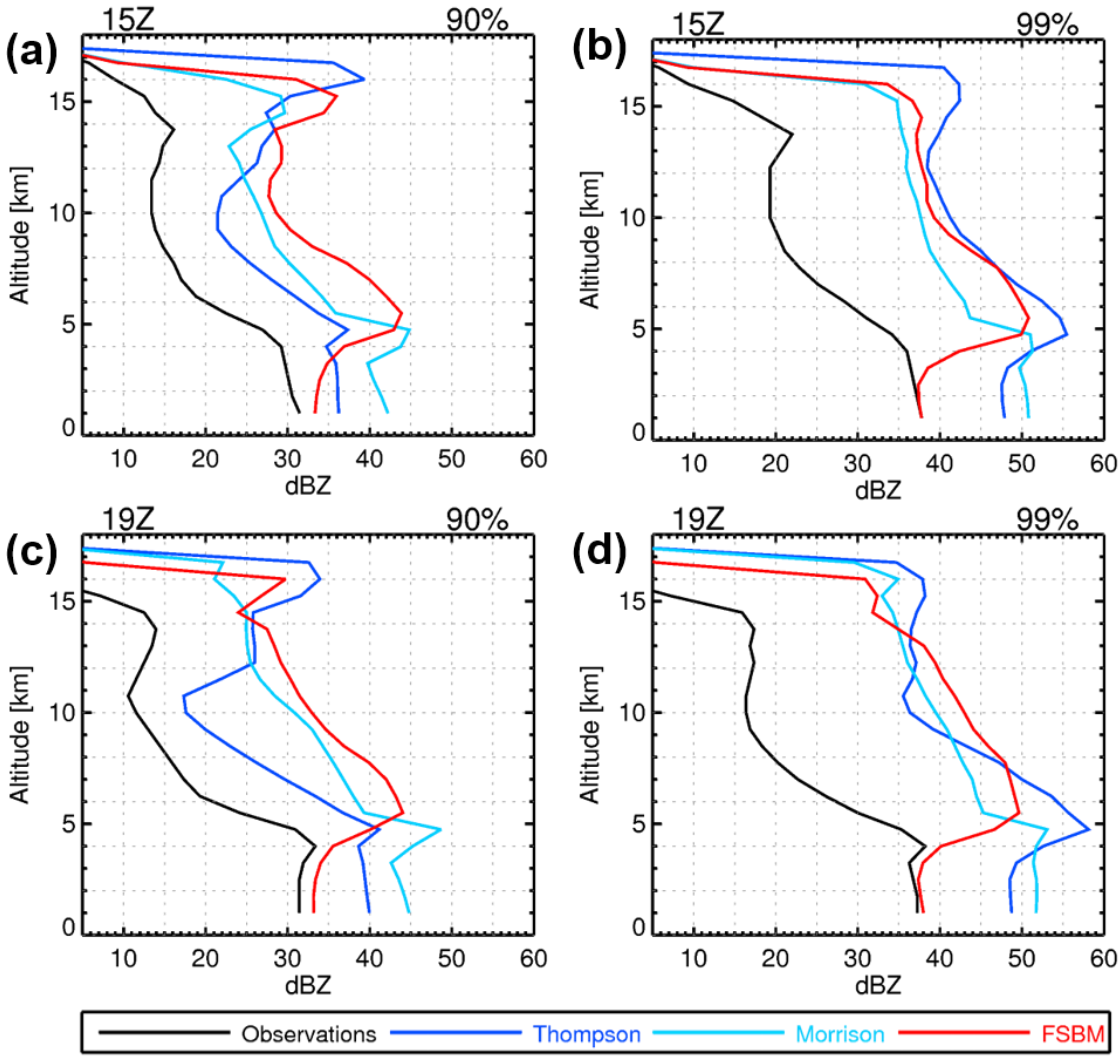

Figure 5.4. Rayleigh reflectivity profiles for the observed and simulated 18 February 2014 case. Only reflectivity values ≥ 5 dBZ are included. The 90th and 99th percentiles for 15Z are shown in (a) and (b) and for 19Z in (c) and (d). Observed C-POL reflectivity is in black, Thompson in dark blue, Morrison in cyan, and FSBM in red.

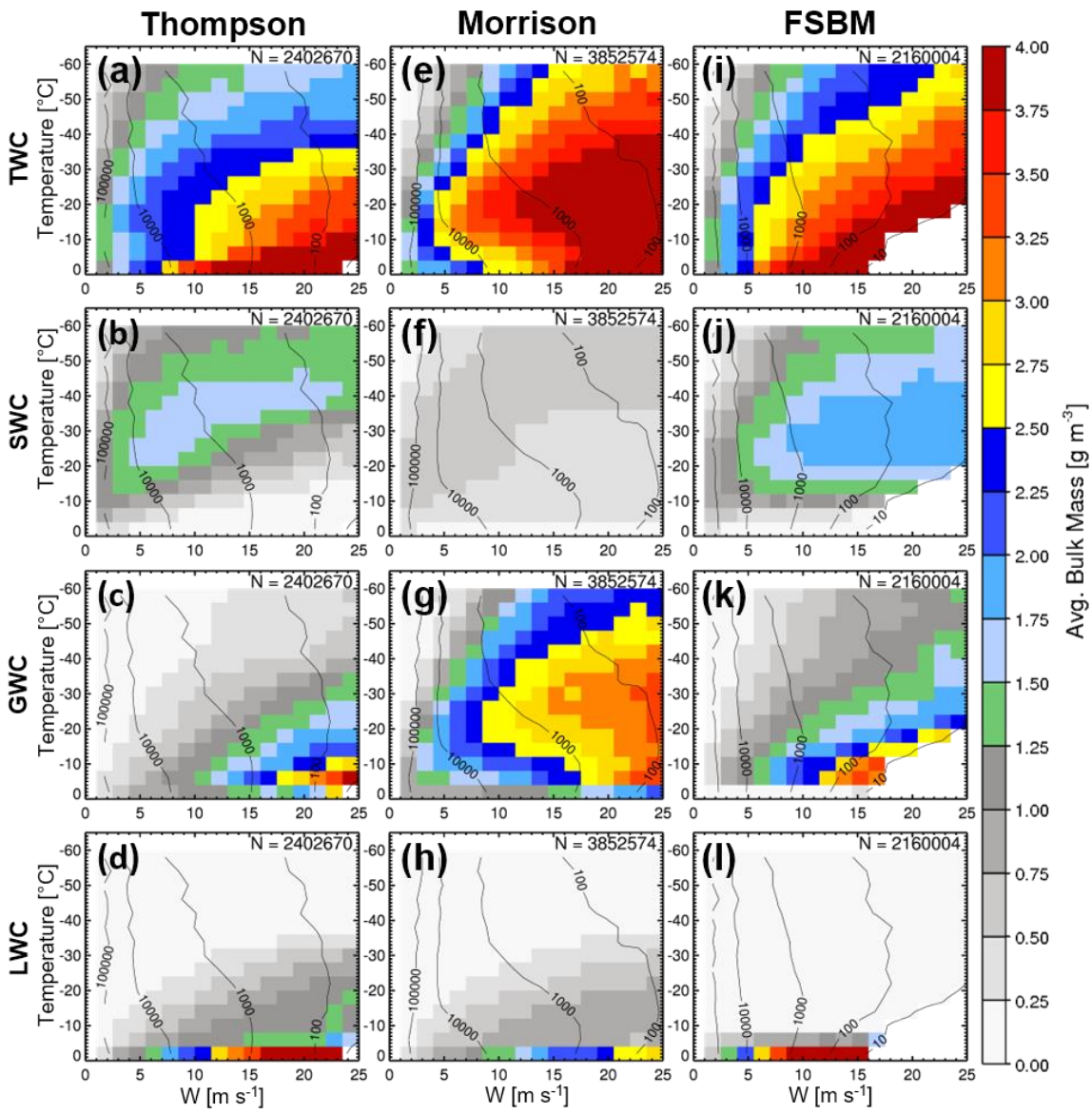

Figure 5.5. Joint histograms of vertical velocity and temperature below freezing using bin sizes of 1.5 m s^{-1} for *w* and 4 °C for temperature. Color-fill is average TWC for (a),(e), and (i), average SWC for (b), (f), and (j), average GWC for (c), (g), and (k), and average LWC for (d), (h), and (l). The Thompson scheme is shown in (a)-(d), Morrison in (e)-(h), and FSBM in (j)-(l). Samples sizes are shown in the upper right corner, and order of magnitude sample sizes are contoured in black.

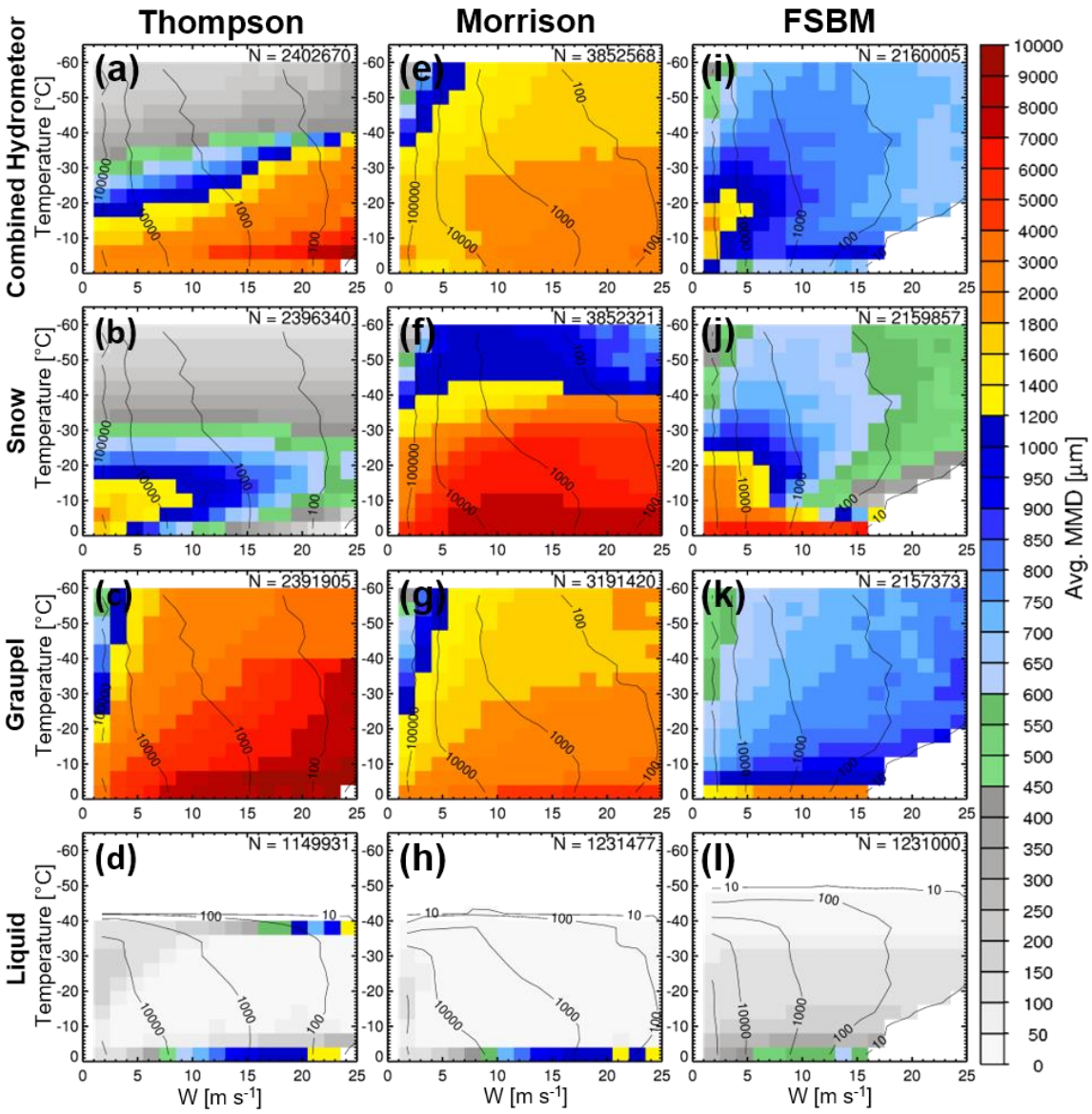

Figure 5.6. As in Figure 5.5, but the color-fill is average MMD for combined hydrometeor size distributions in (a), (e), and (i), snow in (b), (f), and (j), graupel in (c), (g), and (k), and liquid in (d), (h), and (l). Note that the color bar bins do not increase linearly.

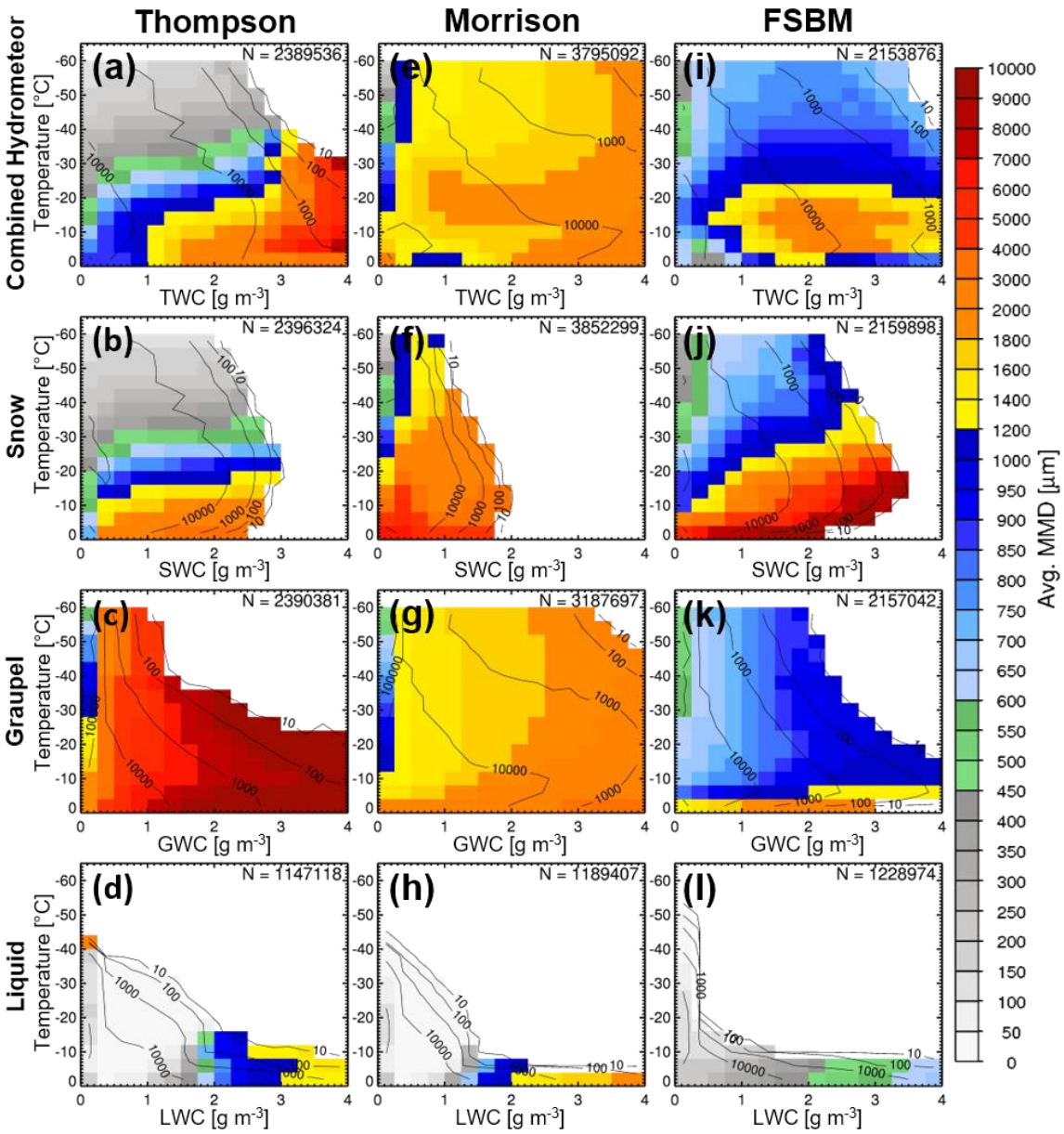

Figure 5.7. As in Figure 5.6, but for bins of temperature and TWC bins in (a), (e), and (i), SWC bins in (b), (f), and (j), GWC bins in (c), (g), and (k), and LWC bins in (d), (h), and (l). Species bulk mass bin sizes are 0.25 g m^{-3}. All data points have $w > 1$ m s^{-1}.

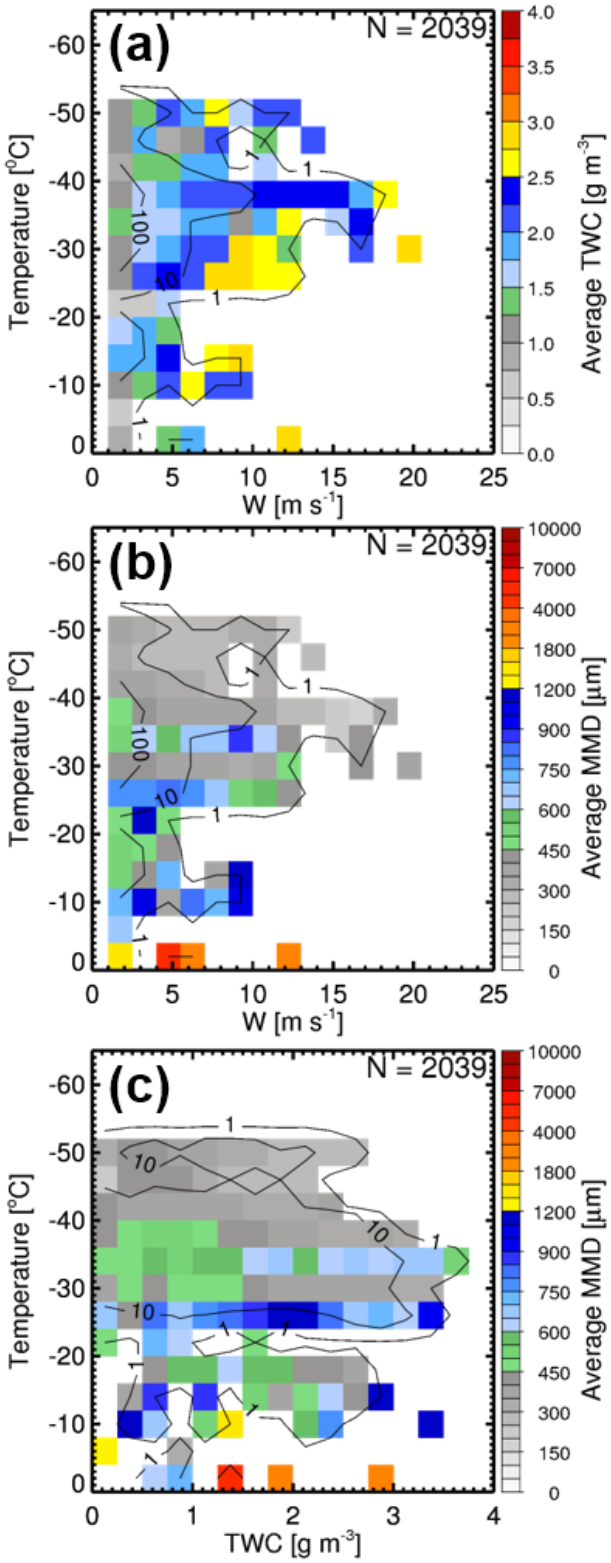

Figure 5.8. Observational joint histograms for data from the Darwin phase of HAIC-HIWC. (a) *w*-T bins color-filled with average TWC, (b) *w*-T bins color-filled with average MMD, and (c) TWC-T bins color-filled with average MMD.

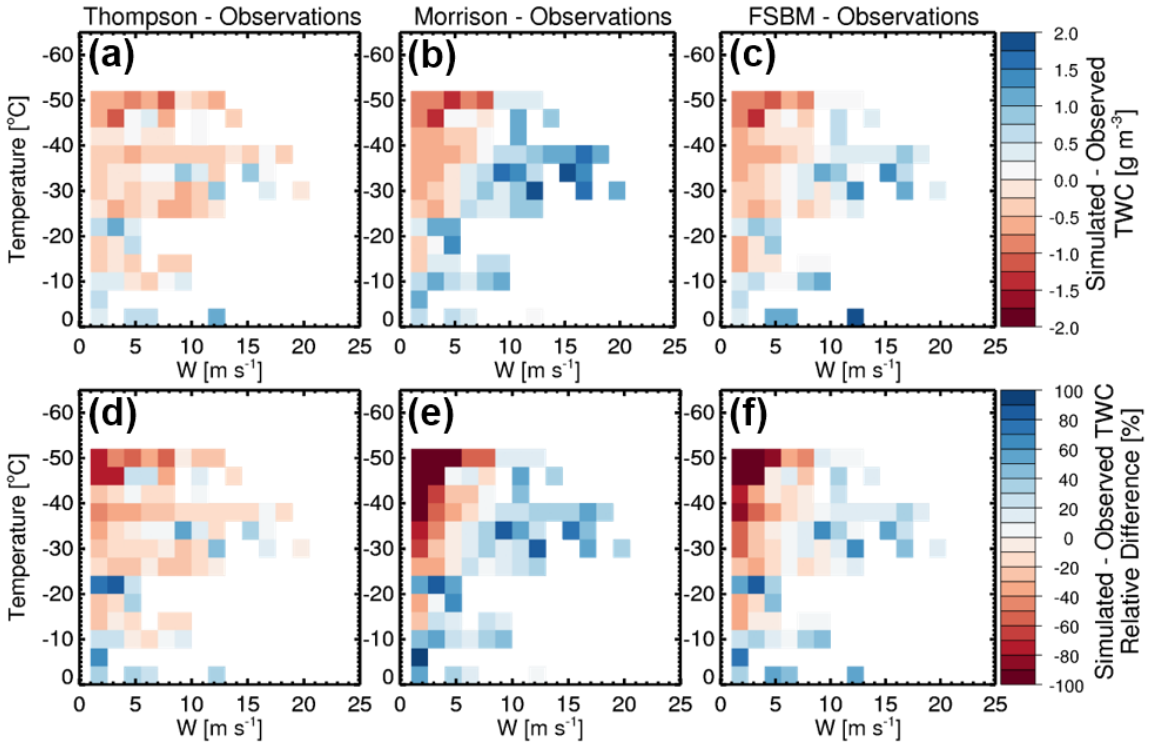

Figure 5.9. Joint histograms for *w*-T bins color-filled with differences (model – observations) between observed and simulated TWC for Thompson (a and d), Morrison (b and e), and FSBM (c and f). Only bins where observational data are present are shown. Absolute differences are shown in (a)-(c) with bin sizes of 0.25 g m^{-3}. Differences relative to the mean (%) are shown in (d)-(f) with bin sizes of 20%.

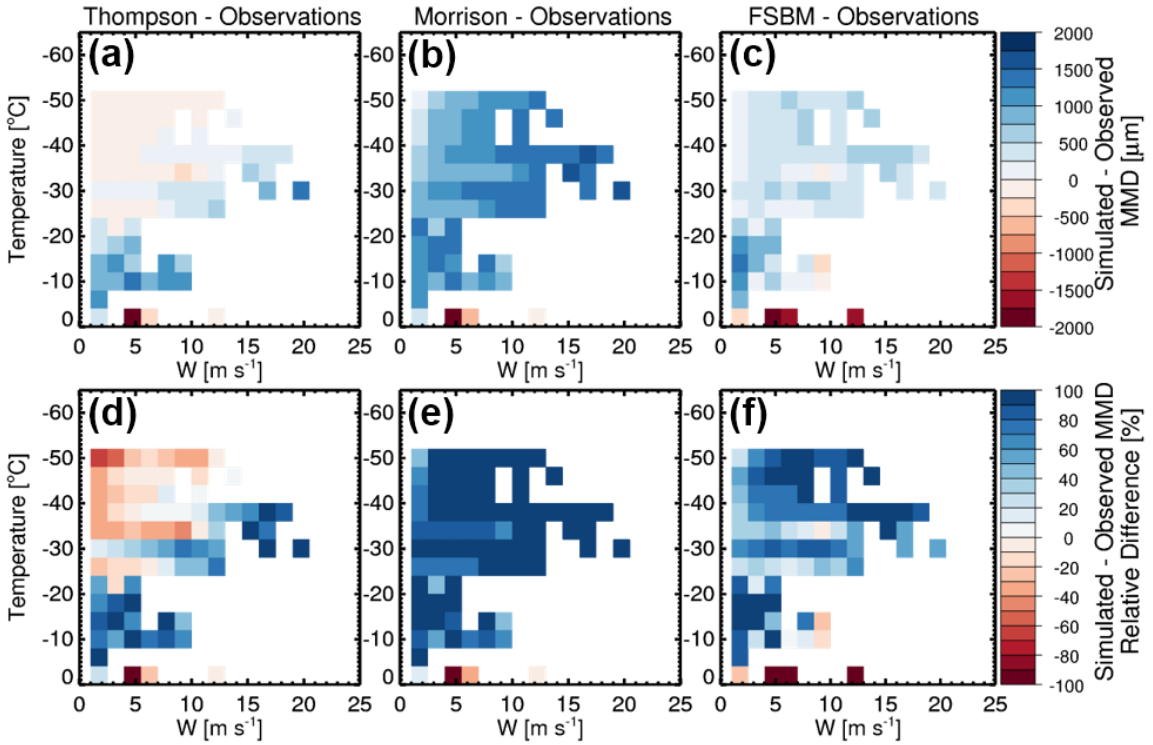

Figure 5.10. As in Figure 5.9, but for observed MMDs subtracted from simulated MMDs. Absolute difference bins sizes in (a)-(c) are 250 μm and relative difference bin sizes in (d)-(f) are 20%.

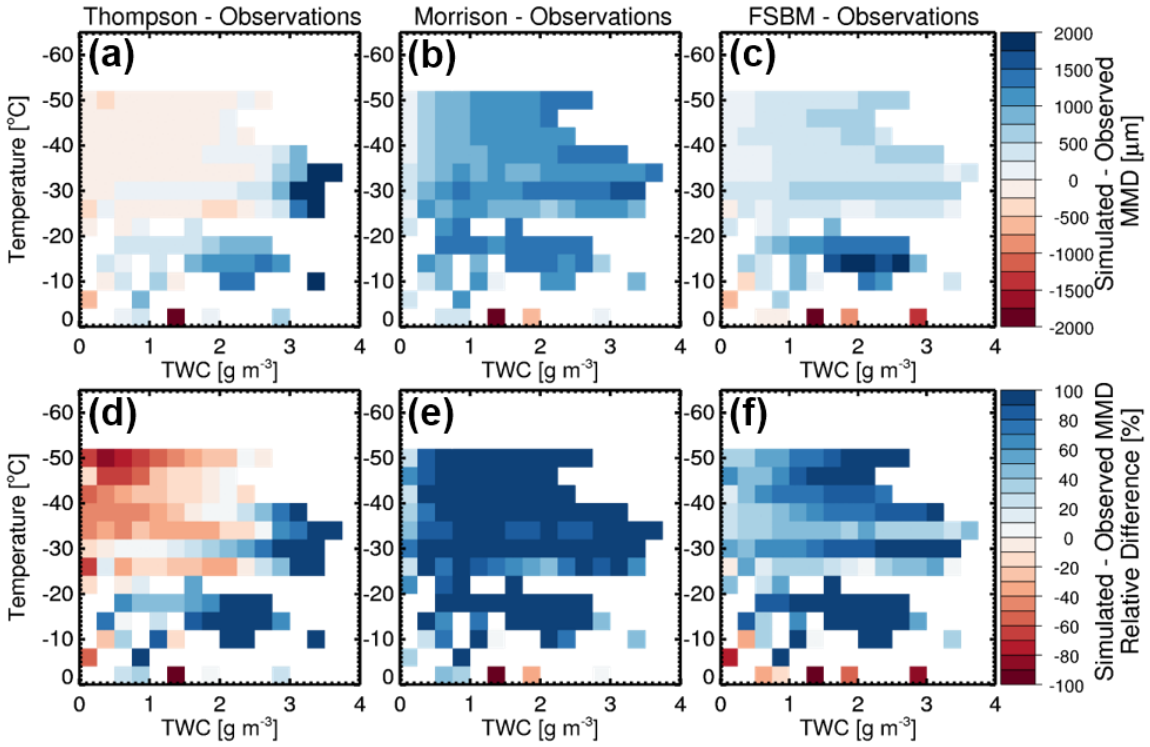

Figure 5.11. As in Figure 5.10, but for TWC-T bins.

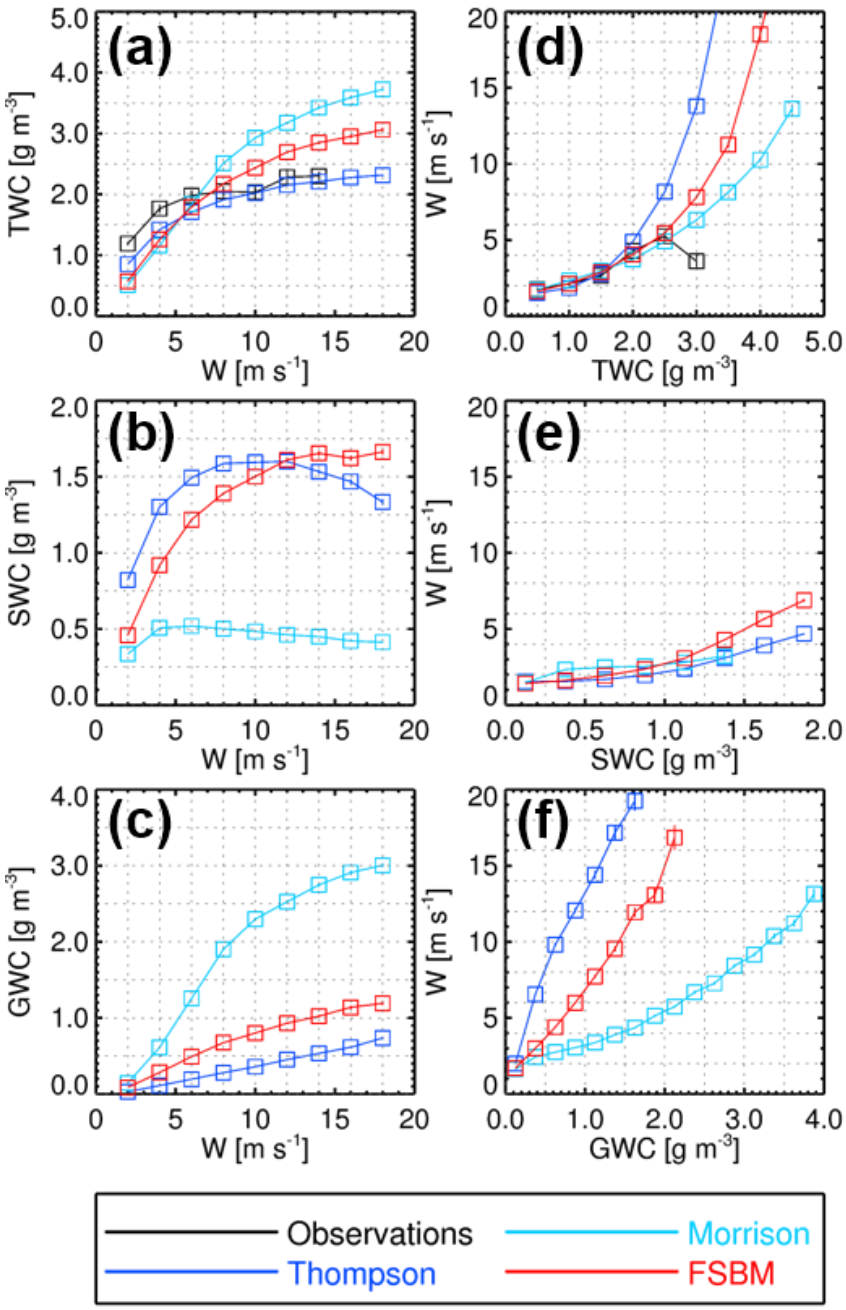

Figure 5.12. Average bulk mass as a function of average *w* and average *w* as a function of average bulk mass for temperatures between -32 °C and -40 °C. Observations are shown in black (a and d only), Thompson in dark blue, Morrison in cyan, and FSBM in red with standard error bars shown in respective colors. Note that most standard errors are small due to large sample sizes and that the axis ranges for bulk mass vary between species. (a)-(c) Average TWC, SWC, and GWC as a function of *w* bins, respectively, with *w* bin widths of 2 m s^{-1}. (d)-(f) Average *w* as a function of TWC, SWC, and GWC bins, respectively. TWC bin widths are 0.5 g m^{-3}, SWC bin widths are 0.25 g m^{-3}, and GWC bin widths are 0.25 g m^{-3}.

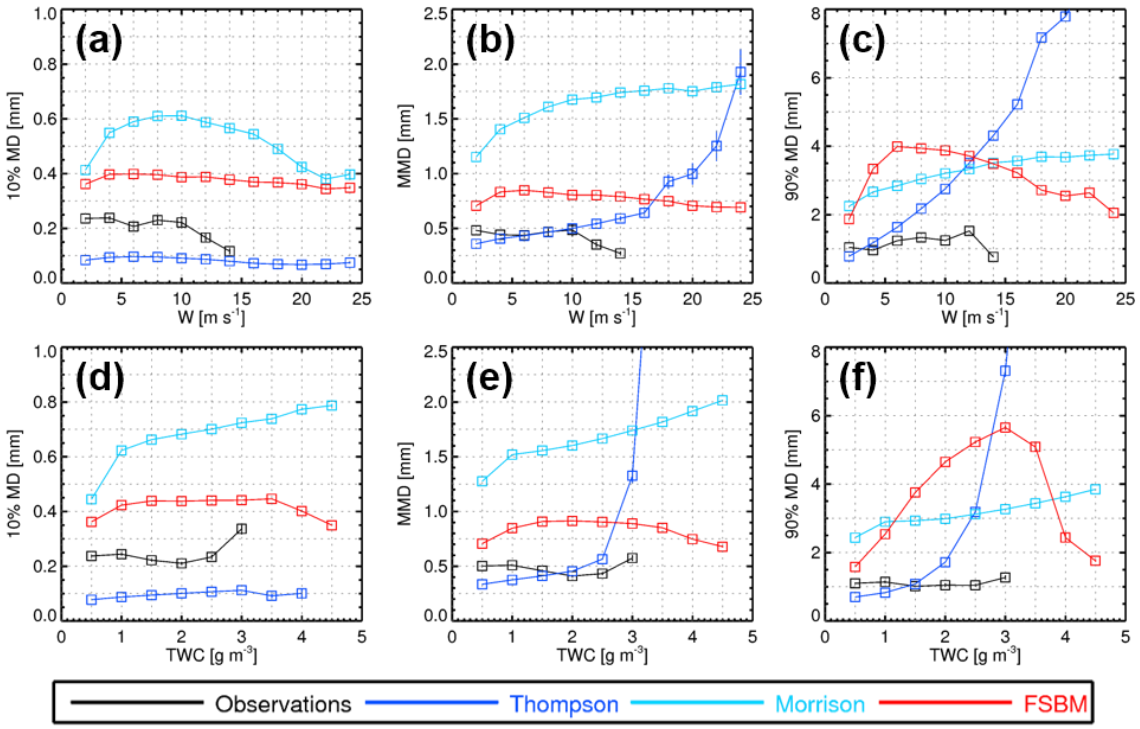

Figure 5.13. Average percentile mass diameters as a function of *w* and bulk mass. Observations are shown in black, Thompson in dark blue, Morrison in cyan, and FSBM in red for temperatures between-32 °C and -40 °C. Standard error bars are shown in respective colors. Note that standard errors are small due to large sample sizes. (a)-(c) 10% MD, MMD, and 90% MD as a function of *w* bins with *w* bin widths of 2 m s^{-1}. (d)-(f) 10% MD, MMD, and 90% MD as a function TWC bins with TWC bin widths of 0.5 g m^{-3}.

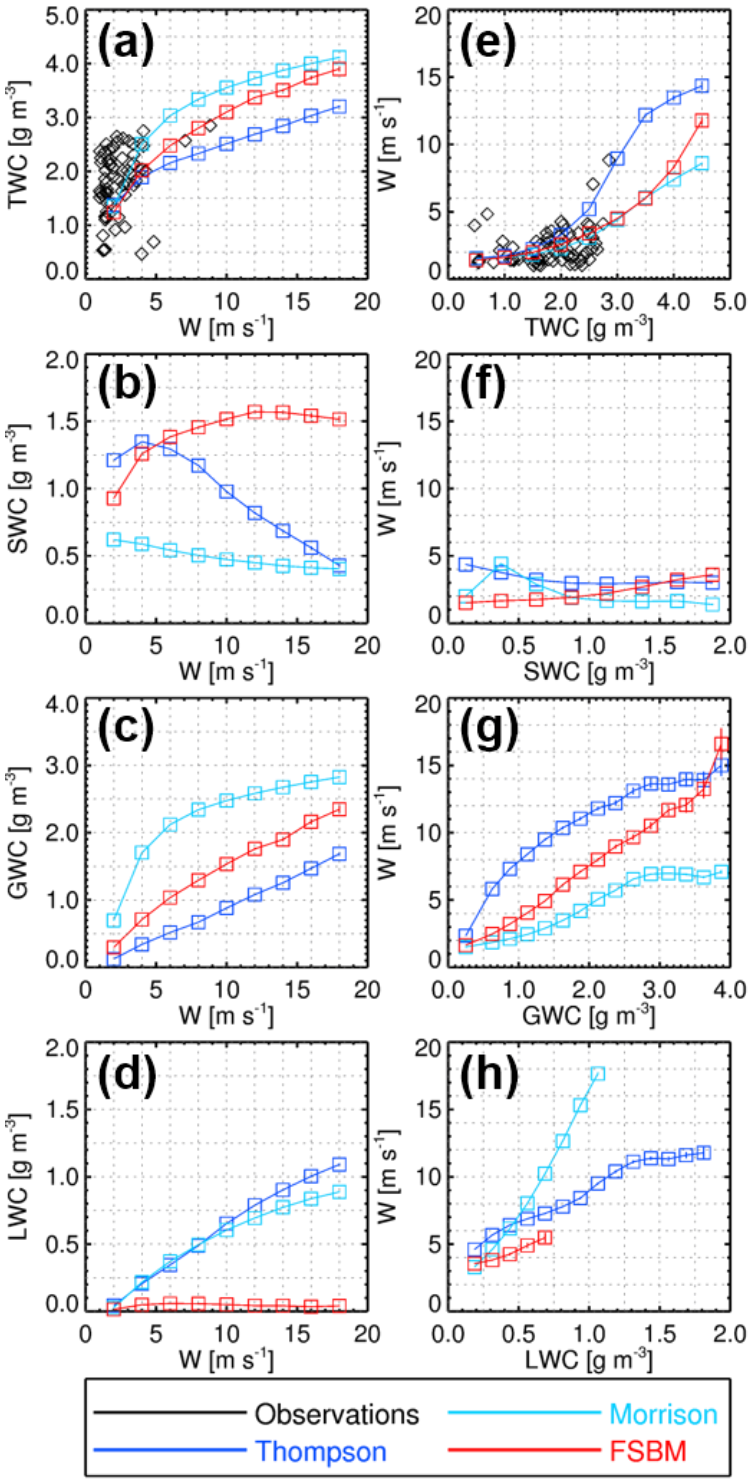

Figure 5.14. As in Figure 5.12, but for temperatures between -12 °C and -20 °C and the inclusion of LWC as a function of *w* (d) and *w* as a function of LWC (h), with LWC bin widths of 0.125 g m^{-3}. Observed symbols in (a) and (e) are plotted as black diamonds for individual data points because of few samples in this temperature range. Note that the axis ranges for bulk mass vary between species.

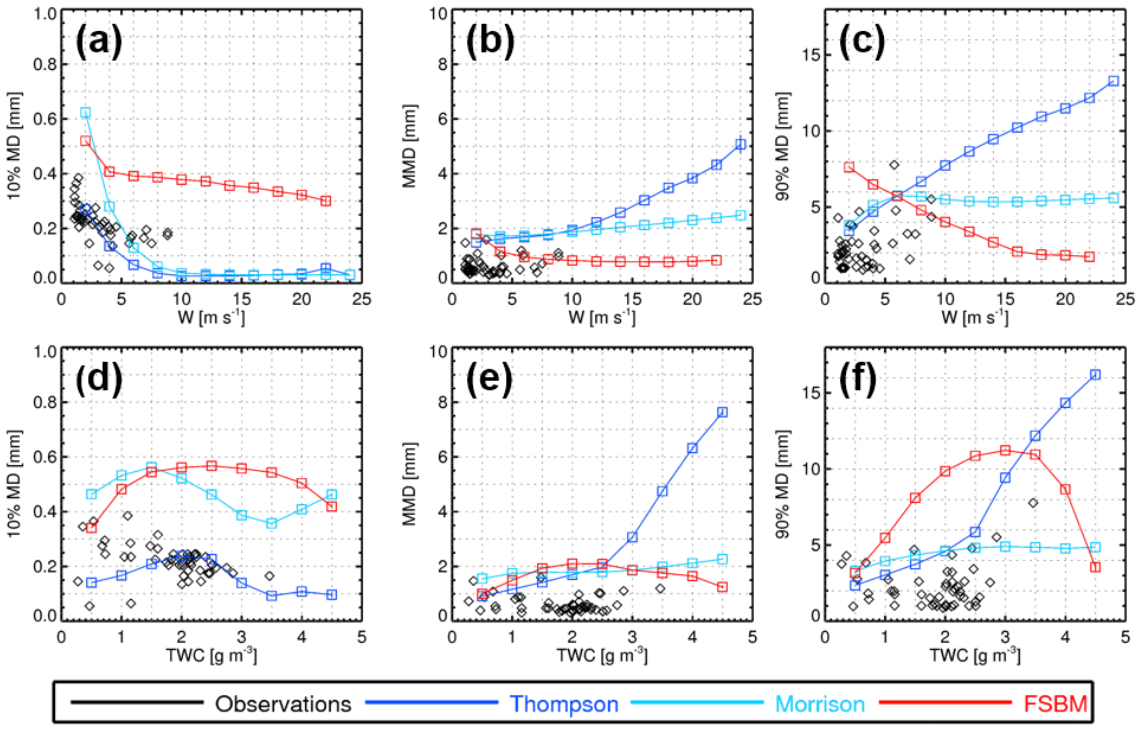

Figure 5.15. As in Figure 5.13, but for temperatures between -12 °C and -20 °C. Observations are plotted in black diamonds for individual data points because of few samples in this temperature range. Note that the ordinate ranges are different from Figure 5.13.

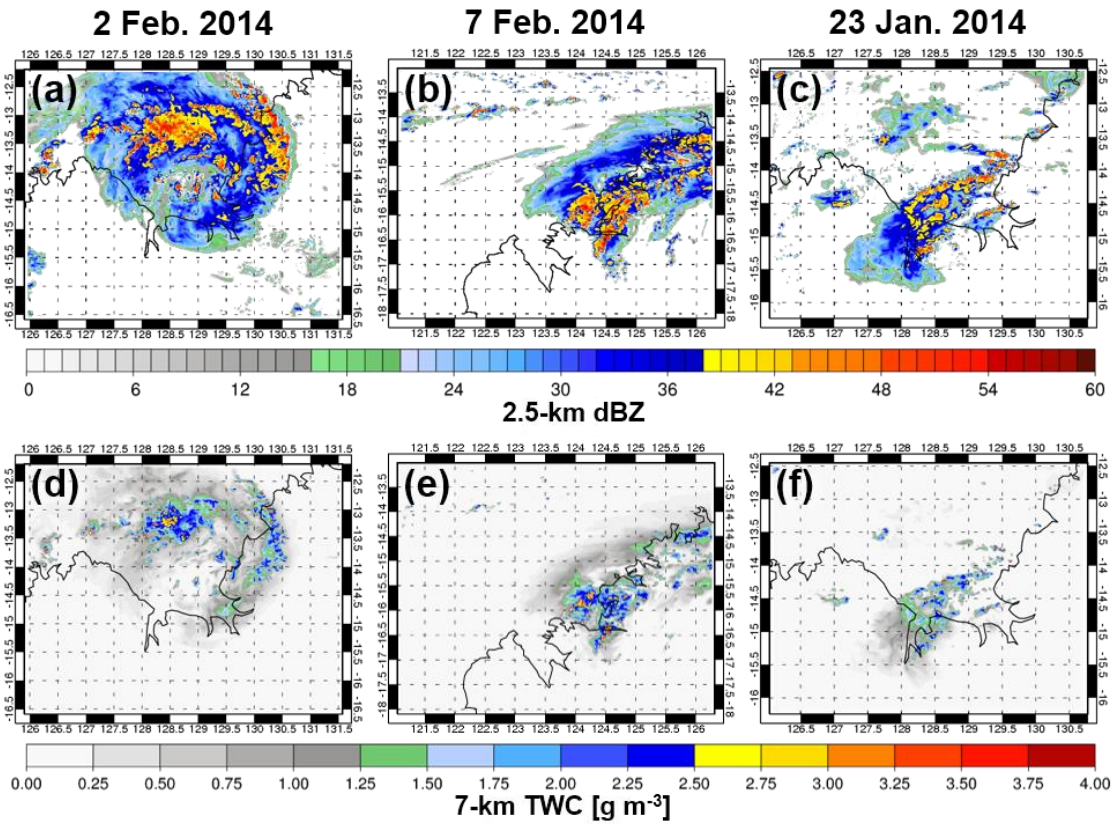

Figure 5.16. Representative Thompson scheme cross-sections of 2.5-km horizontal radar reflectivity and 7-km TWC for various simulated MCS events. Reflectivity cross-sections are shown in (a)-(c) and TWC cross-sections are shown in (d)-(f). Simulations are for MCS events on 2 February 2014 (a and d), 7 February 2014 (b and e), and 23 January 2014 (c and f), respectively.

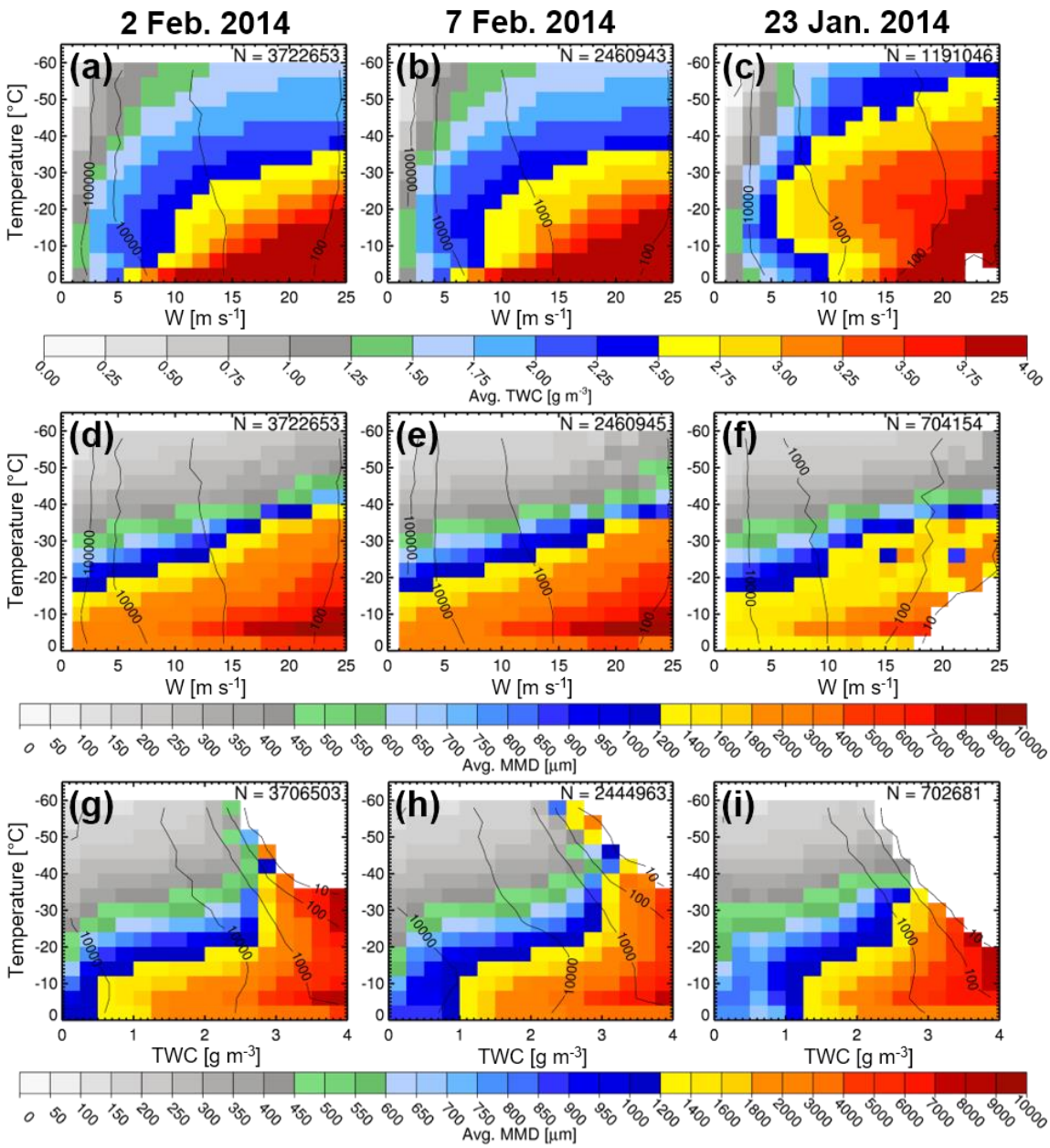

Figure 5.17. Thompson scheme joint histograms for various simulated MCS events. (a)-(c) *w*-T joint histograms color-filled with average TWC for simulations of 2 February 2014, 7 February 2014, and 23 January 2014, respectively. (d)-(f) *w*-T joint histograms color-filled with average MMD for respective simulations. (g)-(i) TWC-T joint histograms color-filled with average MMD for respective simulations.

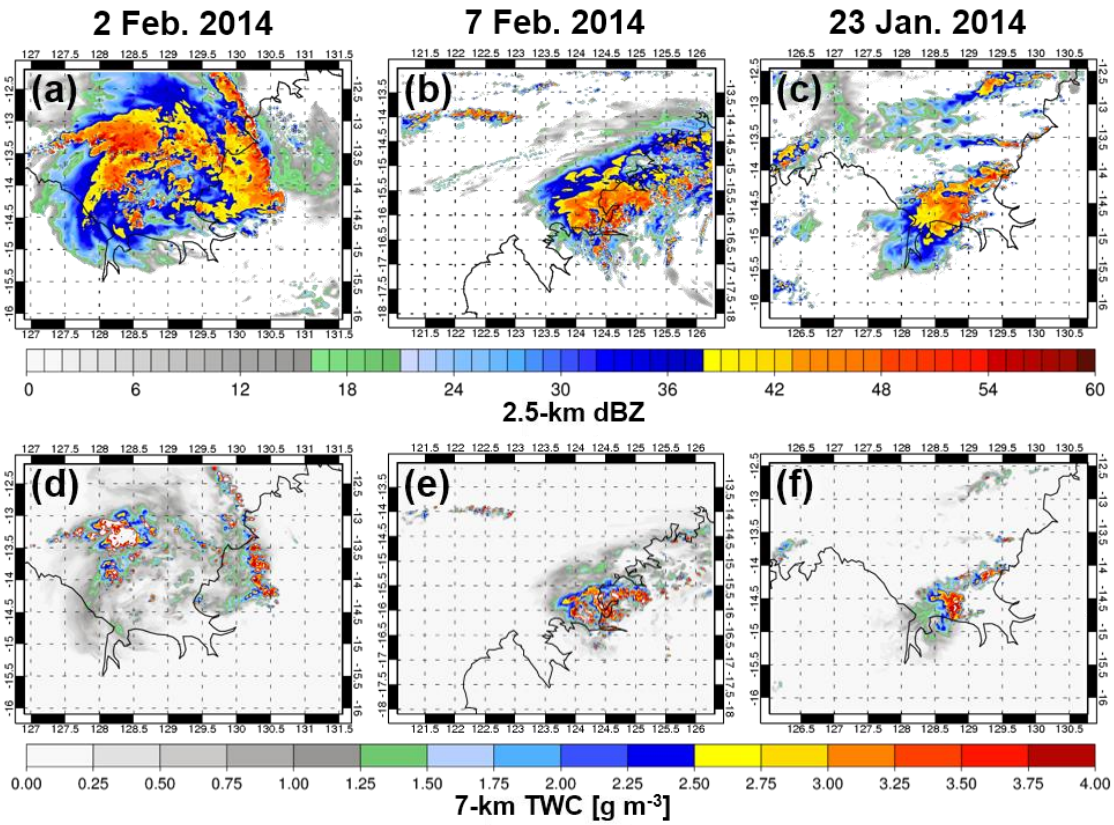

Figure 5.18. As in Figure 5.16 for Morrison simulations.

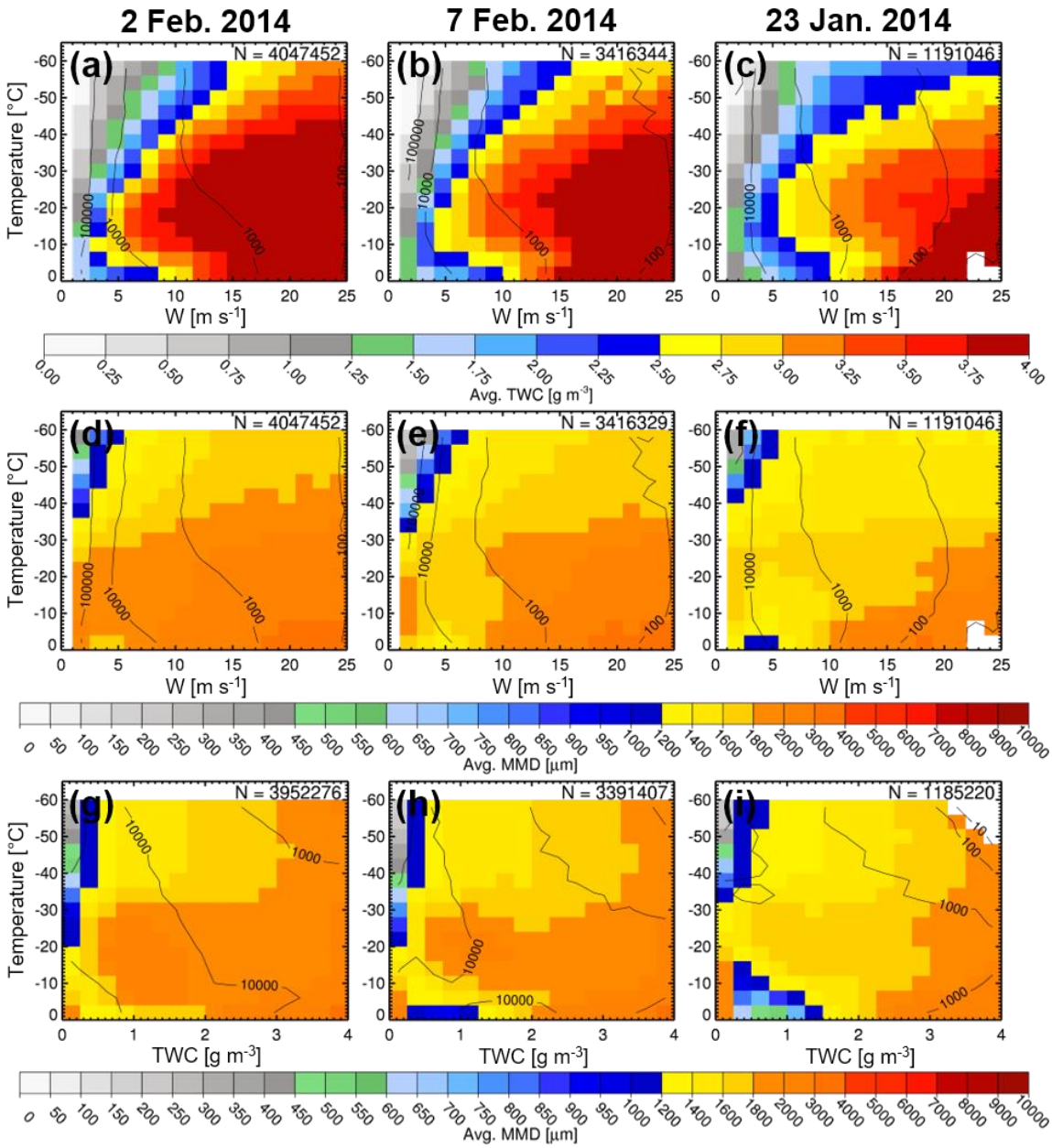

Figure 5.19. As in Figure 5.17 for Morrison simulations.

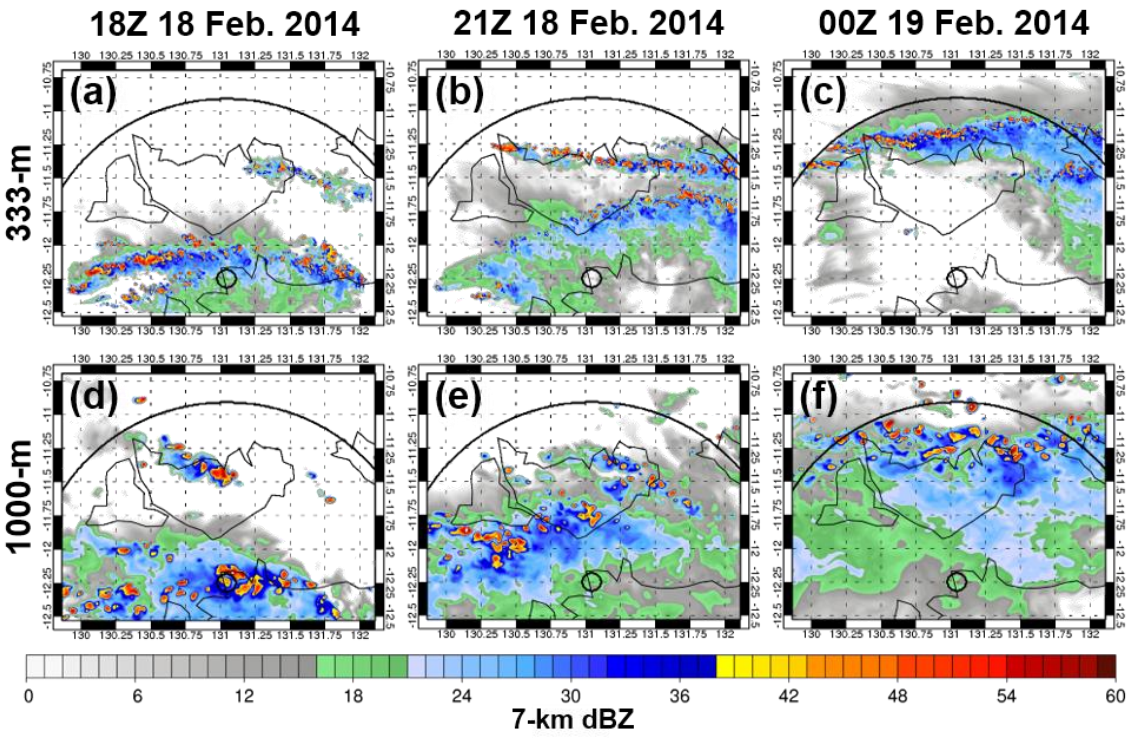

Figure 5.20. Thompson 333-m grid spacing 7-km radar reflectivity horizontal cross-sections for 18Z on 18 February 2014 (a), 21Z on 18 February 2014 (b), and 00Z on 19 February 2014 (c). (d)-(f) are as in (a)-(c) but for the 1000-m grid spacing simulation limited to the 333-m domain.

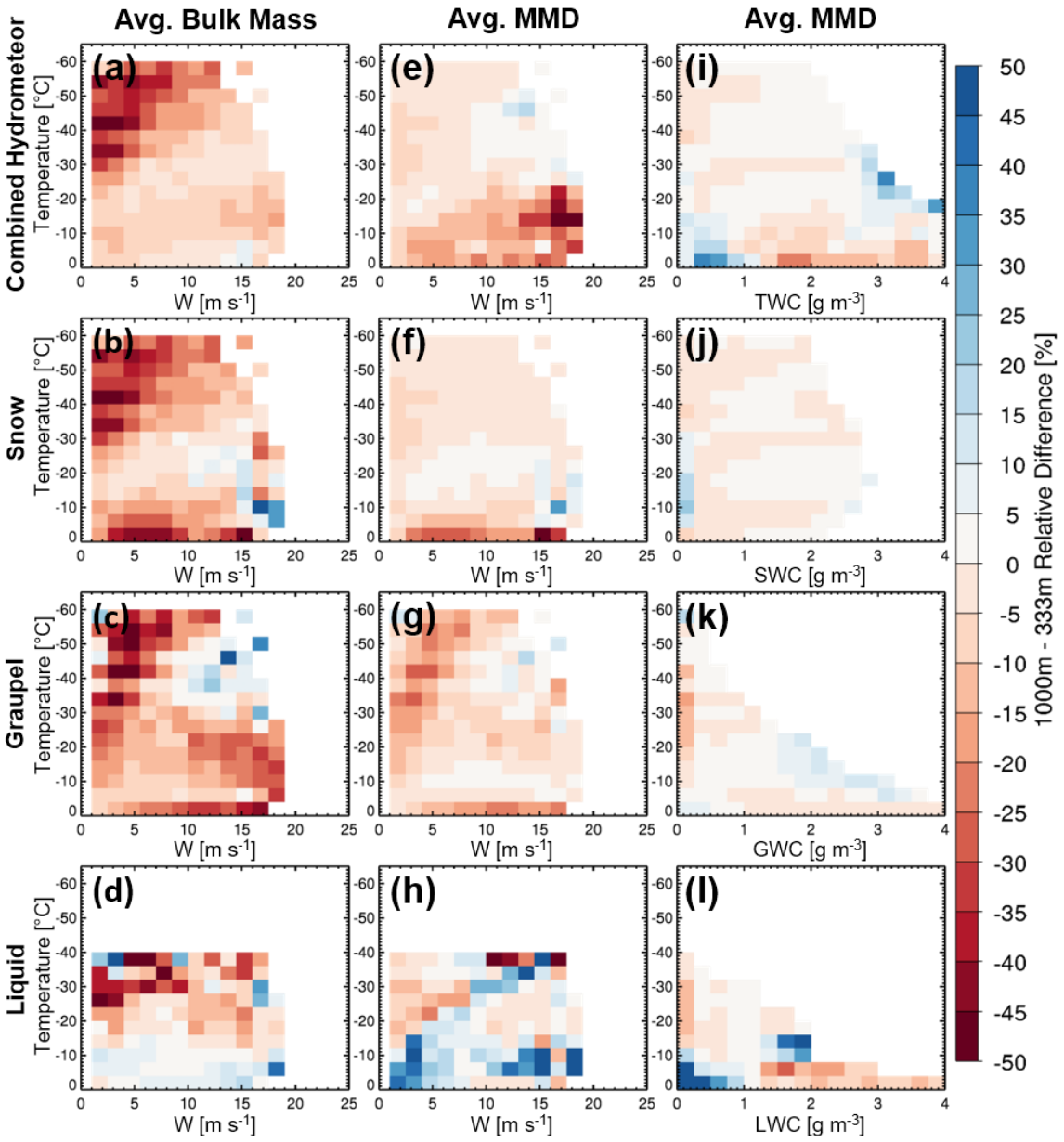

Figure 5.21. Joint histograms of relative differences (%) between average properties from the 1000-m Thompson simulation and the 333-m Thompson simulation (1000-m subtracted from 333-m). (a)-(d) Average TWC, SWC, GWC, and LWC as a function of *w* and T. (e)-(h) Average MMDs for combined hydrometeors, snow, graupel, and liquid as a function of *w* and T. (i)-(l) Average MMDs for combined hydrometeors, snow, graupel, and liquid as function of T and species bulk mass. Data from the 1000-m simulation are limited to domain from the 333-m simulation.

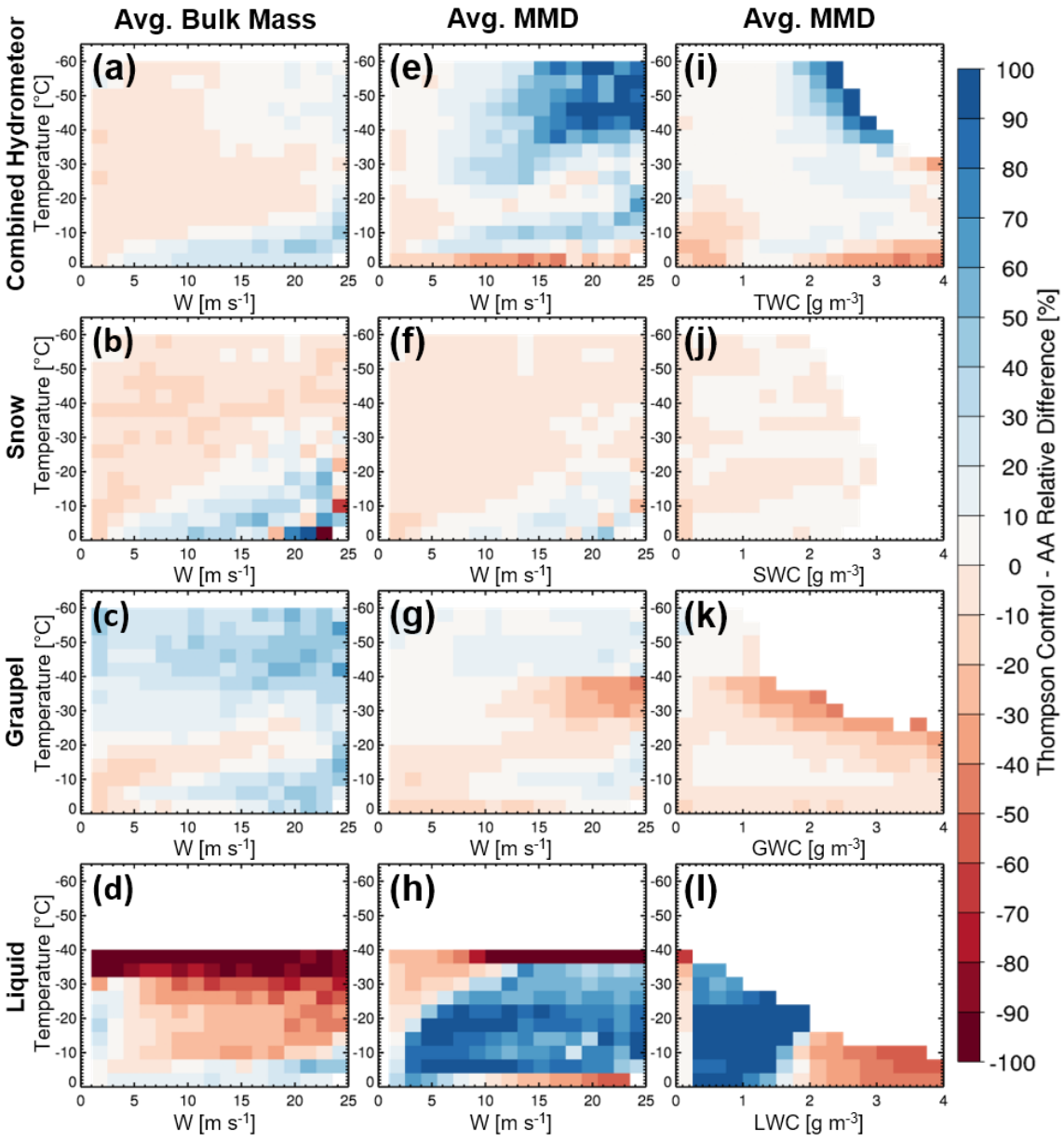

Figure 5.22. Joint histograms of relative differences (%) between average properties from the 1000-m Thompson simulation and the Thompson aerosol-aware (AA) simulation (control subtracted from AA). (a)-(d) Average TWC, SWC, GWC, and LWC as a function of *w* and T. (e)-(h) Average MMDs for combined hydrometeors, snow, graupel, and liquid as a function of *w* and T. (i)-(l) Average MMDs for combined hydrometeors, snow, graupel, and liquid as function of T and species bulk mass.

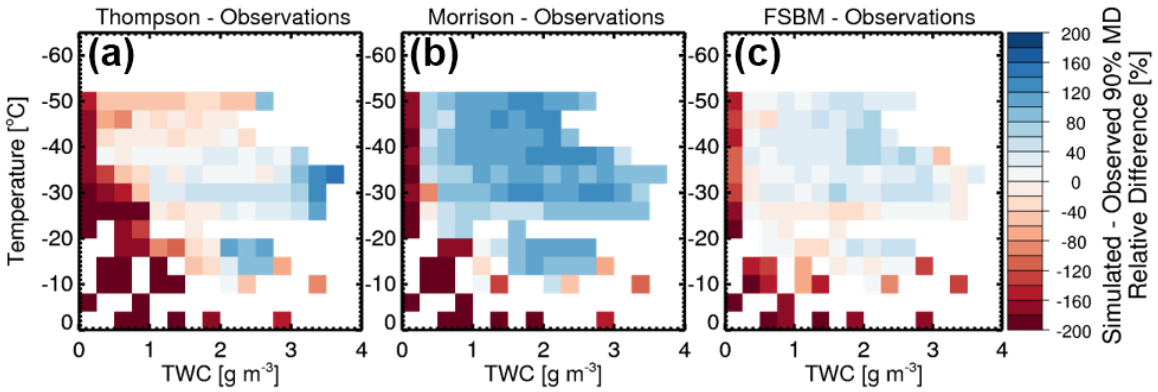

Figure 5.23. Relative differences between simulated and observed minimum 90% MDs for TWC-T bins. Relative difference bin widths are 20%. Note that the relative difference color bar ranges from -200% to 200%.

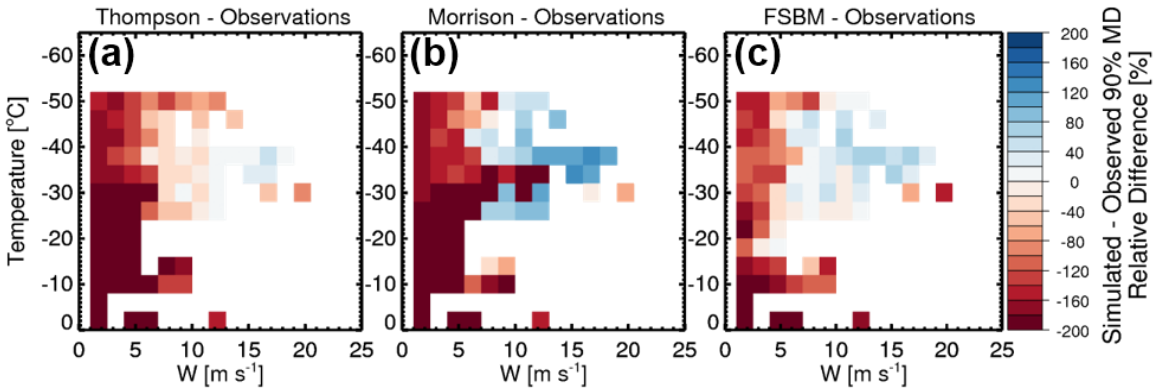

Figure 5.24. As in Figure 5.23, but for *w*-T bins.

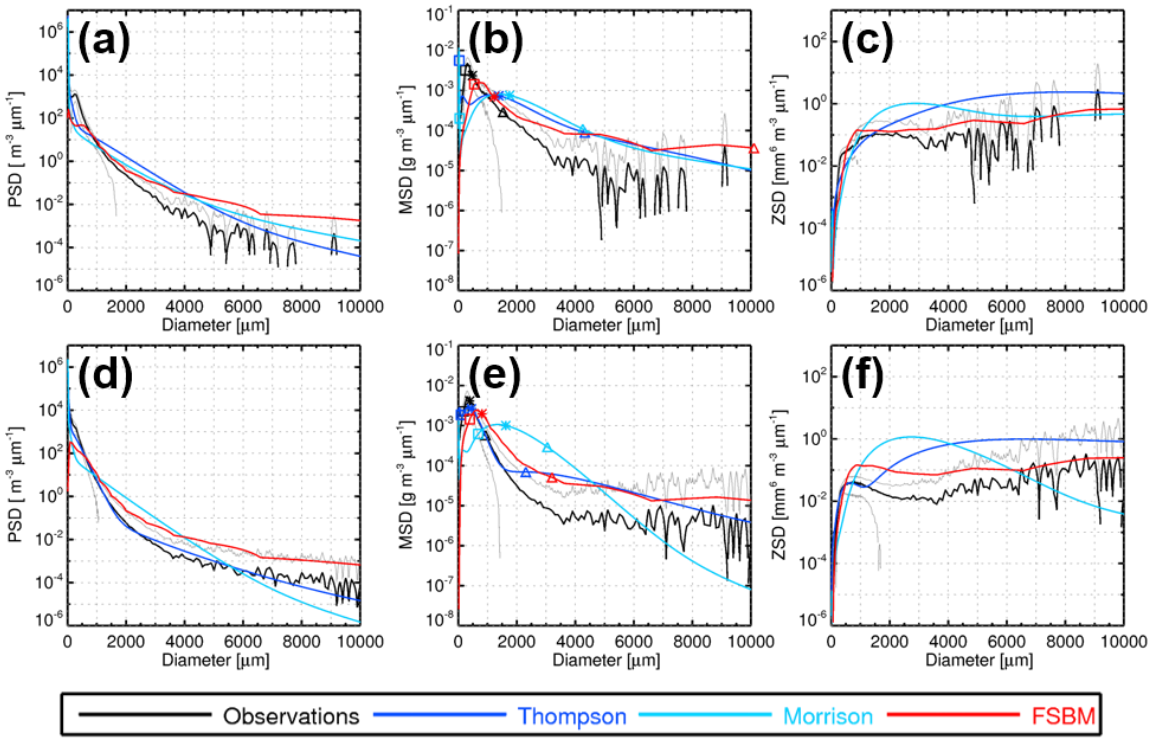

Figure 5.25. Observed and simulated composite PSDs, MSDs, and ZSDs for TWC between 2 and 2.5 g m^{-3}. Squares, asterisks, and triangles overplotted on MSDs (b and e) are the 10% MD, MMD, and 90% MD, respectively, of each composite distribution. Grey lines indicate one standard deviation from the composite mean. Data points with temperatures between -12 °C and -20 °C are shown in (a)-(c), and data points with temperatures between -32 °C and -40 °C are shown in (d)-(f).

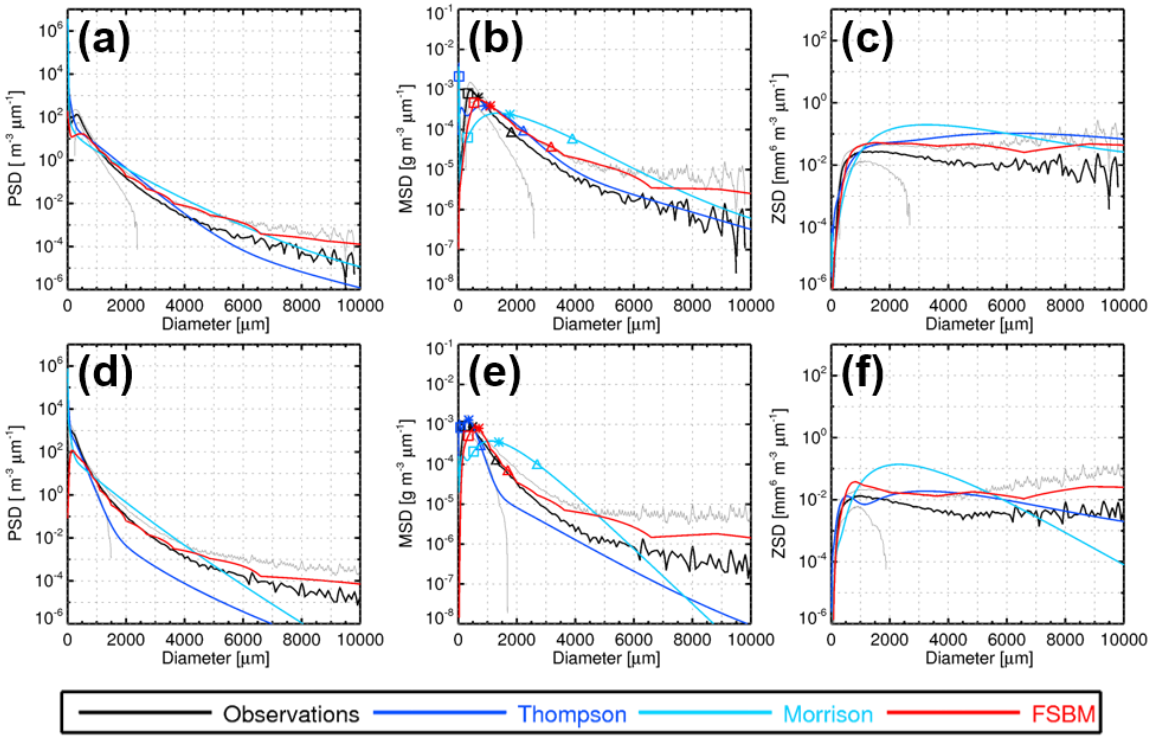

Figure 5.26. As in Figure 5.25, but for TWC between 0.5 and 1 g m^{-3}.

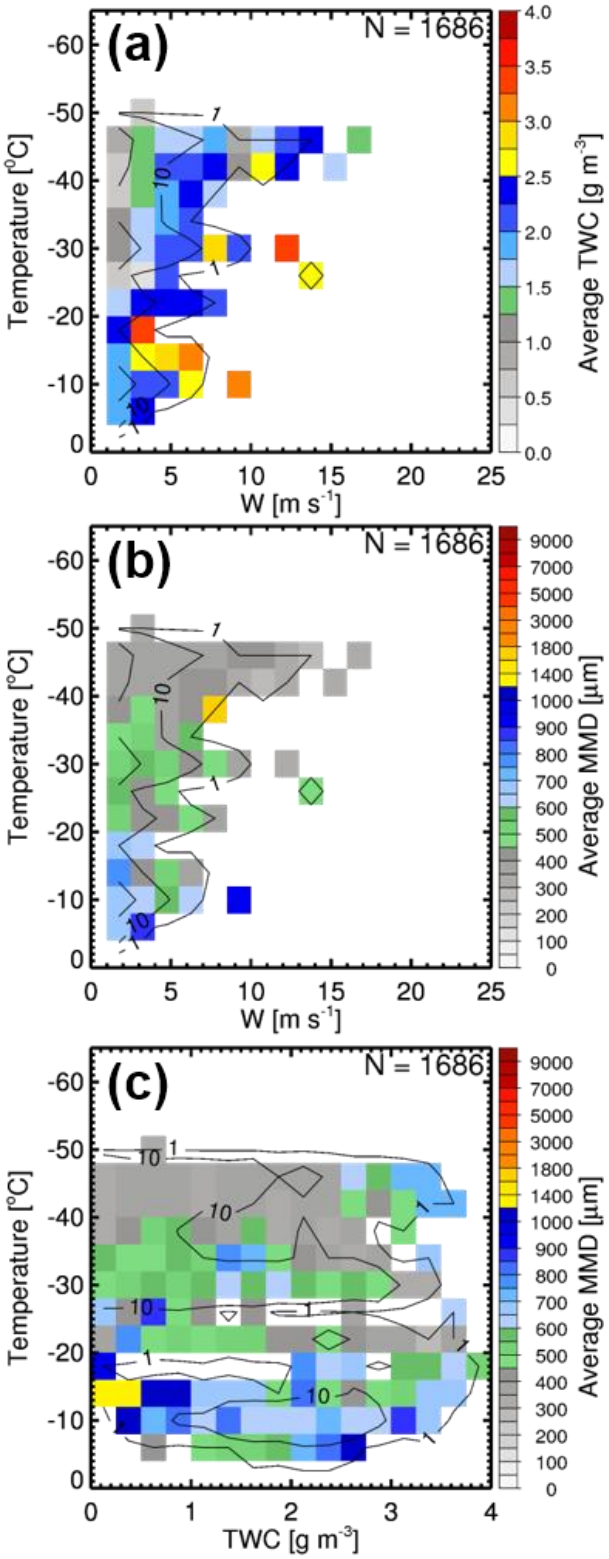

Figure 5.27. Observational joint histograms for data from the Cayenne phase of HAIC-HIWC. (a) *w*-T bins color-filled with average TWC, (b) *w*-T bins color-filled with average MMD, and (c) TWC-T bins color-filled with average MMD.

CHAPTER 6

CONCLUSIONS

6.1 Summary

The accuracy of microphysics parameterizations is limited by the accuracy of simplified descriptions of hydrometeor properties and microphysical processes. A number of studies have shown that changes in the representation of microphysics can impact the evolution and structure of precipitating systems. It is therefore prudent to address potential microphysical biases in a framework for which as many of these factors are controlled as possible in making comparisons with a high-quality observational dataset.

For this study, two-way nested simulations (9:3:1-km grid spacing) of a tropical MCS that occurred on 18 February 2014 during the HAIC-HIWC field campaign are run using WRF-ARW. The simulations vary only by the microphysics scheme employed (Thompson, Morrison, and FSBM). Documented high biases in simulated radar reflectivity aloft in tropical convective systems are investigated by exploring relationships between hydrometeor size, TWC, and *w* as a function of temperature. This multivariate phase space is used to isolate reflectivity biases that result from parameterized hydrometeor properties and microphysical processes from those that result from the lofting of excessive condensate mass in overly strong or large convective

updrafts. While reflectivity biases in simulated tropical convection have been previously shown to exist in bulk schemes, this study shows that biases exist in bin schemes as well.

Simulated MMDs are larger than observed in every microphysics scheme for a given *w*, TWC, and temperature, and differences are especially pronounced for higher *w* and TWC values. Differences in observed and simulated upper percentile diameters of the mass-size distribution are also large. For a given *w*-T or TWC-T bin, simulated sample sizes are around 10^3 times larger than observations. Despite this significant difference in sample size, minimum simulated 90% mass diameters for a given *w*-T or TWC-T bin are larger than minimum observed 90% mass diameters for the same bins. The species that contributes most to this hydrometeor size bias varies between schemes. Simulating an additional three cases from HAIC-HIWC using the Morrison and Thompson schemes shows that primary differences between different simulated events lie in the strength of convective updrafts and the amount of lofted condensate mass rather than differences in hydrometeor size.

Of the three schemes used, the Thompson scheme reproduces observed hydrometeor sizes best at temperatures colder than -30°C, which is not entirely surprising. Vapor-grown ice particles largely control the bulk mass at these temperatures, and the Thompson scheme uses a sophisticated representation of the snow PSD that forces snow to smaller sizes with decreasing temperature. Although these small snow sizes are diagnosed rather than produced by a microphysical process, they still suggest using a nonspherical mass-size relationship in which density varies by size and an appropriate PSD function with limited large particle sizes can nearly reproduce observations at cold temperatures where snow contributes most to bulk mass.

Although the Thompson scheme's snow representation appears to improve simulated hydrometeor sizes at cold temperatures, larger differences in size exist at higher TWC and *w* values and warmer temperatures, where TWC is largely controlled by the hybrid graupel-hail species. These large graupel sizes are a result of diagnostically varying the graupel intercept parameter N_0 inversely with its mass mixing ratio q, which produces very large graupel sizes for large mass mixing ratios, while the fall speed relationship transitions to hail fall speeds at large particle sizes. These faster fall speeds aid in sedimenting graupel out of updrafts quickly, but because graupel sizes are so large, only a small mass is needed to high-bias radar reflectivities, which is consistent with findings from Varble et al. (2014a). While all schemes produce hydrometeor size biases for a given TWC, *w,* and temperature, the Thompson scheme only predicts *N* for rain and cloud ice while using diagnostic relationships for graupel and snow, decreasing computational expense compared to schemes that predict *N* for additional species. This is an important consideration for computationally expensive simulations, which need to balance accuracy with computational costs.

The Morrison scheme allows for much greater variability in graupel and snow size since it predicts *N* for both species. This often shifts graupel to smaller sizes by several millimeters compared to the Thompson scheme, but it also shifts snow sizes to much larger than in the Thompson scheme to the point of becoming the largest-sized precipitating ice species in most situations, supporting conclusions from Varble et al. (2014a) that snow in addition to graupel contributes to reflectivity high biases. The slower fall speeds of Morrison graupel result in much higher amounts of GWC than SWC in updraft cores, which results in combined hydrometeor MMDs being largely controlled

by graupel even though snow MMDs are larger. Even so, Morrison graupel MMDs alone are larger than observed MMDs for most T-*w*-TWC bins.

The FSBM scheme has a fundamental advantage over the bulk schemes because it makes no assumptions about the PSD shape and it computes microphysical process rates separately for different hydrometeor size bin. Despite this, the FSBM scheme also produces larger than observed MMDs for several T-*w*-TWC bins, particularly at temperatures between -20 °C and 0 °C. However, supercooled liquid is reduced at temperatures less than -8 °C relative to bulk schemes, likely reducing riming, which, combined with smaller raindrops being lofted above the 0 °C level and frozen, leads to the smallest graupel MMDs among the schemes tested. However, as with the Morrison scheme, snow is the largest-sized precipitating ice species in FSBM, reaching sizes > 1 cm for SWC > 2.5 g m^{-3} at relatively warm temperatures. The large SWCs combined with large snow MMDs cause larger than observed particles and high biased reflectivity in FSBM, especially for $w < 10$ m s^{-1} and temperatures warmer than -20 °C.

The FSBM scheme's explicit treatment of CCN activation may be partially responsible for FSBM producing smaller graupel MMDs than are produced in other schemes. CCN consumption in updrafts reduces the potential for new cloud droplet formation at sub-freezing temperatures relative to schemes such as Morrison and Thompson that condense all liquid supersaturation at each time step with a constant cloud droplet concentration. This quickens cloud droplet growth and collision-coalescence in FSBM at lower levels, potentially increasing sedimentation of larger raindrops out of updrafts before reaching the 0 °C level. The smaller raindrops lofted above 0 °C freeze to form smaller graupel compared to other schemes. This feature was also seen in the

Thompson “aerosol-aware” run to a lesser degree, which predicts the number concentration of cloud droplets. However, the FSBM scheme is able to maintain supersaturations over liquid, which may be important in limiting the amount of supercooled liquid available for riming and thus potentially aiding in a decrease in FSBM graupel MMDs. Moreover, although graupel MMDs are reduced in the mixed-phase region of the Thompson AA scheme relative to the non-AA Thompson scheme, larger graupel sizes are produced above the homogeneous freezing level due to easier graupel condensate loading from smaller, slower-falling graupel particles at warmer temperatures. Explicit cloud droplet nucleation therefore appears to aid in reducing hydrometeor size biases, but not nearly enough to eliminate large discrepancies with observations.

Increasing horizontal resolution also appears to reduce size biases in the Thompson scheme. Updraft cores are smaller in a 333-m grid spacing domain than the 1000-m domain, while GWC and SWC are also lesser, likely because of more efficient sedimentation of hydrometeors out of updrafts, which preferentially favors removal of faster-falling large particles before slower-falling small particles. The TWC reduction for most *w*-T bins is accompanied by MMD decreases, but this is largely the result of lesser GWC. Although finer resolution better resolves convective motions and sedimentation, it is clear that simulated hydrometeor sizes will come nowhere close to converging to observed sizes and increasing the resolution does little to change hydrometeor sizes for a given bulk mass.

Composite MSDs retrieved from observations reveal that most condensate mass is distributed in a prominent mode at a diameter of 300 μm, generally regardless of

temperature, *w*, or TWC constraints. Rarely are any of the schemes able to reproduce this, with the exception of the Thompson scheme at cold temperatures and small-moderate TWC. Otherwise, all schemes produce too much mass at large particle diameters, even for TWC < 1 g m^{-3}, though discrepancies with observations are enhanced for larger TWCs and higher *w* values. Equivalent Rayleigh reflectivity size distributions show that the larger amount of mass distributed at large particle sizes in simulations produces reflectivities that are higher by up to two orders of magnitude in some diameter ranges compared to observations. This leads to high biased overall simulated reflectivities.

Ultimately, these results indicate that all simulations fail to reproduce observed hydrometeor size distributions in which the majority of bulk mass is distributed at sub-0.5 mm sizes. Bulk scheme MSDs are sensitive to assumed hydrometeor properties including the particle number size distribution function and the mass-size relationship. The bin scheme failures show that additional causes of hydrometeor size biases are likely related to species partitioning and parameterization of microphysical processes. Biases resulting from microphysical processes are likely present in bulk schemes as well, but further research is needed to determine how much of the bias results from microphysical processes versus diagnosed properties.

Several caveats exist in this study, the majority of which have been discussed in Section 4.3. The largest caveat is from potentially biased aircraft sampling in which regions with high reflectivity values (> 40 dBZ) and lightning were avoided, which may limit the dataset's representation of the most intense convective cores. Despite this, evidence suggests that differences in hydrometeor size exist for even weak-moderate TWC and *w* constraints. Another important caveat is the comparison of observations

from all Darwin flights with a single simulated event, which is done due to computational limitations and small observed sample sizes for a single flight. Regardless, results show that hydrometeor sizes vary little between simulated events for a given bulk mass and *w* value, and thus comparison of a single case with observations of many cases is an appropriate strategy for validating simulations.

6.2 Future Work

Many opportunities are available for further evaluation of the HAIC-HIWC dataset. In particular, the release of data from the Cayenne phase of the field campaign includes many samples in the mixed-phase region around -10 °C where observations were lacking in the Darwin dataset. The Cayenne dataset is also subject to a lesser sampling bias than the Darwin dataset because the vast majority of convective cells in Cayenne failed to have lightning or high reflectivities aloft. While some results using the Cayenne data are discussed in Section 5.7, the data presented are only from the Falcon 20 aircraft. Additional measurements at temperatures warmer than -15 °C were made by Environment Canada's Convair aircraft, which will increase observed sample sizes. While Falcon 20 data from Cayenne generally support the Darwin data results, more statistical analyses should be performed to determine if the two datasets significantly differ. If not, merging the two datasets would provide a much more statistically robust comparison of observations with simulations. This would also require new simulations of Cayenne MCS cases.

While this study focused on properties of tropical convective updrafts, preliminary analyses reveal that biases are likely present in downdrafts as well. The

extent to which hydrometeor size biases are present in regions other than updrafts should be investigated along with associated differences in the interplay between dynamics and microphysics. If high biases exist as a function of temperature and TWC regardless of vertical velocity direction, then observational sample sizes used to establish the bias may be increased by including data points with negative vertical velocities. Moreover, the differing microphysical processes in updrafts versus downdrafts may provide an opportunity for investigating causes of hydrometeor size biases.

Finally, the work presented here should be used as guidance for generally improving microphysics parameterizations. Evidence suggests that documented biases in CRMs and LAMs partially result from very basic hydrometeor property assumptions, some of which have been discussed. Exploring the physical basis for these assumptions through comparison with robust and high-quality observations should remain a focus of future studies. Ideally, quantifying differences with observations caused by these assumptions will help to quantify biases in the representation of microphysical processes, which should also be further investigated in laboratories and field experiments.

REFERENCES

Ackerman, A. S., A. M. Fridlind, A. Grandin, F. Dezitter, M. Weber, J. W. Strapp, and A. V. Korolev, 2015: High ice water content at low radar reflectivity near deep convection – Part 2: Evaluation of microphysical pathways in updraft parcel simulations. *Atmos. Chem. Phys.*, **15**, 11729-11751, doi: 10.5194/acp-15-11729-2015.

Baumgardner, D., and Coauthors, 2011: Airborne instruments to measure atmospheric aerosol particles, clouds and radiation: A cook's tour of mature and emerging technology. *Atmos. Res.*, **102**, 10-29, doi: 10.1016/j.atmosres.2011.06.021.

Benmoshe, N., and A. Khain, 2014: The effects of turbulence on the microphysics of mixed—phase deep convective clouds investigated with a 2-D cloud model with spectral bin microphysics. *J. Geophys. Res. Atmos.*, **119**, 207-221, doi: 10.1002/2013JD020118.

Benmoshe, N., A. Khain, M. Pinsky, and A. Pokrovsky, 2012: Turbulent effects on cloud microstructure and precipitation of deep convective clouds as seen from simulations with a 2-D spectral microphysics cloud model. *J. Geophys. Res.*, **117**, D06220, doi: 10.1029/2011JD016603.

Blossey, P. N., C. S. Bretherton, J. Cetrone, and M. Kharoutdinov, 2007: Cloud-resolving model simulations of KWAJEX: Model sensitivities and comparisons with satellite radar observations. *J. Atmos. Sci.*, **64**, 1488-1508, doi:10.1175/JAS3982.1.

Bryan, G. H., J. C. Wyngaard, and J. M. Fritsch, 2003: Resolution requirements for the simulation of deep moist convection. *Mon. Wea. Rev.*, **131**, 2394-2416, doi: 10.1175/1520-0493(2003)131<2394:RRFTSO>2.0.CO;2.

Caine, S., T. P. Lane, P. T. May, C. Jakob, S. T. Siems, M. J. Manton, and J. Pinto, 2013: Statistical assessment of tropical convection-permitting model simulations using a cell-tracking algorithm. *Mon. Wea. Rev.*, **141**, 557-581, doi: 10.1175/MWR-D-11-00274.1.

Chen, F., and J. Dudhia, 2001: Coupling an advanced land-surface/ hydrology model with the Penn State/ NCAR MM5 modeling system. Part I: Model description and implementation. *Mon. Wea. Rev.*, **129**, 569–585, doi: 10.1175/1520-

0493(2001)129<0569:CAALSH>2.0.CO;2.

Cifelli, R., and S. A. Rutledge, 1998: Vertical motion, diabatic heating, and rainfall characteristics in north Australian convective systems. *Quart. J. Roy. Meteor. Soc.*, **124**, 1133-1162, doi: 10.1002/qj.49712454806.

Dezitter, F., A. Grandin, J.-L. Brenguier, F. Hervy, H. Schlager, P. Villedieu, and G. Zalamansky, 2013: HAIC – High Altitude Ice Crystals. *5th AIAA Atmospheric and Space Environments Conference*, San Diego, CA, American Institute of Aeronautics and Astronautics. [Available online at http://arc.aiaa.org/doi/abs/10.2514/6.2013-2674.]

Dudhia, J., 1989: Numerical study of convection observed during the winter monsoon experiment using a mesoscale two-dimensional model. *J. Atmos. Sci.*, **46**, 3077–3107, doi: 10.1175/1520-0469(1989)046<3077:NSOCOD>2.0.CO;2.

Fridlind, A. M., A. S. Ackerman, A. Grandin, F. Dezitter, M. Weber, J. W. Strapp, A. V. Korolev, and C. R. Williams, 2015: High ice water content at low radar reflectivity near deep convection – Part 1: Consistency of in situ and remote-sensing observations with stratiform rain column simulations. *Atmos. Chem. Phys.*, **15**, 11713-11728, doi: 10.5194/acp-15-11713-2015.

Grabowski, W. W., 2001: Coupling cloud processes with the large-scale dynamics using the cloud-resolving convection parameterization (CRCP). *J. Atmos. Sci.*, **58**, 978-997, doi: 10.1175/1520-0469(2001)058<0978:CCPWTL>2.0.CO;2.

Grabowski, W. W. and P. K. Smolarkiewics, 1999: CRCP: A cloud resolving convection parameterization for modeling the tropical convective atmosphere. *Physica D.*, **133**, 171-178, doi: 10.1016/S0167-2789(99)00104-9.

Grandin, A., J.-M. Merle, M. Weber, J. Strapp, A. Protat, and P. King, 2014: AIRBUS flight tests in high total water content regions. *6th AIAA Atmospheric and Space Environments Conference*, Reston, VA, American Institute of Aeronautics and Astronautics, doi: 10.2514/6.2014-2753.

Grzych, M. and J. Mason, 2010: Weather conditions associatied with jet engine power loss and damage due to ingestion of ice particles: What we've learned through 2009. *14th Conference on Aviation, Range and Aerospace Meteorology*, Atlanta, GA, Amer. Meteor. Soc.

Harshvardhan, S. E. Schwartz, C. M Benkovitz, and G. Guo, 2002: Aerosol influence on cloud microphysics examined by satellite measurements and chemical transport modeling. *J. Atmos. Sci.,* **59**, 714-725, doi: 10.1175/1520-0469(2002)059<0714:AIOCME>2.0.CO;2.

Hartmann, D. L., H. H. Hendon, and R. A. Houze Jr., 1984: Some implications of mesoscale circulations in tropical cloud clusters for large-scale dynamics and climate. *J. Atmos. Sci,* **41**, 113-121, doi: 10.1175/1520-

0469(1984)041<0113:SIOTMC>2.0.CO;2.

Heymsfield, A. J., 2007: On measurements of small ice particles in clouds. *Geophys. Res. Lett.,* **34**, doi:10.1029/2007GL030951.

Janjic, A. I., 1994: The Step-Mountain Eta Coordinate Model: Further Developments of the Convection, Viscous Sublayer, and Turbulence Closure Schemes. *Mon. Wea. Rev.*, **122**, 927-945, doi: 10.1175/1520-0493(1994)122<0927:TSMECM>2.0.CO;2.

Jorgensen, D. P. and M. A. LeMone, 1989: Vertical Velocity Characteristics of Oceanic Convection. *J. Atmos. Sci.,* **46**, 621-640, doi: 10.1175/1520-0493(1999)127<1056:VVCODC>2.0.CO;2.

Kain, J. S., 2004: The Kain-Fritsch Convective Parameterization: An update. *J. Appl. Meteor.*, **43**, 170-181, doi: 10.1175/1520-0450(2004)043<0170:TKCPAU>2.0.CO;2.

Kaufman, Y. J., and T. Nakajima, 1993: Effect of Amazon smoke on cloud microphysics and albedo-analysis from satellite imagery. *J. Appl. Meteor.*, **32**, 729-744, doi: 10.1175/1520-0450(1993)032<0729:EOASOC>2.0.CO;2.

Keenan, T. D., Michael J. Manton, Greg J. Holland, and Bruce R. Morton, 1989: The Island Thunderstorm Experiment (ITEX)—A Study of Tropical Thunderstorms in the Maritime Continent. *Bull. Am. Meteor. Soc.,* **70**, 152–159, doi: 10.1175/1520-0477(1989)070<0152:TITESO>2.0.CO;2.

Keenan, T. D., K. Glasson, F. Cummings, T. S. Bird, J. Keeler, and J. Lutz, 1998: The BMRC/NCAR C-Band Polarimetric (C-POL) Radar System. *J. Atmos. Oceanic Technol.,* **15**, 871–886, doi: 10.1175/1520-0426(1998)015<0871:TBNCBP>2.0.CO;2.

Keenan, T., and Coauthors, 2000: The Maritime Continent Thunderstorm Experiment (MCTEX): Overview and Some Results. *Bull. Am. Meteor. Soc.,* **81**, 2433–2455, doi: 10.1175/1520-0477(2000)081<2433:TMCTEM>2.3.CO;2.

Khain, A. P. and I. Sednev, 1996: Simulation of precipitation formation in the eastern Mediterranean coastal zone using a spectral bin microphysics cloud ensemble. *Atmos. Res.*, **43**, 77-110, doi:10.1016/S0169-8095(96)00005-1.

Khain, A. P., A. Pokrovsky, and I. Sednev, 1999: Some effects of cloud-aerosol interaction on cloud-microphysics, precipitation formation and size distribution of atmospheric aerosol: Numerical experiments with a spectral microphysics cloud model. *Atmos. Res.*, **52**, 195-220, doi: 10.1016/S0169-8095(99)00027-7.

Khain, A. P., M. Ovtchinnikov, M. Pinsky, A. Pokrovsky, and H. Krugliak, 2000: Notes on the state-of-the-art numerical modeling of cloud microphysics. *Atmos. Res.*, **55**, 159-224, doi: 10.1016/S0169-8095(00)00064-8.

Khain, A. P., K. D. Beheng, A. Heymsfield, A. Korolev, S. O. Krichak, Z. Levin, M.

Pinsky, V. Phillips, T. Prabhakaran, A. Teller, S. C. van den Heever, and J.-I. Yano, 2015: Representation of microphysical processes in cloud-resolving models: Spectral (bin) microphysics versus bulk parameterization. *Rev. Geophys.*, **53**, 247-322, doi: 10.1002/2014RG000468.

Khairoutdinov, M. F., and D. A. Randall, 2001: A cloud resolving model as a parameterization in the NCAR Community Climate System Model: Preliminary results. *Geophys. Res. Lett.*, **28**, 3617-3620, doi: 10.1029/2001GL013552.

Korolev, A. and G. A. Isaac, 2005: Shattering during Sampling by OAPs and HVPS. Part 1: Snow Particles. *J. Atmos. Oceanic Technol.,* **22**, 528-542, doi: 10.1175/JTECH1720.1.

Korolev, A., and P. R. Field, 2015: Assessment of the performance of the inter-arrival time algorithm to identify ice shattering artifacts in cloud particle probe measurements. *Atmos. Meas. Tech.,* **8**, 761-777, doi: 10.5194/amt-8-761-2015.

Krueger, S. K., 1988: Numerical simulation of tropical cumulus clouds and their interaction with the subcloud layer. *J. Atmos. Sci.*, **45**, 2221-2250, doi: 10.1175/1520-0469(1988)045<2221:NSOTCC>2.0.CO;2.

Lang, S., W.-K. Tao, J. Simpson, R. Cifelli, S. Rutledge, W. Olson, and J. Halverson, 2007: Improving simulations of convective systems from TRMM LBA: Easterly and westerly regimes. *J. Atmos. Sci.*, **64**, 1141-1164, doi: 10.1175/JAS3879.1.

Lang., S., W.-K. Tao, X. Zeng, Y. Li, 2011: Reducing the Biases in Simulated Radar Reflectivities from a Bulk Microphysics Scheme: Tropical Convective Systems. *J. Atmos. Sci.,* **68**, 2306-2320, doi: 10.1175/JAS-D-10-05000.1.

Lawson, R. P., 2011: Effects of ice particles shattering on the 2D-S probe. *Atmos. Meas. Tech.,* **4**, 1361-1381, doi:10.5194/amt-4-1361-2011.

Lawson, R. P., L. J. Angus, and A. J. Heymsfield, 1998: Cloud Particle Measurements in Thunderstorm Anvils and Possible Weather Threat to Aviation. *J. Aircr.*, **35**, 113-121, doi: 10.2514/2.2268.

Lawson, R. P., D. O'Connor, P. Amarzly, K. Weaver, B. Baker, Q. Mo., and H. Jonsson , 2006; The 2D-S (Stereo) Probe: Design and Preliminary Tests of a New Airborne, High-Speed, High-Resolution Particle Imaging Probe. *J. Atmos. Oceanic Technol.*, **23**, 1462-1477, doi: 10.1175/JTECH1927.1.

Leroy, D., E. Fontaine, A. Schwarzenboek, and J. W. Strapp, 2016: Ice Crystal Sizes in High Ice Water Content Clouds. Part 1: On the computation of Median Mass Diameter from in-situ measurements. *J. Atmos. Oceanic Technol.*, in press, doi: 10.1175/JTECH-D-15-0151.1.

Li, Y., E. J. Zipser, S. K. Krueger, and M. A. Zulauf, 2008: Cloud-resolving modeling of deep

convection during KWAJEX: Part 1: Comparison to TRMM satellite and ground-based observations. *Mon. Wea. Rev.*, **136**, 2699-2712, doi: 10.1175/2007MWR2258.1.

Lucas, C. and E. J. Zipser, 1994: Vertical Velocity in Oceanic Convection off Tropical Australia. *J. Atmos. Sci.*, **51**, 3183-3193, doi: 10.1175/1520-0469(1994)051<3183:VVIOCO>2.0.CO;2.

Lynn, B. H., A. P. Khain, J. Dudhia, D. Rosenfeld, A. Pokrovsky, and A. Seifert, 2005: Spectral (Bin) Microphysics Coupled with a Mesoscale Model (MM5). Part I: Model Description and First Results. *Mon. Wea. Rev.*, **133**, 44-58, doi: 10.1175/MWR-2840.1.

Mason, J. W. Strapp, and P. Chow, 2006: The Ice Particle Threat to Engines in Flight. *44th AIAA Aerospace Sciences Meeting and Exhibit*, Reno, NV, American Institute of Aeronautics and Astronautics, doi: 10.2514/6.2006-206.

Mason, J. G., and M. Grzych, 2011: The Challenges Identifying Weather Associated with Jet Engine Ice Crystal Icing. *SAE Technical Paper*, 2011-38-0094, doi:10.4271/2011-38-0094.

Matsui, T., X. Zeng, W.-K. Tao, H. Masunaga, W. S. Olson, and S. Lang, 2009: Evaluation of long-term cloud-resolving model simulations using satellite radiance observations and multifrequency satellite simulations. *J. Atmos. Oceanic Technol.*, **26**, 2185-2197, doi: 10.1175/2008JTECHA1168.1.

May., P. T. and A. Ballinger, 2007: The statistical characteristics of convective cells in a monsoon regime (Darwin, Northern Australia). *Mon. Wea. Rev.*, **135**, 82-92, doi: 10.1175/MWR3273.1.

May, P. T., J. H. Mather, G. Vaughan, K. N. Bower, C. Jakob, G. M McFarquhar, and G. G. Mace, 2008: The Tropical Warm Pool International Cloud Experiment. *Bull. Am. Meteor. Soc.*, **89**, 629-645, doi: 10.1175/BAMS-89-5-629.

Milbrandt, J. A., and M. K. Yau, 2005: A multimoment bulk microphysics parameterization. Part II: A proposed three-moment closure and scheme description. *J. Atmos. Sci.*, **62**, 3065-3081, doi: 10.1175/JAS3535.1.

Milbrandt, J. A., and M. K., Yau, 2006: A multimoment bulk microphysics parameterization. Part III: Control simulation of a hailstorm. *J. Atmos. Sci.*, **63**, 3114-3136, doi: 10.1175/JAS3816.1.

Mitchell, D. L., R. Zhang, and R. L. Pitter, 1990: Mass-dimensional relationships for ice particles and the influence of riming on snowfall rates. *J. Appl. Meteor.*, **29**, 153-163, doi: 10.1175/1520-0450(1990)029<0153:MDRFIP>2.0.CO;2.

Mlawer, E. J., S. J. Taubman, P. D. Brown, M. J. Iacono, and S. A. Clough, 1994: Radiative transfer for inhomogeneous atmosphere: RRTM, a validated correlated-

k model for the longwave. *J. Geophys. Res.*, **102**, 16663–16682, doi:10.1029/97JD00237.

Morrison, H., G. Thompson, and V. Tatarskii, 2009: Impact of cloud microphysics on the development of trailing stratiform precipitation in a simulated squall line: Comparison of one- and two-moment schemes. *Mon. Wea. Rev.,* **137**, 991-1007, doi: 10.1175/2008MWR2556.1.

Nesbitt, S. W., R. Cifelli, and S. A. Rutledge, 2006: Storm morphology and rainfall characteristics of TRMM precipitation features. *Mon. Wea. Rev.,* **134**, 2702-2721, doi: 10.1175/MWR3200.1.

Protat, A., and co-authors, 2009: Assessment of CloudSat reflectivity measurements and ice cloud properties using ground-based and airborne cloud radar observations. *J. Atmos. Oceanic Technol.*, **26**, 1717-1741, doi: 10.1175/2009JTECHA1246.1.

Pruppacher, H. R., and J. D. Klett, 1997: *Microphysics of Clouds and Precipitation*. Kluwer Academic Publishers, 954 pp.

Ramanthan, V., R. D. Cess, E. F. Harrison, P. Minnis, B. R. Barkstrom, E. Ahmad, and D. Hartmann, 1989: Cloud-radiative forcing and climate: Results from the Earth radiation budget experiment. *Science,* **243**, 57-63, doi: 10.1126/science.243.4887.57.

Randall, D. A., M. Khairoutdinov, A. Arakawa, and W. W. Grabowski, 2003: Breaking the cloud parameterization deadlock. *Bull. Am. Meteor. Soc.*, **84**, 1547-1564, doi: 10.1175/BAMS-84-11-1547.

Reisner, R., R. M. Rasmussen, and R. T. Bruintjes, 1998: Explicit forecasting of supercooled liquid water in winter storms using the MM5 mesoscale model. *Quart. J. Roy. Meteor. Soc.,* **124**, 1071-1107, doi: 10.1002/qj.49712454804.

Russell, P. B., L. Pfister, and H. B. Selkirk, 1993: The tropical experiment of the Stratosphere-Troposphere Exchange Project (STEP): Science objectives, operations, and summary findings. *J. Geophys. Res*., **98**, 8563–8589, doi: 10.1029/92JD02521.

Rutledge, S. A. and P. V. Hobbs, 1983: The mesoscale and microscale structure of organization of clouds and precipitation in midlatitude cyclones. VIII: A model for the "seeder-feeder" process in warm-frontal rainbands. *J. Atmos. Sci.*, **40**, 1185-1206, doi: 10.1175/1520-0469(1983)040<1185:TMAMSA>2.0.CO;2.

Rutledge, S. A. and P. V. Hobbs, 1984: The mesoscale and microscale structure and organization of clouds and precipitation in midlatitude cyclones. Part XII: A diagnostic modeling study of precipitation development in narrow cold-frontal rainbands. *J. Atmos. Sci.,* **41**, 2949-2972, doi: 10.1175/1520-0469(1984)041<2949:TMAMSA>2.0.CO;2.

Rutledge, S. A., Earle R. Williams, and Thomas D. Keenan, 1992: The Down Upper Doppler and Electricity Experiment (DUNDEE): Overview and Preliminary Results. *Bull. Am. Meteor. Soc.,* **73**, 3–16, doi: 10.1175/1520-0477(1992)073<0003:TDUDAE>2.0.CO;2.

Schumacher, C. R. A. Houze Jr., and I. Kraucunas, 2004: The tropical dynamical response to latent heating estimates derived from the TRMM precipitation radar. *J. Atmos. Sci*., **61**, 1341-1358, doi: 10.1175/1520-0469(2004)061<1341:TTDRTL>2.0.CO;2.

Skamarock, W. C., and Coauthors, 2008: A description of the advanced research WRF version 3. NCAR Tech. Note NCAR/TN-475+STR, 113 pp., doi: 10.5065/D68S4MVH.

Smith, P. L., 1984: Equivalent radar reflectivity factors for snow and ice particles. *J. Climate Appl. Meteor.,* **23**, 1258-1260, doi: 10.1175/1520-0450(1984)023<1258:ERRFFS>2.0.CO;2.

Stith, J. L., J. E. Dye, A. Bansemer, A. J. Heymsfield, C. A. Grainger, W. A. Petersen, and R. Cifelli, 2002: Microphysical observations of tropical clouds. *J. Appl. Meteor*., **41**, 97-117, doi: 10.1175/1520-0450(2002)041<0097:MOOTC>2.0.CO;2.

Stith J. L., J. A. Haggerty, and A. Heymsfield, 2004: Microphysical Characteristics of Tropical Updrafts in Clean Conditions. *J. Appl. Meteor.,* **43**, 779-794, doi: 10.1175/2104.1.

Stoelinga, M. T., and Coauthors, 2003: Improvement of Microphysical Parameterization through Observational Verification Experiment. *Bull. Am. Meteor. Soc.,* **84**, 1807-1826, doi: 10.1175/BAMS-84-12-1807.

Strapp, J. W., A. Korolov, T. Ratvasky, R. Potts, A. Protat, et al., 2015: The High Ice Water Content (HIWC) Study of Deep Convective Clouds: Science en Technical Plan, FAA report DOT/FAA/TC14/31, in press.

Takahashi, T., T. Endoh, and G. Wakahama, 1991: Vapor diffusional growth of free-falling snow crystals between -3° and 23°. *J. Meteor. Soc. Japan,* **69**, 15-30.

Tao, W.-K., and M. W. Moncrieff, 2009: Multiscale cloud system modeling. *Rev. Geophys.*, **47**, doi:10.1029/2008RG000276.

Thompson, G., P. R. Field, R. M Rasmussen, and W. D. Hall, 2008: Explicit forecasts of winter precipitation using an improved bulk microphysics scheme. Part II: Implementation of a new snow parameterization. *Mon. Wea. Rev.,* **136**, 5095-5115, doi: 10.1175/2008MWR2387.1.

Thompson, G. and T. Eidhammer, 2014: A Study of Aerosol Impacts on Clouds and Precipitation Development in a Large Winter Cyclone. *J. Atmos. Sci.,* **71**, 3636-3658, doi: 10.1175/JAS-D-13-0305.1.

Tiedtke, M., 1993: Representation of Clouds in Large-Scale Models. *Mon. Wea. Rev.*, **121**, 3040-3061, doi: 10.1175/1520-0493(1993)121<3040:ROCILS>2.0.CO;2.

Varble, A., A. M. Fridlind, E. J. Zipser, A. S. Ackerman, J.-P. Chaboureau, J. Fan, A. Hill, S. A. McFarlane, J.-P. Pinty, and B. Shipway, 2011: Evaluation of cloud-resolving model intercomparison simulations using TWP-ICE observations: Precipitation and cloud structure. *J. Geophys. Res.*, **116**, D12206, doi:10.1029/2010JD015180.

Varble, A., E. J. Zipser, A. M. Fridlind, P. Zhu, A. S. Ackerman, J.-P. Chaboureau, S. Collis, J. Fan, A. Hill, and B. Shipway (2014), Evaluation of cloud-resolving and limited area model intercomparison simulations using TWP-ICE observations: 1. Deep convective updraft properties. *J. Geophys. Res. Atmos.*, **119**, 13891-13918, doi:10.1002/2013JD021371.

Varble, A., E. J. Zipser, A. M. Fridlind, P. Zhu, A. S. Ackerman, J.-P. Chaboureau, J. Fan, A. Hill, B. Shipway, and C. Williams, 2014: Evaluation of cloud-resolving and limited area model intercomparison simulations using TWP-ICE observations: 2. Precipitation Microphysics. *J. Geophys. Res. Atmos.*, **119**, 13919-13945, doi: 10.1002/2013JD021372.

Weisman, M. L., W. C. Skamarock, and J. B. Klemp, 1997: The Resolution Dependence of Explicitly Modeled Convective Systems. *Mon. Wea. Rev.*, **125**, 527-548, doi: 10.1175/1520-0493(1997)125<0527:TRDOEM>2.0.CO;2.

Westbrook, C. D., R. C. Ball, P. R. Field, and A. J. Heymsfield, 2004: Universality in snowflake aggregation. *Geophys. Res. Lett*., **31**, doi:10.1029/2004GL020363.

Zipser, E. J., and M. A. LeMone, 1980: Cumulonimbus vertical velocity events in GATE. Part I: Diameter, Intensity, and Mass Flux. *J. Atmos. Sci.*, **34**7 2444-2457, doi: 10.1175/1520-0469(1980)037<2444:CVVEIG>2.0.CO;2.

Zipser, E. J., and K. R. Lutz, 1994: The Vertical Profile of Radar Reflectivity of Convective Cells: A Strong Indicator of Storm Intensity and Lightning Probability?, *Mon. Wea. Rev.,* **122**, 1751-1759, doi: 10.1175/1520-0493(1994)122<1751:TVPORR>2.0.CO;2.